Innovations in sparse MRI

In search of a free lunch

Schoormans, J.

Innovations in Sparse MRI

In search of a free lunch

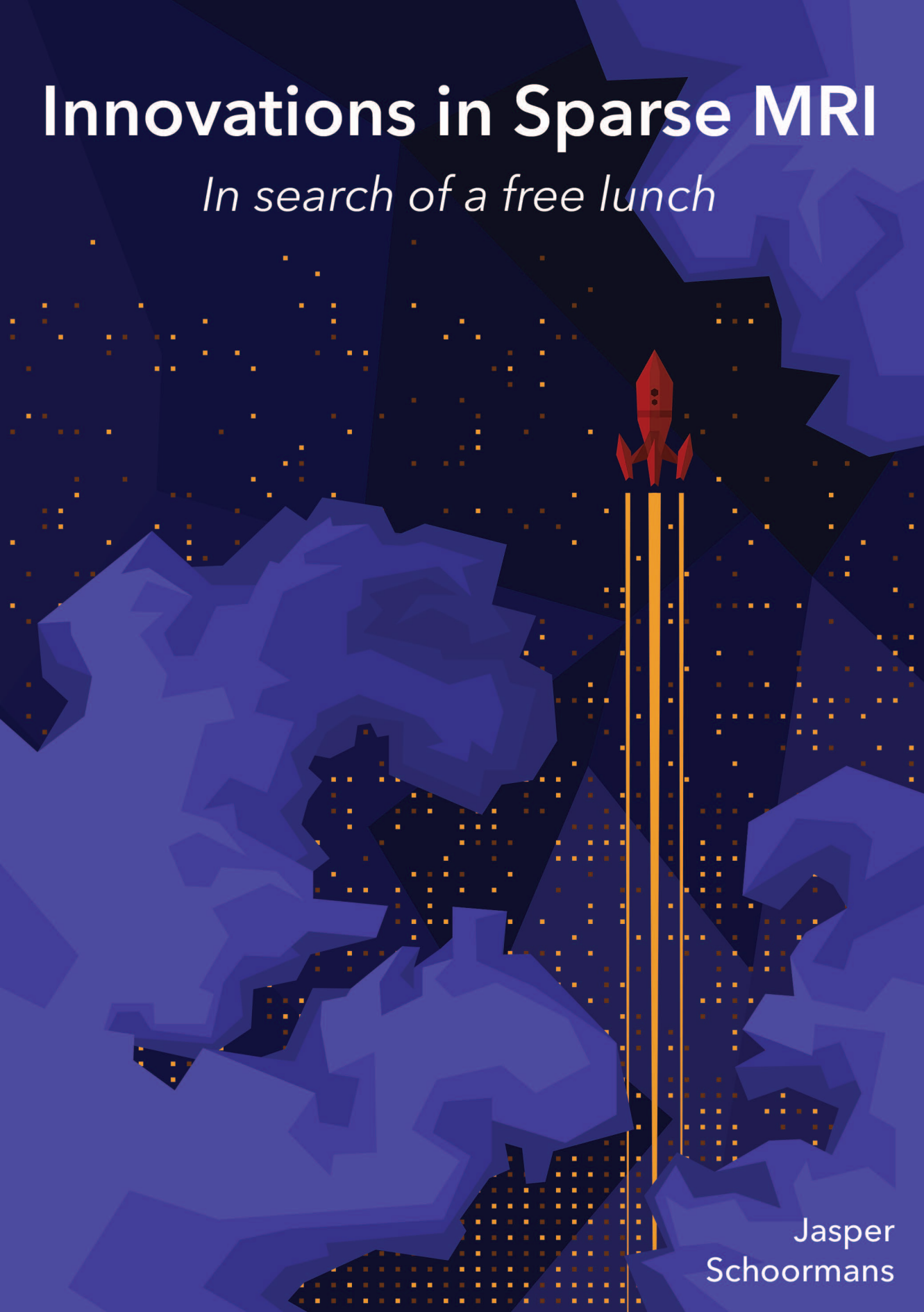

Jasper Schoormans

Innovations in Sparse MRI

In search of a free lunch

Jasper Schoormans

Layout & Design Jasper Schoormans
ISBN 978-94-6332-661-2

Innovations in Sparse MRI

In search of a free lunch

ACADEMISCH PROEFSCHRIFT
ter verkrijging van de graad van doctor
aan de Universiteit van Amsterdam
op gezag van de Rector Magnificus
prof. dr. ir. K.I.J. Maex
ten overstaan van een door het College voor Promoties ingestelde commissie,
in het openbaar te verdedigen in de Agnietenkapel
op donderdag 17 september 2020, te 16.00 uur

door Jasper Schoormans
geboren te Dordrecht

Promotiecommissie

Promotores:	Prof. dr. ir. G.J. Strijkers	AMC-UvA
	Prof. dr. ir. A.J. Nederveen	AMC-UvA
Copromotor:	Dr. ir. B.F. Coolen	AMC-UvA
Overige leden:	Prof. dr. ir. J.J. Sonke	AMC-UvA
	Dr. ir. M.W.A. Caan	AMC-UvA
	Prof. dr. E.S.G. Stroes	AMC-UvA
	Dr. ir. C.A.T. van den Berg	Universiteit Utrecht
	Prof. dr. M.E. Kooi	Universiteit Maastricht
	Prof. dr. M. Stuber	University of Lausanne

Faculteit der Geneeskunde

Table of contents

Introduction 6
Compressed Sensing MRI with variable density averaging (CS-VDA) outperforms full sampling at low SNR 17
Plaque permeability assessed with dynamic contrast-enhanced MRI predicts ferumoxytol nanoparticle uptake in patients with peripheral artery disease 43
Pharmacokinetic modeling of 3D black-blood vessel wall DCE imaging using an AIF independent reference region method 61
An iterative sparse deconvolution method for simultaneous multicolor ^{19}F-MRI of multiple contrast agents 81
Accelerated 4D self-gated MRI of tibiofemoral kinematics 103
General Discussion 125
Summary 132
Nederlandse samenvatting 134
PhD portfolio 136

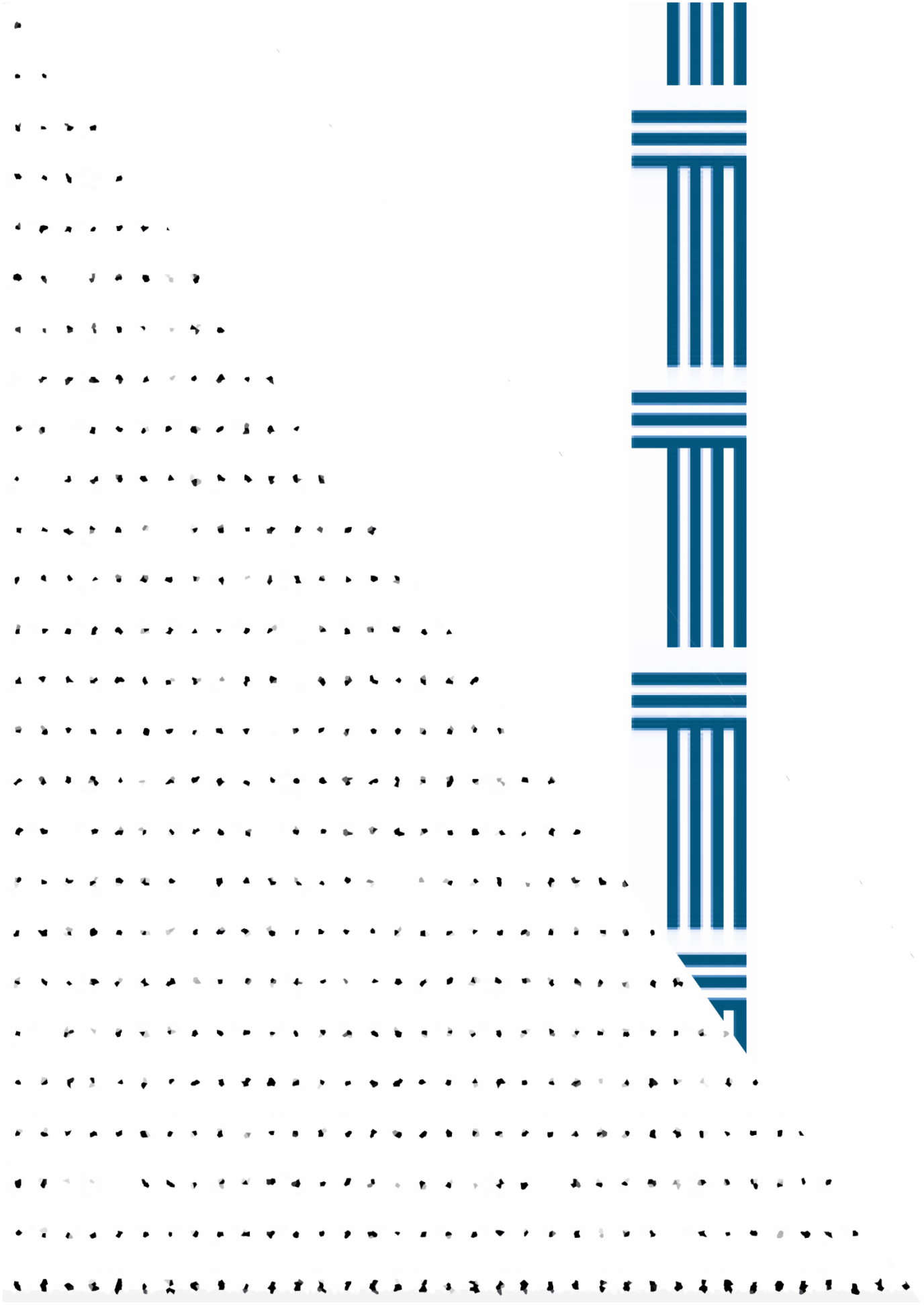

Chapter 1

Introduction

While millions of people undergo an MRI-exam every year, it remains an expensive and lengthy diagnostic tool, unavailable to many. The cramped space, loud and unfamiliar sounds, and long scan times make it an unpleasant experience for many patients. Often, a substantial part of the exam needs to be redone because of insufficient image quality, patient motion or other artefacts. Still, MRI is a unique diagnostic tool. We are now able to discriminate tissues based on an almost inexhaustible list of properties. Most MR images depict the spatial distribution of hydrogen atoms in the body. The magnetic moments of the tiny nuclei of these hydrogen atoms will align with the strong magnetic field of the scanner. A sequence of radiofrequency pulses and variations in magnetic fields causes these nuclei to do a sort of mass choreography. Small differences in this choreography, between healthy and diseased tissue for instance, can be shown using MRI.
The great versatility in MRI contrast is unparalleled in the medical imaging field. For example, we can measure diffusion in cells—tiny molecules are always randomly shooting in all directions at very high speeds, and we are able to say something about the speed and direction in which they do. We can even visualize the flow of blood in small arteries and vessels, with extreme precision in time and space. Contrasts between tissues can be tweaked to your heart's content, and if we want to remove bothersome signal (fat in the knee, or blood signal in vessel wall imaging) we can find a sequence that does just that. We even have the ability to image nuclei different than hydrogen, such as fluorine (^{19}F) or phosphorus (^{31}P). And let's not forget the multi dimensionality: two- and three-dimensional images are standard, but we can even vary over time, respiratory and cardiac phases, echo times, etc. Only string theorists use more dimensions than MR physicists, it seems.

However, this extreme versatility comes with one important caveat: measuring takes time. A long time. While a CT examination is over in minutes, and an ultrasound probe can give volumetric information almost instantaneously, MR exams are notoriously slow. Relax and make yourself comfortable, we'll see you in an hour.

It is often said that there is *no free lunch* in MRI; this is a simple yardstick you can use to hit claims of ambitious researchers with. One example of the *no free lunch* theory is the well-known trade-off between imaging speed, signal-to-noise ratio (SNR) and resolution (Figure 1). In the quest for early detection of disease, we want sharper images, measured with a higher resolution. However, this means an increase in scan time, and a decrease of valuable SNR—you have the resolution to see the subtle lesions the doctor wanted to see, but now they are hidden in a sea of noise; and due to the longer scan time the patient has moved, blurring the image. Moreover, patient comfort and ever-increasing healthcare costs demand quick MR check-ups.

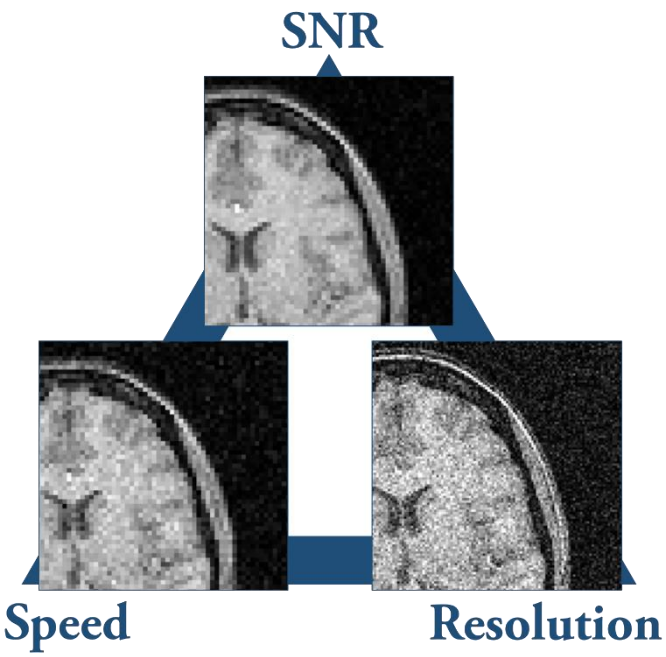

Figure 1. The balancing act. Classically, if the MR operator wants to double the resolution of a 3D acquisition, he expects the scan to take four times as long. However, this will also negatively impact the SNR. Alternatively, he can choose to improve the SNR of the original scan by averaging. To double the SNR, he needs to scan four times as long. The invention of smart sampling and reconstruction techniques gives more options for sequence designers in this balancing act.

We face these challenges, and they require us to handle the MRI process in its entirety in a smarter way. If we can manage to accelerate MR exams considerably with minimum drawbacks, it will increase patient throughput, enable higher resolution scans and ultimately have more and better diagnoses.

In the last years, the field of magnetic resonance imaging has undergone a major innovation push. Acceleration techniques have been introduced and refined, and ever-smarter things keep on arriving. It seems that, sometimes, there is such a thing as a free lunch. Or, if not free, the lunch is heavily discounted. Extremely clever acceleration techniques with names like SENSE, GRAPPA, and compressed sensing are the shoulders of giants upon which we as researchers are currently standing.
The studies described in this thesis have the overarching aim to progress the field of accelerated MRI beyond its current possibilities and to demonstrate the possibilities of these novel methods in relevant clinical applications.
The remainder of this introductory section presents further details on relevant research on MR acceleration techniques. This would be a good moment to refresh

the basics of MR physics. The section concludes with an overview of the research described in this thesis.

1.2 A technical introduction to this thesis

The signals recorded in Magnetic Resonance Imaging (MRI) are usually Fourier-encoded. Neglecting all effects of tissue and sequence parameters on the magnetization, we can reasonably model the received signal $\boldsymbol{y}$ as the discretized Fourier transform of the magnetization:

$$\boldsymbol{y} = \boldsymbol{F}x, \tag{1}$$

where **x** is the magnetization and F is the discrete Fourier Transform (DFT). The k-space signal $\boldsymbol{y}$ is usually collected during many repetition times (TR), every TR acquiring one k-line. For a two- or three-dimensional single-coil Cartesian acquisition, image reconstruction is simply an inverse DFT:

$$\hat{\boldsymbol{x}} = F^{-1}\,\boldsymbol{y}. \tag{2}$$

However, image reconstruction quickly becomes more difficult when we add receive coils or sample differently, e.g. on a non-Cartesian grid or by omitting certain k-lines.

Image reconstruction in the presence of multiple channels
In general, the signal received by coil element $\boldsymbol{i}$ can be described as:

$$\boldsymbol{y_i} = F_s C_i \boldsymbol{x}, \tag{3}$$

where F_s is the encoding matrix, and C_i is a matrix describing the coil sensitivity on the diagonal. The encoding matrix is known beforehand: the researcher has chosen the location of encoding k-lines. The coil sensitivity matrix, however, is unknown beforehand and should be measured, either by calibration k-lines or a low-resolution pre-scan. Combining the received signal from all coil elements into one model, we get:

$$\begin{bmatrix} \boldsymbol{y_1} \\ \vdots \\ \boldsymbol{y_N} \end{bmatrix} = \begin{bmatrix} F_s & \cdots & 0 \\ \vdots & \ddots & \vdots \\ 0 & \cdots & F_s \end{bmatrix} \begin{bmatrix} C_1 \\ \vdots \\ C_N \end{bmatrix} \boldsymbol{x} + \boldsymbol{\eta}, \tag{4}$$

for *N* coil elements. Here $\boldsymbol{\eta}$ is the noise term.

Parallel imaging is a complete family of reconstruction techniques; most of these were developed in the late 1990s[1] when receive coils with multiple elements started

to become available. The overarching idea of parallel MRI (pMRI) is to accelerate MRI by selectively omitting certain k-lines. The resulting aliasing is then resolved by using prior knowledge of the local sensitivities of the coil elements.
We can recognize two main branches in pMRI: image-based and k-space based reconstruction. Image-based pMRI uses knowledge of coil sensitivities for image reconstruction, examples of these are SENSE (Sensitivity Encoding), which was introduced in 1999 [2], and is an optimized form of an earlier-published idea called *subencoding* [3]. In contrast, k-space based pMRI, like GRAPPA [4], extracts a k-space kernel from autocalibration lines, and performs unaliasing in k-space.

The goal in image reconstruction is to recover the image **x**. The more prior information we have, the better our reconstructed result image can be. The entire MR measurement can be put in a *forward model,* with the magnetization as an unknown that is to be solved for. More generally put, the Fourier- and coil-sensitivity encoding matrices in Equation 4 can be combined into one model matrix **M** as:

$$\boldsymbol{y} = \boldsymbol{M}\boldsymbol{x} + \boldsymbol{\eta}. \tag{5}$$

The model matrix can be expanded to include inhomogeneity effects, different sampling patterns, et cetera. In parallel MRI, the predictable nature of the aliasing behavior caused by regular undersampling can be leveraged to solve for **x**. However, not all image reconstruction problems are that easy, for instance in the case of SENSE with arbitrary k-space trajectories [5]. In those cases, Equation 5 can also be reformulated as an iterative optimization problem of the form:

$$\hat{\boldsymbol{x}} = \arg\min |\boldsymbol{M}\boldsymbol{x} - \boldsymbol{y}|_2^2 + \lambda R(\boldsymbol{x}), \tag{6}$$

where R(x) is an (optional) regularization function, λ is a regularization parameter, and the minimization is put into a l_2*-norm.*

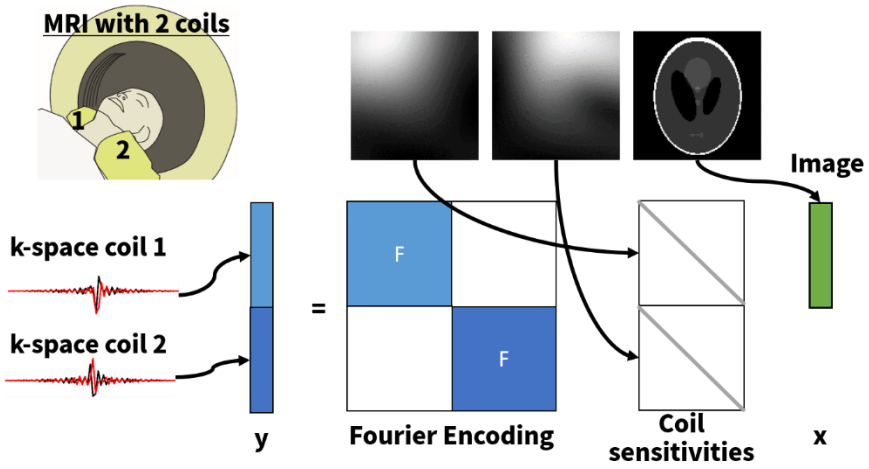

Figure 2. The building blocks of equation 4. A multi-channel coil receives localized k-space data. The k-space can be described as the final image, multiplied by the coil sensitivity maps and transformed to the Fourier domain. Undersampled strategies accelerate scans, and in effect, the Fourier encoding matrix becomes high and narrow.

Equation 6 is a very powerful model to pose our problem as. With Equation 6, we can significantly accelerate the MRI experiment, modifying M, and if we add enough prior information to our regularizer, we are still able to recover **x.** Alternatively, we can modify our experiments to improve image quality—i.e. such that our error $|\hat{\boldsymbol{x}} - \boldsymbol{x}|_2^2$ is as small as possible—an approach I have taken in chapter 2 of this thesis. Thirdly, we might be interested instead to recover the magnetization in a different *form:* visualizing the magnetization over different time frames, for instance. I describe such an approach in chapters three, four, and six. Finally, in chapter five, this concept is used to reconstruct separate magnetization images for different ^{19}F compounds.

Compressed Sensing

Compressed Sensing (CS) [6], like parallel methods, can be used to accelerate or otherwise improve MR acquisitions. It deviates from pMRI in several important ways: while SENSE and GRAPPA have a very regular pattern of omitted k-lines, CS uses *incoherent* undersampling. Incoherent undersampling in the Fourier domain gives rise to undersampling artifacts in the image-domain that don't add up constructively—these artefacts are noise-like and do not represent natural images.

The main assumption of CS is sparsity: the idea that the information content is much less than the number of pixels suggests. Most, if not all, medical images are naturally sparse in some representation. This means that the signal can be represented by a vector containing a small number of non-zero entries. However, the sparsity is

usually not in the image (pixel) domain, they are sparse under a transformation instead. The sparsity transforms used in CS are similar to the Fourier transform, as they are a one-to-one transformation of the image domain to another domain, preserving all the information, so that after applying the inverse transform the initial image is recovered (Figure 3). Sparsity can be measured by counting the zero-valued entries (the l_0-norm), but the l_1-norm is usually used instead, since this can be more efficiently minimized, while resulting in the same solution.

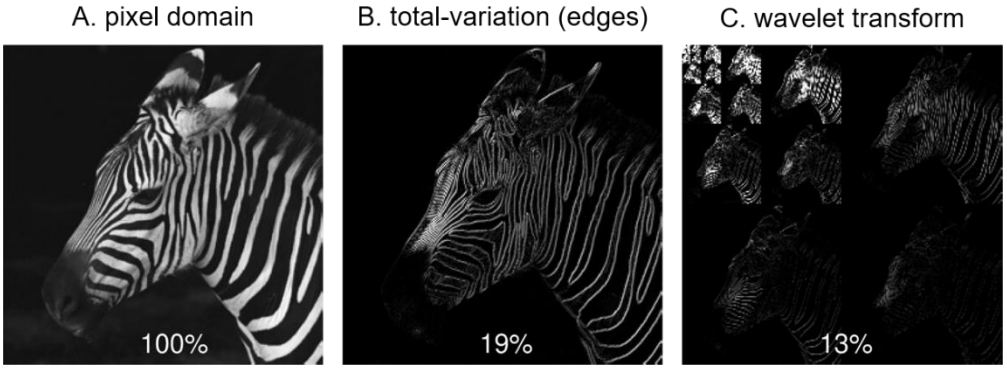

Figure 3. Sparsity is defined as the fraction of zero-valued elements. In the pixel domain (panel A), all pixel values are greater than zero. However, we can also calculate the total-variation (the edges), and see that only about a fifth of pixels still contain non-zero information (panel B). With the edge information for both directions, you could perfectly recover the original image. Another (slightly less intuitive) transform that can efficiently capture all image information is the wavelet transform, with only 13% of the original data size (panel C).

CS image reconstruction can be performed by adapting Eq. 6 to the LASSO-form:

$$\hat{\boldsymbol{x}} = \arg\min |M\boldsymbol{x} - \boldsymbol{y}|_2^2 + \lambda |W\boldsymbol{x}|_1 , \tag{7}$$

where W is a transform operator, the wavelet transform or a finite-difference operator are often used. The l_2-norm in this equation enforces the data consistency, while sparsity is forced by the l_1-norm (see inset, Figure 5). The regularization parameter λ can be tuned to balance between these terms and will be dependent on noise levels and inherent sparsity of the image. Equation 7 can be solved by any of a myriad of reconstruction algorithms. [7]

The last ten years have seen a huge interest in the research community in sampling pattern design, algorithmic development, and optimal sparse transformations. In addition to sparsity in image space, sparsity over time (dynamic imaging) has been

The $l_{1,2}$-norms, an analogy

Imagine you are in New York, standing at the intersection of Central Park West and 67th street. Your friend calls you to meet you and says: I'm on Broadway, I could not be closer to you—and at that moment the connection drops. You know he is on Broadway, the yellow line on the map, but you didn't catch the full address. He can be anywhere on that long street. However, he also said: 'I could not be closer to you'. You start mentally drawing an ever-expanding circle on the map. It grows, until it touches Broadway, at W 65th. This is the point on Broadway with the shortest distance to you, according to Pythagoras (this distance is sometimes called the l_2-norm). However, now you remember that you are in Manhattan. Here, distance is not calculated as in the rest of the world—you use the *Manhattan-distance* instead, also known as the l_1-norm. The shape for equidistant points is a square, rotated 45 degrees to the grid. For all points on this square (the red line on the map), the walking distance along the street grid is the same. This means that your friend is at 67th street and Broadway! In this system, the closest intersection is also the most sparse: sparsity in Manhattan means the number of different streets you'd have to walk on: only one!

Figure 4. The l-norms in New York.

In our accelerated MR experiments, we also have incomplete information, but rather than a phone call in which a few words were dropped, we have decided to skip some k-lines. Just like in Manhattan, we need a simple solution, in our case a *sparse* image, that fits with the data that we do know for sure.

proposed, in addition to low-rank methods, joint sparsity, etc. These are all variations on the basic model in Equation 6.

However, sparsity and incoherence can be described more subtly, as these seem to vary over resolutions; a property called multi-level sparsity [8] has been proposed. This insight can explain why the variable-density sampling pattern, which has been experimentally derived, has seen so much success. In effect, the low-resolution k-space does not encode for a very sparse image; while the high-resolution outer k-space does.

Accelerated dynamic imaging

Dynamic MRI is a booming research field and is used for visualization of perfusion, and motion dynamics. Acceleration techniques can be directly used to increase frame-rates, enabling more reliable visualization of dynamic processes. Parallel MRI strategies can accelerate dynamic MRI roughly as much as static images, 2 to 6 times generally, thus limiting the achievable framerate. In contract, CS approaches can leverage the enormous sparsity that exists in these datasets for very high accelerations, tens of times faster than fully sampled. As subsequent frames are usually highly correlated, information can be compressed greatly. In line with the examples given in Figure 1, the sparsity can be calculated, for example by a total-variation constraint in the time dimension [9] (see Figure 4). Several chapters (4,5 and 6) in this thesis deal with accelerated *dynamic* imaging. We have used the *golden-angle* sampling strategy [10]. In this strategy, subsequent k-lines are chosen such that the angle between the two (the "golden angle") is equal to the angle dividing the semicircle with the golden ratio. It can be shown [11] that this gives a nearly uniform k-space coverage for an arbitrary number of lines, as every line fills in the largest remaining gaps. A similar strategy can be found throughout nature, e.g. in the distribution of leaves on a stem, optimized for maximum sunlight coverage.
Additionally, radial k-space sampling is robust to motion artefacts, and gives undersampling artefacts which look like streaking, and which are well optimized for in a reconstruction.

Multicolor Fluorine imaging

Fluorine (^{19}F) MRI is rapidly gaining traction for in vivo cell tracking [12], as any signal can be assumed to originate from exogenously administered fluorine probes [13]. The different PFCs differ from one another in terms of the number of ^{19}F resonances and their chemical shifts. In chapter 6 of this thesis, we have leveraged these differences, and the model-based MR equation 6, to detect different ^{19}F-containing nanoparticles in the same sample and in the same imaging session, enabling "*multicolor*" ^{19}F-MRI.

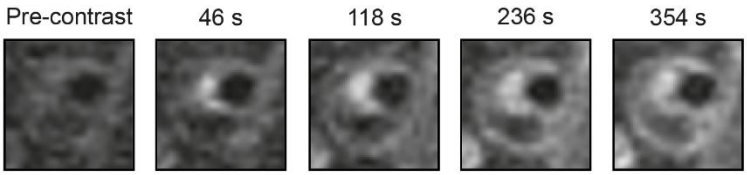

Figure 5. Close-ups of the signal of a femoral arterial plaque, as measured with a highly accelerated dynamic contrast-enhanced black-blood sequence [chapters 3,4 of this thesis]. Note the high correlation between time frames, a property that is exploited by compressed sensing techniques to achieve very high frame-rates (12 seconds per volume in this case).

1.3 Thesis aims and outline

The studies described in this thesis have the overarching aim to progress the field of accelerated MRI beyond its current possibilities and to demonstrate the possibilities of these novel methods in relevant clinical applications. As we have seen in this chapter, a myriad of successful applications of accelerated MRI by means of a sparse prior have been introduced in the last decade. However, the usually stated goals of increasing scan resolution by leveraging the saved acquisition time are not usually successfully met—the SNR penalty is the limiting factor. Therefore, I aimed to study and improve CS for low SNR acquisitions. Chapter 2 introduces a novel sampling method applying CS to low-SNR MRI.

In chapter 3, I have studied the possibility of volumetric, accelerated dynamic contrast-enhanced MRI for vessel wall imaging. Vessel wall delineation requires blood signal suppression. However, this suppression makes pharmacokinetic analysis of the data more difficult. In this chapter, I investigate the use of arterial input-free analysis methods.

In chapter 4, I continue this research, by applying the sequence to a group of patients with femoral atherosclerotic plaques. I found a correlation between DCE-MRI and USPIO uptake in the patient group.

In chapter 5, a radial stack-of-stars acquisition was applied for dynamic imaging of the patella in a moving knee.

Chapter 6 uses the possibilities of iterative reconstruction and the MR physics to enable multi-color MRI for ^{19}F MRI. I describe a novel method to simultaneously measure two chemical compounds.

Finally, in chapter 7, I discuss findings and propose future directions for this research.

1.4 References

[1] R. M. Heidemann, P. M. Parizel, M. A. Griswold, and P. M. Jakob, "A brief review of parallel magnetic resonance imaging," *Eur. Radiol.*, vol. 13, no. 10, pp. 2323–2337, 2003.

[2] K. P. Pruessmann, M. Weiger, M. B. Scheidegger, and P. Boesiger, "SENSE: Sensitivity encoding for fast MRI," *Magn. Reson. Med.*, vol. 42, no. 5, pp. 952–962, 1999.

[3] J. B. Ra and C. Y. Rim, "Fast Imaging Using Subencoding Data Sets from Multiple Detectors," *Magn. Reson. Med.*, vol. 30, no. 1, pp. 142–145, 1993.

[4] M. A. Griswold, P. M. Jakob, R. M. Heidemann, M. Nittka, V. Jellus, J. Wang, B. Kiefer, and A. Haase, "Generalized Autocalibrating Partially Parallel Acquisitions (GRAPPA)," *Magn. Reson. Med.*, vol. 47, pp. 1202–1210, 2002.

[5] K. P. Pruessmann, M. Weiger, P. Börnert, and P. Boesiger, "Advances in sensitivity encoding with arbitrary k -space trajectories," *Magn. Reson. Med.*, vol. 46, no. 4, pp. 638–651, Oct. 2001.

[6] M. Lustig, D. Donoho, and J. M. Pauly, "Sparse MRI: The application of compressed sensing for rapid MR imaging," *Magn. Reson. Med.*, vol. 58, no. 650, pp. 1182–1195, 2007.

[7] J. A. Fessler, "Optimization methods for MR image reconstruction (long version)," *arXiv Prepr.*, vol. arXiv:1903, pp. 1–12, Mar. 2019.

[8] B. Roman, A. Hansen, and B. Adcock, "On asymptotic structure in compressed sensing," *arXiv Prepr. arXiv1406.4178*, no. c, pp. 1–10, 2014.

[9] K. T. Block, M. Uecker, and J. Frahm, "Undersampled radial MRI with multiple coils. Iterative image reconstruction using a total variation constraint," *Magn. Reson. Med.*, vol. 57, no. 6, pp. 1086–1098, 2007.

[10] L. Feng, R. Grimm, K. T. obias Block, H. Chandarana, S. Kim, J. Xu, L. Axel, D. K. Sodickson, and R. Otazo, "Golden-angle radial sparse parallel MRI: combination of compressed sensing, parallel imaging, and golden-angle radial sampling for fast and flexible dynamic volumetric MRI," *Magn. Reson. Med.*, vol. 72, no. 3, pp. 707–717, 2014.

[11] S. Wundrak, J. Paul, J. Ulrici, E. Hell, and V. Rasche, "A small surrogate for the golden angle in time-resolved radial MRI based on generalized fibonacci sequences," *IEEE Trans. Med. Imaging*, vol. 34, no. 6, pp. 1262–1269, 2015.

[12] E. T. Ahrens, R. Flores, H. Xu, and P. A. Morel, "In vivo imaging platform for tracking immunotherapeutic cells," *Nat. Biotechnol.*, vol. 23, no. 8, pp. 983–987, 2005.

[13] M. Srinivas, A. Heerschap, E. T. Ahrens, C. G. Figdor, and I. J. M. de Vries, "19F MRI for quantitative in vivo cell tracking," *Trends Biotechnol.*, vol. 28, no. 7, pp. 363–370, 2010.

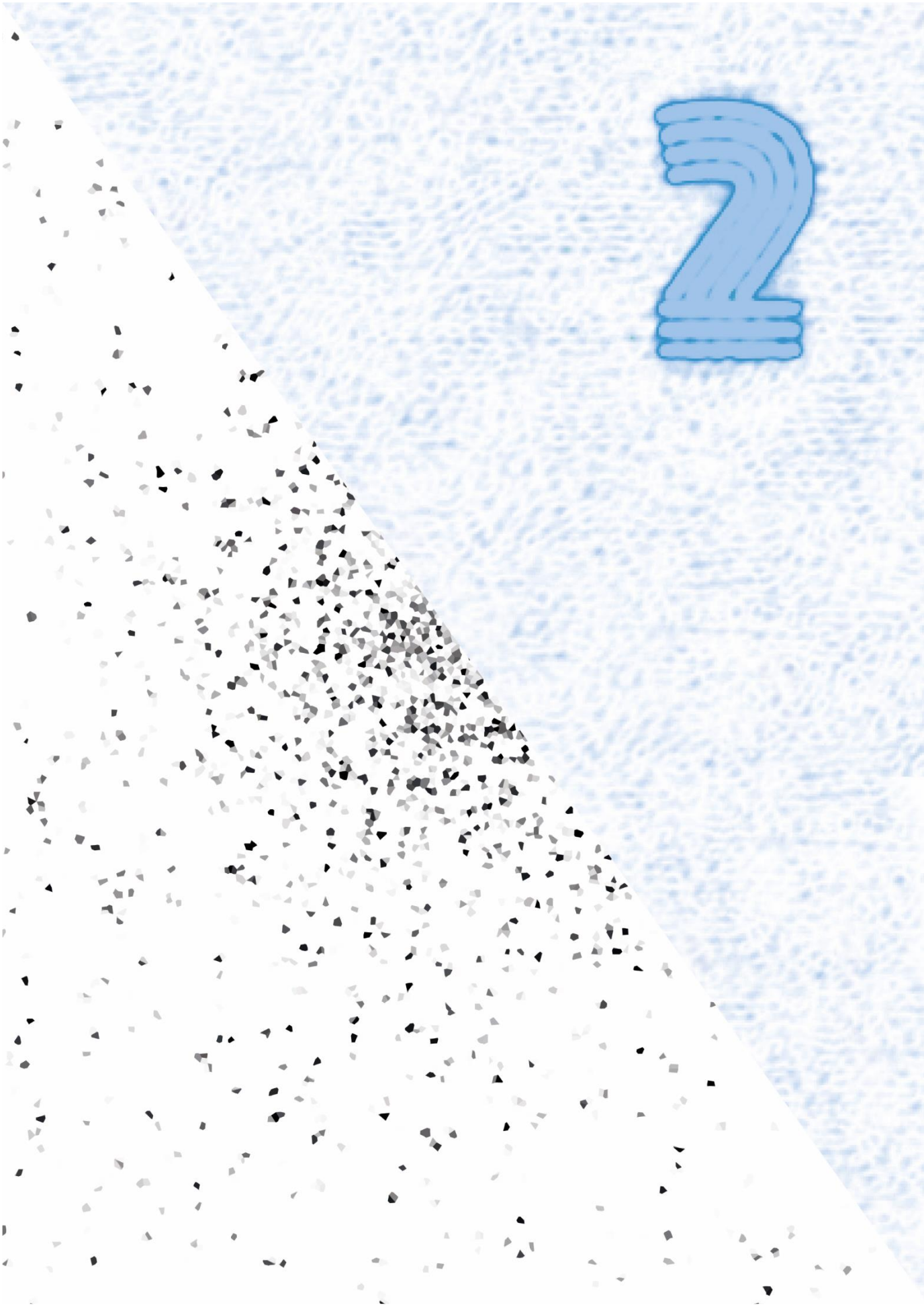

Chapter 2

Compressed Sensing MRI with variable density averaging (CS-VDA) outperforms full sampling at low SNR

Jasper Schoormans,
Gustav J. Strijkers,
Anders C. Hansen,
Aart J. Nederveen,
Bram F. Coolen

Published in Physics in Medicine and Biology, 2020; 65(4):045004

2.1 Abstract

We investigated whether a combination of k-space undersampling and variable density averaging enhances image quality for low-SNR MRI acquisitions. We implemented 3D Cartesian k-space prospective undersampling with a variable number of averages for each k-space line. The performance of this compressed sensing with variable-density averaging (CS-VDA) method was evaluated in retrospective analysis of fully sampled phantom MRI measurements, as well as for prospectively accelerated in vivo 3D brain and knee MRI scans. Both phantom and in vivo results showed that acquisitions using the CS-VDA approach resulted in better image quality as compared to full sampling of k-space in the same scan time. Specifically, CS-VDA with a higher number of averages in the center of k-space resulted in the best image quality, apparent from increased anatomical detail with preserved soft-tissue contrast. This novel approach will facilitate improved image quality of inherently low SNR data, such as those with high-resolution or specific contrast-weightings with low SNR efficiency.

2.2 Introduction

Designing MRI acquisitions always involves a compromise between scan time, image signal-to-noise ratio (SNR), tissue contrast, and spatial resolution. The development of undersampling acquisition schemes in combination with advanced reconstruction algorithms, such as parallel imaging and compressed sensing (CS) has allowed for a significant reduction in scan time, thereby minimizing image distortions (e.g. due to motion) as well as improving patient comfort and cost effectiveness of MRI protocols [1], [2]. In addition, accelerated imaging has allowed application of 3D imaging protocols at isotropic resolution, which would otherwise result in clinically unfeasible imaging times.

In certain cases, however, MRI scans have inherently low SNR, e.g. when aiming for a very high spatial resolution or to achieve a specific contrast weighting, such as in T2-weighted or diffusion-weighted imaging. This limits the application of accelerated imaging as these are thought to further decrease SNR.

In recent years, the optimization of CS acquisition and reconstruction techniques has received considerable attention. With respect to image reconstruction, improved transforms were designed to find the best sparse representation of the images [3]–[5], facilitating higher compression factors and thus a higher degree of undersampling. Although early work in CS theory suggests purely random subsampling of k-space[6], much work has been performed on finding optimal sampling strategies to maximize image quality and robustness to artifacts [7]–[10], and these patterns are not uniformly distributed for MR acquisitions [11], [12].

Despite the research into the optimal distribution of sampling points, one aspect that surprisingly has received little attention is the noise sensitivity of the individual sampling points on the resulting reconstructed images. In light of the relation between wavelet and k-space coefficients [13], we hypothesized that compressed sensing reconstructions are more robust to noise disturbances in high frequency regions. In this work, we therefore aimed to show that employing an undersampling and averaging scheme (without affecting total acquisition time) results in superior image quality as compared to full sampling without averaging.

While this seems unintuitive at first, this study clearly shows the advantage of this approach in a number of steps. First, the rationale and implementation of our new acquisition method of Compressed Sensing with variable averaging (CS-VDA) is presented, combined with a noise-optimal weighted l2-norm in the CS reconstruction. It can be shown that the weighted l2-norm, considering the number of averages for every line, is a least-squares optimizer for this reconstruction problem.

In simulations, we were able to show that our new CS-VDA approach, given equal total scan time, provides superior image quality to fully sampled data. To further

demonstrate the performance of our CS-VDA approach, we performed experiments using prospectively undersampled in vivo brain MRI scans, as well as quantitative T2 MRI of the knee, using clinical 3T MRI.

2.3 Theoretical background

In this paper, we introduce a new compressed sensing sampling method with variable averaging (CS-VDA). Assume we have a fixed sampling pattern, consisting of *n* k-points, but a scan-time budget of *m>n* sampling points, *i.e.* we must distribute these *m* points over *n*, by resampling points in some way. Figure 1 shows three ways to distribute sampling points: by uniform averaging, center-dense averaging; and periphery dense-averaging. For all experiments in this work, k-space was undersampled.

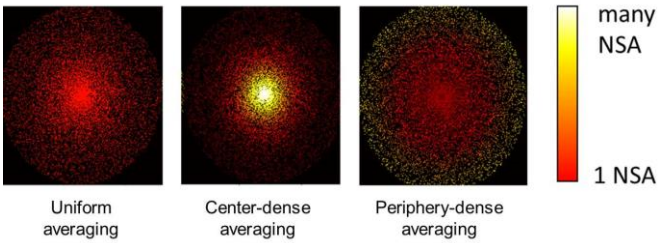

Figure 1. Illustration of the three k-space undersampling & averaging strategies. Shown are the 2 phase encoding dimensions of the 3D k-space; the 3rd dimension is the frequency encoding direction. The k-spaces share the same variable density undersampling pattern, with denser sampling in the center of k-space than in the periphery. However, the three k-spaces differ in how the number of signal averages (NSA) are distributed in k-space, with (A) uniform averaging of all measured k-space points, (B) higher NSA in the center of k-space (center-dense averaging), and (C) periphery-dense averaging. Note that all strategies have the same total number of k-space points.

To obtain a better understanding of the effect of the proposed sampling strategy, we first illustrate the influence of noise in the wavelet domain (using Db-4 wavelets), a commonly used sparsity transform in MRI compressed sensing. Figure 2 shows the wavelet transform of the Shepp-Logan phantom, with complex noise of an equal l_2-norm added in the two following ways: A) the noise was added in the 5 lowest-frequency levels of the wavelet coefficients; B) the noise was added to the highest level of wavelet coefficients only. From the resulting inverse wavelet transforms, it is evident that the addition of noise to the low wavelet levels has a much worse effect on the general quality of the image: the details indicated by the red arrow are much more difficult to distinguish in this case.

While the wavelet transform is commonly used to employ sparsity in compressed sensing, MR images are acquired in k-space. Fig. 3 shows the Shepp –Logan phantom in these two transforms. The MR measurement of a wavelet signal in Cartesian k-

space is the subsequent operation of the inverse wavelet transform (DWT*) and the discrete Fourier transform (DFT), and can be formulated as the matrix $U = DFT\ DWT^*$.

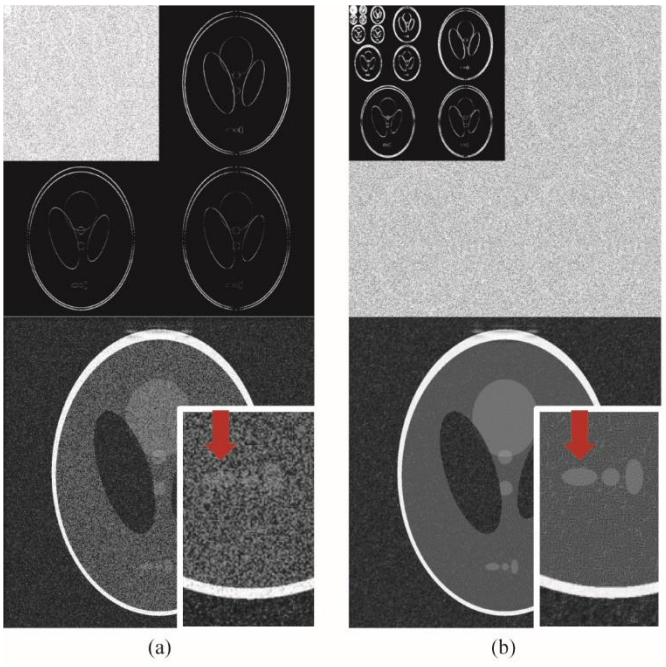

Figure 2. Influence of noise in the wavelet domain on image reconstructions. A) Noise was added to the coarse wavelet coefficients. In B), noise with an equal l_2-norm as in A. is added to the highest wavelet level only. It is clearly visible that resulting details in the reconstruction (red arrow) are much more easily distinguished in B.

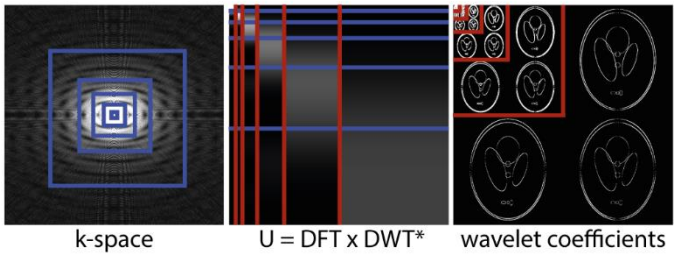

Figure 3. The structure of the MR measurement. The MR measurement of this wavelet signal in Cartesian k-space is the subsequent operation of the inverse wavelet transform (DWT*) and the discrete Fourier transform (DFT), and can be formulated as the matrix U= DFT DWT*. The absolute values are displayed here. Wavelets of increasing coefficients are indicated by red lines, and increased frequencies in k-space are illustrated by blue lines.

This matrix is nearly block-diagonal, with each row representing a k-point measurement. The wavelet coefficients exist in increasing scales, each scale illustrated by a red bounding box. The sections of matrix *U* acting upon each separate wavelet scales are distinguished by the red lines.

In contrast to wavelets, the frequencies in k-space are linearly increasing – not fixed blocks. However, if we show increasing resolutions by blue boxes (1mm, 2mm etc.), this converts to the blue lines in *U*. Now, because measurement *U* is nearly block-diagonal, we can say that wavelets at a given scale are essentially concentrated in square rings of k-space.

Figure 4 shows a one-dimensional toy example, combining the insights from Figs. 2 and 3. Consider a one-dimensional object to be measured: the projection of the Shepp-Logan phantom. Resembling many natural signals, this signal has a sparse representation in the wavelet domain (Fig. 4B). Moreover, it shares the sparsity structure of most natural images: the wavelet coefficients are unequally distributed, with most of the signal energy made up from coarse wavelets, and few non-zero coefficients lying in the higher coefficients. Consider two resampling strategies: we will measure all k-points at least once, but we can choose to measure either the low-resolution (Fig. 4C; case 1), or the high-resolution half (Fig. 4D; case 2) of k-space many times, such that there is effectively no more noise in that half. In the wavelet domain this will result in the following: case 1) noise mostly concentrated in the higher wavelet coefficients encoding for the details; case 2) noise mainly in the lower wavelet coefficients, which encode for coarse image structures and contrast.

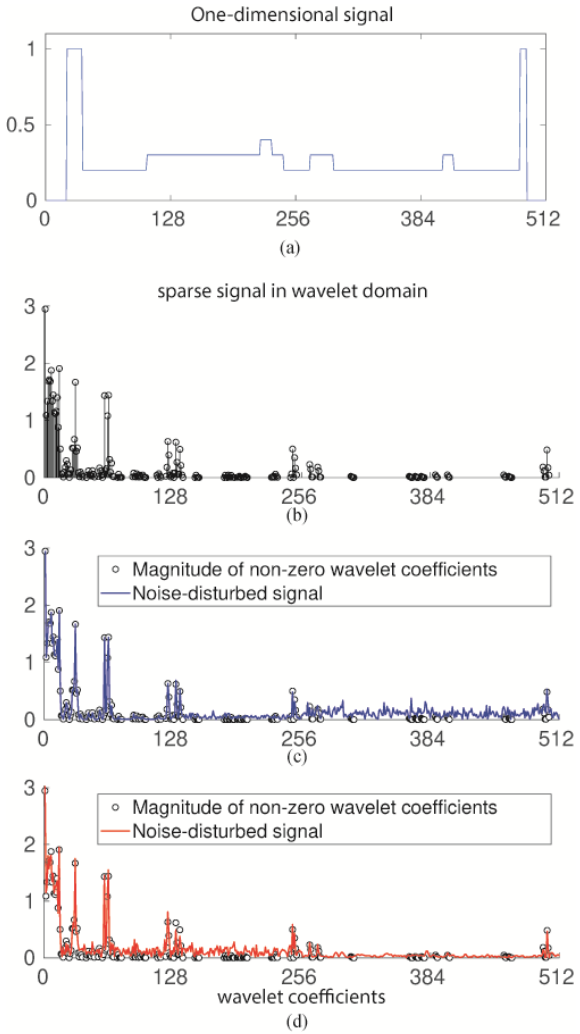

Figure 4. The structure of noise in a 1D MR measurement. A) A one- dimensional signal. B) The wavelet coefficients of this signal. Note the sparsity in the wavelet domain. C) Noise disturbed wavelet coefficients for infinite resampling in the high-frequency half of k-space. Most noise is contained in the higher wavelet coefficients. D) Noise disturbed wavelet coefficients for infinite resampling in the low-frequency half of k-space.

This has the following effects: firstly, as was illustrated in Figure 2, the image quality is considerably worse in the case of coarse-wavelet noise. Secondly, because U is nearly block-diagonal, when the noise is concentrated on the lower wavelet coefficients (case 2), it is projected onto few coefficients in k-space. In contrast, for case 1 the noise contribution will be shared with many more points. Along the same lines as in Adcock *et al.*[14], where the structure of U is the basis of the explanation of the variable-density sampling strategy in CS, this structure can also point in the direction of success in designing an averaging strategy. Thirdly: while one of the key

tenets of CS is incoherence, it has been shown that the MRI measurement matrix is only asymptotically incoherent: In the low-resolution regime, the measurement is very coherent, as indicated by the concentrated coefficients in the columns of *U*. For higher resolutions, *U* becomes increasingly more incoherent. Given these considerations, we theorize that higher frequency k-points are more robust to noise, as the CS theory is more applicable in this regime.

It is evident that the toy example given in Fig. 4 is extreme: the examples given correspond to the unrealistic limit of infinite resampling. A full theoretical explanation of the effects, given realistic sampling numbers, is outside the scope of this paper. However, the behavior described in these toy examples suggests that resampling of points should be focused on the low resolution, coherent, k-space. **Therefore, we predict that for low SNR measurements, unevenly distributing averages with more averages in the low frequencies of k-space will result in superior image quality, even compared to full sampling.** In this paper, we have investigated three types of averaging distributions (Figure 1). A full investigation over the range of distributions, and its dependence, on SNR, resolution, sparsity structure etc. is outside the scope of this work. This paper introduces the concept, and argues for CS-VDA in certain low-SNR applications. The remainder of this will work focus on simulations and prospective measurements of the CS-VDA strategy.

Acquisition strategy

For all experiments in this work, a randomly generated variable density [1] undersampling pattern was generated, according to the probability density function

$$P(r_{\mathrm{k}}) = c + (1 - r_{\mathrm{k}})^4, \tag{1}$$

where r_{k} is the distance to the k-space center. The scaling factor c was chosen such that

$$\int P(r_{\mathrm{k}}) dr_{\mathrm{k}} = \frac{N_k}{R}, \tag{2}$$

i.e. the total number of k-space samples for a fully sampled scan N_k divided by the undersampling factor R. The center ten percent of k-space is always fully sampled (i.e. $P(r_k)$ is defined as 1). In every undersampled scan, the total number of measured k-space samples was kept identical: N_k. This implies that the total acquisition times of undersampled and fully sampled scans were equal. Thus, for the undersampled scans, k-space points could be averaged since there are more readouts than available k-space positions. This averaging in k-space was done in one of the following three ways (Fig. 1):

i) Uniform averaging

Every sampled k-space point was averaged an equal number of R times, with R an integer number.

ii) Center-dense averaging

Averaging was denser in the k-space center, *i.e.* more averages were taken in the center of k-space, and fewer in the periphery. The number of signal averages (NSA) was determined using the sampling probability density

$$\mathrm{NSA}(r_\mathrm{k}) = \mathrm{N}_\mathrm{max}(c + (1 - r_\mathrm{k})^p), \tag{3}$$

where p determines the distance-dependent sampling. In this work, p was chosen to be 4, c similar as the sampling distribution as in Equation 1, and the scaling factor N_{max}such that the total number of acquisitions equals

$$N_k = \int \mathrm{NSA}(r_\mathrm{k}) P(r_\mathrm{k}) dr_\mathrm{k}\,. \tag{4}$$

iii) Periphery-dense averaging

Fewer averages were taken in the center, and more in the periphery, according to

$$\mathrm{NSA}(r_\mathrm{k}) = \frac{1}{\beta + (1 - r_\mathrm{k})^p}\,, \tag{5}$$

where β is a normalization constant calculated with Eq. 4. For both center-dense and periphery-dense averaging $\mathrm{NSA}(r_\mathrm{k})$ was rounded off to its nearest integer number.

The weighted l_2-norm

Noise in k-space can be modeled as a normally distributed stochastic variable $N(0, \sigma^2)$ with zero mean, and a standard deviation σ independent of k-space location [15]. The maximum likelihood estimator of independent and identically normally distributed data is the least-squares estimator, which is related to the data fidelity term

$$|F_u S\boldsymbol{m} - \boldsymbol{y}|_2^2 = (F_u S\boldsymbol{m} - \boldsymbol{y})^*(F_u S\boldsymbol{m} - \boldsymbol{y}), \tag{6}$$

where F_u is the undersampled discrete Fourier transform operator, is a matrix containing the coil sensitivities, $\boldsymbol{m}$ is the image vector, and $\boldsymbol{y}$ is the multichannel undersampled k-space. However, in the case of non-uniform averaging in k-space, the assumption of identical noise variance per k-space point is violated. In this case, the maximum likelihood estimator is given by the weighted least-squares estimator

$$|F_u S\boldsymbol{m} - \boldsymbol{y}|_{2,W}^2 = (F_u S\boldsymbol{m} - \boldsymbol{y})^* W (F_u S\boldsymbol{m} - \boldsymbol{y}), \tag{7}$$

where W denotes the variance-covariance matrix. Assuming independent noise, the covariances are zero. From the sample mean, we can estimate the variances

$$\sigma_i^2 = \frac{\sigma_0^2}{n_i}\,, \tag{8}$$

where n_i is the number of averages for the i^{th} k-point, and σ_0 is the variance for a single average. The weighting matrix then becomes

$$W = \frac{1}{\sigma_0^2}\begin{bmatrix} n_1 & \cdots & 0 \\ \vdots & \ddots & \vdots \\ 0 & \cdots & n_N \end{bmatrix}, \tag{9}$$

where N is the total number of measured k-points. Of note, a similar weighting matrix in the l_2-norm has been proposed previously for general noise uncertainties [16]. In this work, we use the weighted l_2-norm in combination with the l_1-norm, according to

$$\hat{\boldsymbol{m}} = \arg\min_{\boldsymbol{m}} \left| W^{\frac{1}{2}}(F_u S\boldsymbol{m} - \boldsymbol{y}) \right|_2^2 + \lambda |Q\,\boldsymbol{m}|_1\,, \tag{10}$$

with λ a regularization parameter and Q a sparsifying transform, *e.g.* the wavelet transform or a finite-difference operator.

Noise variance and the l_2-norm

The averaging schemes described in Equations 3,4,5 will influence the noise variance and lead to different data fidelity terms. To keep the balance with the l_1-norm. the λ in Equation 10 is adapted to the expected l_2-norm:

$$\lambda_{mod} = \alpha\, \lambda_0 \tag{11}$$

where α is the regularization adaption term.
The expected data fidelity in Equation 10 is given as:

$$\mathbb{E}(l_2^2) = \mathbb{E} \sum_{i=1}^{N} \left| W_i^{\frac{1}{2}}(y_i - y_{i,0}) \right|^2\,, \tag{12}$$

Where y_i is the averaged measurement of the i^{th} k-space line, and $y_{i,0}$ is the true value of that k-space line. This simplifies to:

$$\mathbb{E}(l_2^2) = \sum_{i=1}^{N} \mathbb{E}\big(W_i(y_i - y_{i,0})^*(y_i - y_{i,0})\big), \tag{13}$$

and simplifies further to:

$$\mathbb{E}(l_2^2) = \sum_{i=1}^{N} \mathrm{W_i} \cdot \Big(\mathbb{E}(y_i^* y_i) + y_{i,0}^* y_{i,0} - 2y_i^* \mathbb{E}(y_i)\Big). \tag{14}$$

As we assume white noise, the expected values of the measurement $\mathbb{E}(y_i) = \mathrm{y_{i,0}}$ and $\mathbb{E}(y_i^* y_i) = y_{i,0}^* y_{i,0} + |\sigma_i|^2$, Equation 12 becomes

$$\mathbb{E}(l_2^2) = \sum_{i=1}^{N} \mathrm{W_i} \cdot |\sigma_i|^2 = N\,. \tag{15}$$

From the definition of the weighting matrix in Equation 9, the regularization is then be scaled with:

$$\alpha = \frac{\mathbb{E}(l_2^2)}{\mathbb{E}(l_2^2)_{full}} = \frac{N}{N_0} = \frac{1}{R}, \tag{16}$$

where N_0 is the number of samples for a fully sampled measurement.

2.4 Methods

Retrospective undersampling of phantom data

MRI was performed on a 3T clinical MRI scanner (Philips Ingenia, Best, the Netherlands). For retrospectively undersampled experiments, we chose to scan a grapefruit phantom to maximize the presence of detailed structures. A high-resolution 2D T_1-weighted fast-field echo scan of the grapefruit was performed using the following parameters: flip angle (FA) = 15°, TR = 15.6 ms, TE = 4.2 ms, FOV= 128×128 mm^2, matrix size = 512×512, resolution = 0.25×0.25 mm^2, and slice thickness = 1 mm. This fully sampled scan was performed with 50 averages for every k-space point to allow full flexibility in retrospective undersampling of k-space points and NSA per point. Total scan time was 6 minutes and 39 seconds. This dataset was retrospectively undersampled and averaged for R = 1, 2, 3, 4, and 5 in the above described three ways. Four different regularization parameters λ were tested (0.0005, 0.005, 0.05, and 0.5). After reconstruction, images were normalized with the *normalize* function in the BART toolbox [17]. Scan quality was assessed by fitting a sigmoid perpendicular to the air/fruit-skin interface, with the Matlab *lsqnonlin* fit routine. For every reconstruction, this was done for ten lines. The sigmoid width parameter was used as a measure for apparent sharpness [18].

To further investigate the effect of the weighting matrix, a second scan of the grapefruit was performed with the same settings as described above. The k-space data was subsampled at R = 5 with a center-dense variable density pattern. The center k-space was averaged 5 times more than the periphery. Data was reconstructed in 4 different ways, *i.e.* using an l_2-norm, a weighted l_2-norm, an l_2-norm plus the l_1-norm, and finally, our proposed weighted l_2-norm combined with an l_1-norm (Eq. 10). For both methods, 30 iterations of the non-linear conjugate gradient algorithm were used and the optimal λ was determined by the l-curve method [19]. The noise spectral density was calculated in a noise-only region-of-interest, outside the fruit.

Prospective undersampling of in vivo human brain data

The institutional review board of our hospital approved this study. All four healthy volunteers (2m, 2f, age=26-35) gave written informed consent for participating in this study.

For prospective undersampling of k-space, an in-house developed scanner software patch was used to sample user-defined k-space trajectories. An inversion prepared 3D T1-weighted fast-field-echo brain scan was performed at high isotropic spatial resolution using a 16-channel head coil and the following sequence parameters: FA = 5°, TR = 7.9 ms, TE = 2.6 ms, inversion delay time (TI) = 1000 ms, echo train length = 120, FOV= 210×210×58 mm^3, matrix size = 304×302×91, resolution = 0.7×0.7×0.7 mm^3. For each volunteer, five different k-space patterns were measured, *i.e.* one fully sampled k-space, uniform averaging with either R = 3 or 5, and center-dense averaging with R = 3 and 5. Total scan time was 6min24s for all scans. Furthermore, a fully sampled lower resolution acquisition with a resolution of 1×1×1 mm^3 and uniform NSA = 2 was acquired. Scans were assessed visually for image sharpness and signal-to-noise.

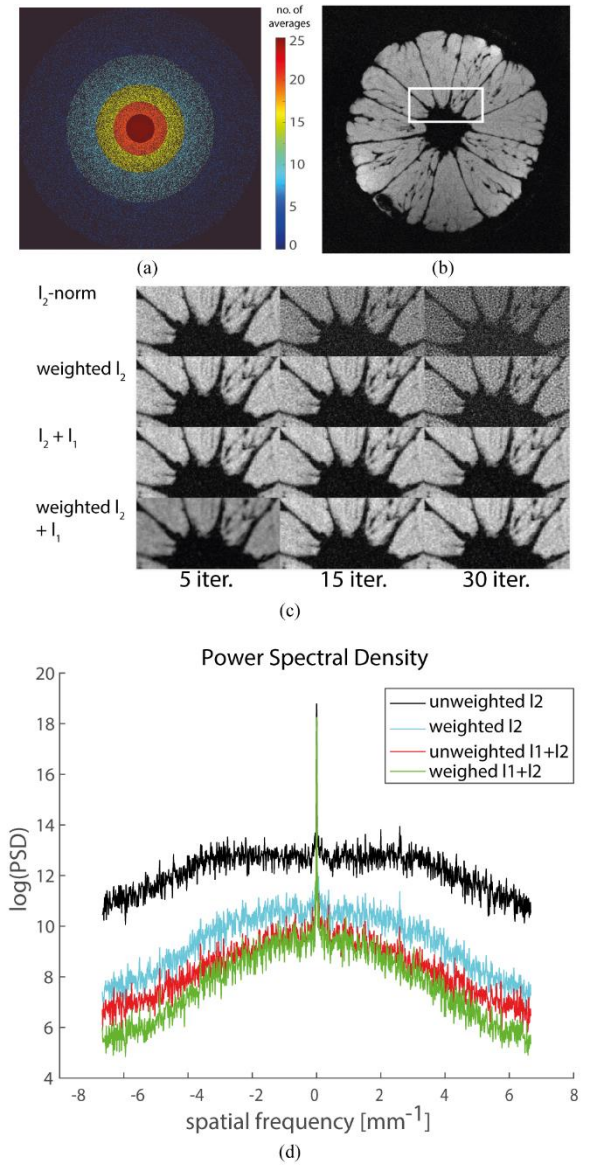

Figure 5 Imaging of grapefruit using different reconstruction methods. (A) Center-dense undersampling of k-space. (B) Middle slice of a fully sampled scan with NSA = 50. (C) Magnifications of the regions of interest, shown in A, with different reconstruction strategies and number of iterations. (D) Noise power spectral density for the four methods. The use of the noise weighting matrix reduces the power spectral density over the full range of spatial frequencies, both without inclusion of l_1-norm regularization (black to blue) and with l_1-norm regularization (red to green).

Prospective undersampling of in vivo human knee data

A T2-prepared fast-field echo knee scan of a healthy female volunteer (26y) was performed at 3T, using a 16-channel knee coil. The sequence was adapted from

Colotti *et al.* [20], modified with selective water excitation, and a segment-time increased from 700 to 800 ms. Fully sampled and CS-VDA ($R = 3$) data were scanned in an interleaved fashion, for T2-echo preparation times of 0, 23, 38 and 58 ms. Further scan parameters were: FOV = 140x150x171 mm^3, resolution: 0.8x0.8x0.8 mm^3, FA = 15 degrees, TE/TR = 3.4/6.9 ms, TFE-factor = 100. Total scan time amounted to 4 x 4m51s per sampling method. The reconstruction parameter λ was optimized for every separate T2-prepared acquisition: a value of λ=0.001 was used for TE = 0, and $\lambda = 0.005$ for all other scans. Three-dimensional rigid registration and a pixel-wise T2 fits were performed with Matlab (R2015b).

Image reconstruction

All image reconstructions were performed in Matlab (R2015b, The MathWorks, Natick, 2014). Both full and undersampled data went through the same reconstruction pipe-line. K-space data was loaded and preprocessed with the MRecon toolbox (version 5.3.19, Gyrotools, Zürich, Switzerland). The data was pre-whitened and sensitivity maps were calculated with the ESPiRIT method in the BART toolbox [21][17]. Slices were reconstructed in parallel after an iFFT in the frequency encoding direction. Equation 10 was solved by a non-linear conjugate gradient algorithm. The number of iterations (20) was carefully chosen by visual comparison to prevent noise amplification [22] and a restart strategy with 3 outer iterations was used. A wavelet transform was used as a sparsifying operator for the *in vivo* scans, and a total-variation constraint was used for the grapefruit scans. Reconstruction time was 5 minutes for a full reconstruction of a 3D dataset on a standard Dell workstation (3.5 GHz, 32 GB memory), with a Geforce Titan XP GPU.

2.5 Results

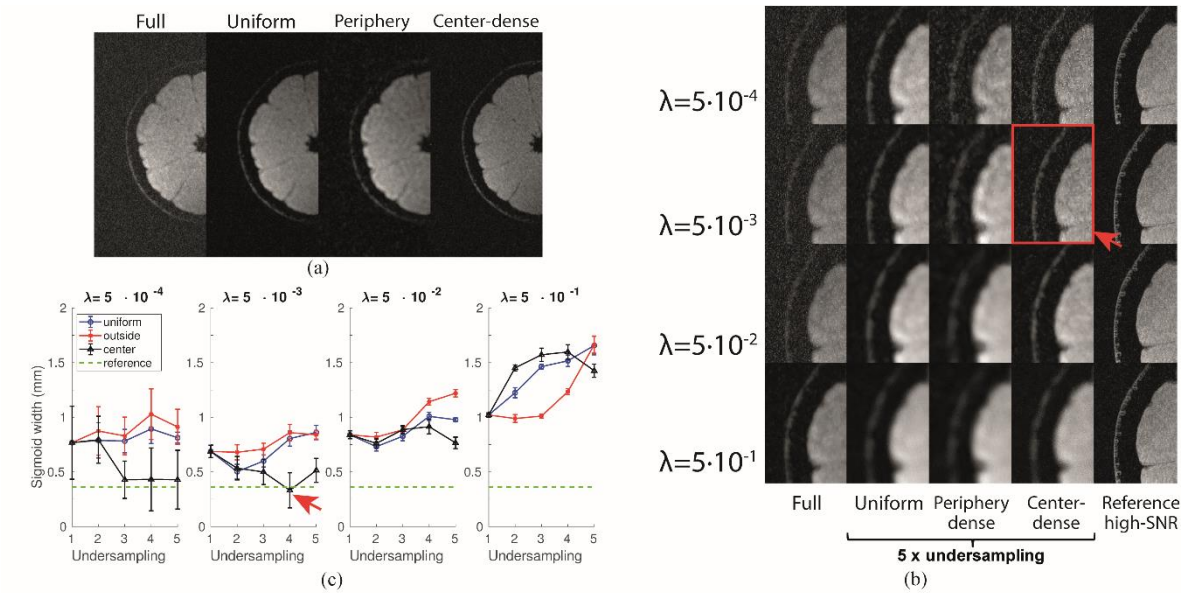

Figure 6. Comparisons of different CS-VDA sampling schemes. (A) half of a center slice of the grapefruit, five times undersampled (R = 5), reconstructed using uniform, center-dense, and periphery-dense k-space averaging in comparison to the fully sampled scan. (B) Enlarged sections of the reconstructed images with varying regularization parameter λ. Note the thin layer covering the grapefruit skin, which is sharpest for the center-dense averaging scheme with $\lambda = 5\times10^{-3}$. Undersampled scans have better signal-to-noise than the fully sampled scan. (C) Mean calculated sigmoid widths for different sampling and reconstruction parameters. The fully-sampled scan corresponds to undersampling = 1. The error-bars indicate the standard deviation of 10 measurements. The lowest sigmoid width, and the corresponding image are indicated by red arrows. This indicates the best reconstruction, however, compared to a fully sampled references at high SNR (10 times longer scan time), there is still a loss of resolution apparent in the skin.

Figure 5 illustrates the beneficial effect on image quality of the weighted l_2-norm in comparison to the traditional unweighted l_2-norm. Figure 5B shows the middle slice of the fully sampled 3D dataset of the grapefruit with NSA = 50 (experiment 1), providing a reference to which the reconstructions with the undersampled and center-dense NSA k-space pattern (Fig. 5A) can be compared. Magnifications of the regions of interest in Fig. 5B with different reconstruction strategies and iteration numbers are shown in Fig. 5C. Upon visual inspection, the reconstructions with l_2-

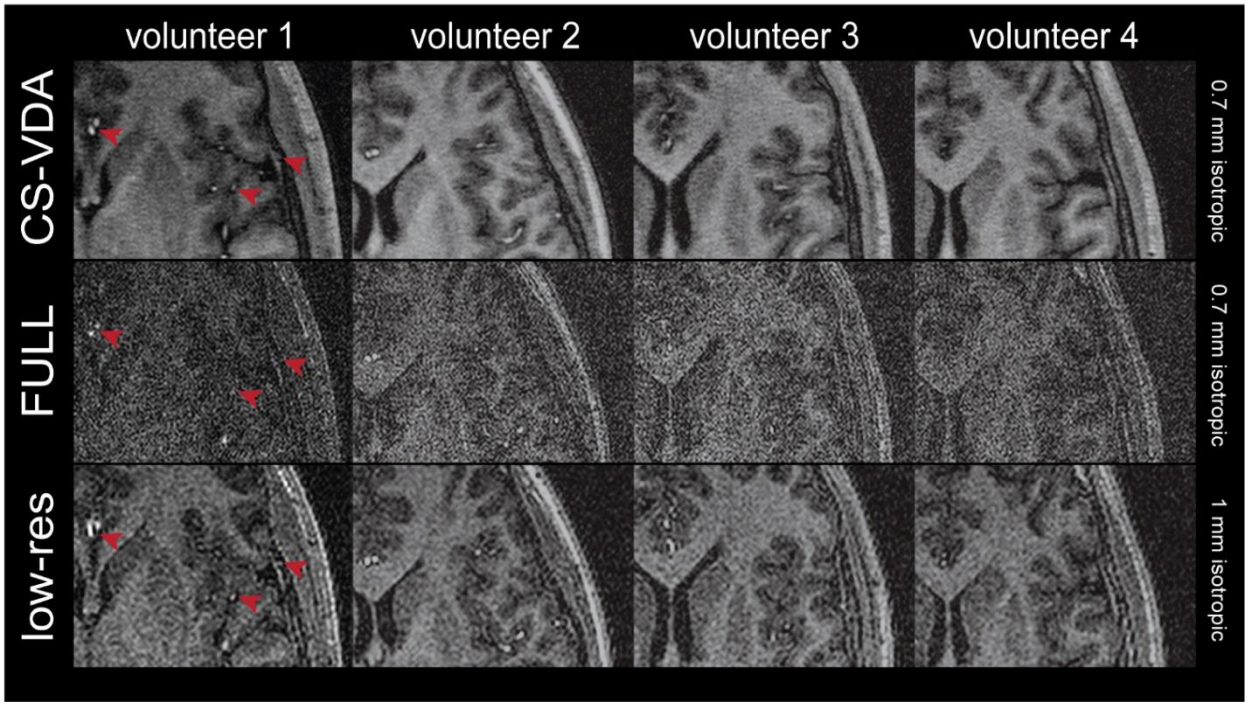

Figure 7. Inversion prepared 3D T1-FFE brain scans of the four volunteers scanned with (top) center-dense averaging (R = 3) and 0.7 mm isotropic voxel size, (middle) fully sampling at 0.7 mm isotropic voxel size, and (bottom) full sampling at 1 mm isotropic voxel size. All scan times were equal. The red arrows indicate small anatomical details in the brain.

norm + l_1-norm and weighted l_2-norm + l_1-norm (Eq. 10) with 15 and 30 iterations resulted in the best image quality with the lowest noise. This visual assessment can be objectified by comparing the power spectral density calculated from a background-only (noise) region in the image for the different reconstruction methods (Fig. 5D). The use of the noise weighting matrix W reduced the noise power over the full range of spatial frequencies. In CS reconstructions that included the l_1-norm, the benefit was visually less apparent, but still substantial as is shown in Fig. 5D.

Figure 6A shows half of a center slice of the grapefruit, reconstructed from five times undersampled (R = 5) data using uniform, center-dense, and periphery-dense averaging in comparison to the fully sampled scan. Note that based on visual inspection, we used 5 (instead of only 1/50) averages to define the low SNR fully sampled scan. For a fair comparison, all reconstructions, including the fully sampled scan, were performed using Eq. 10 with $\lambda = 5\times10^{-4}$ and equal total number of samples. In Fig. 6B, reconstructions are shown for varying regularization parameter λ. The width of the sigmoid-curves fitted to the air/grapefruit-skin interface (Fig. 6C) is

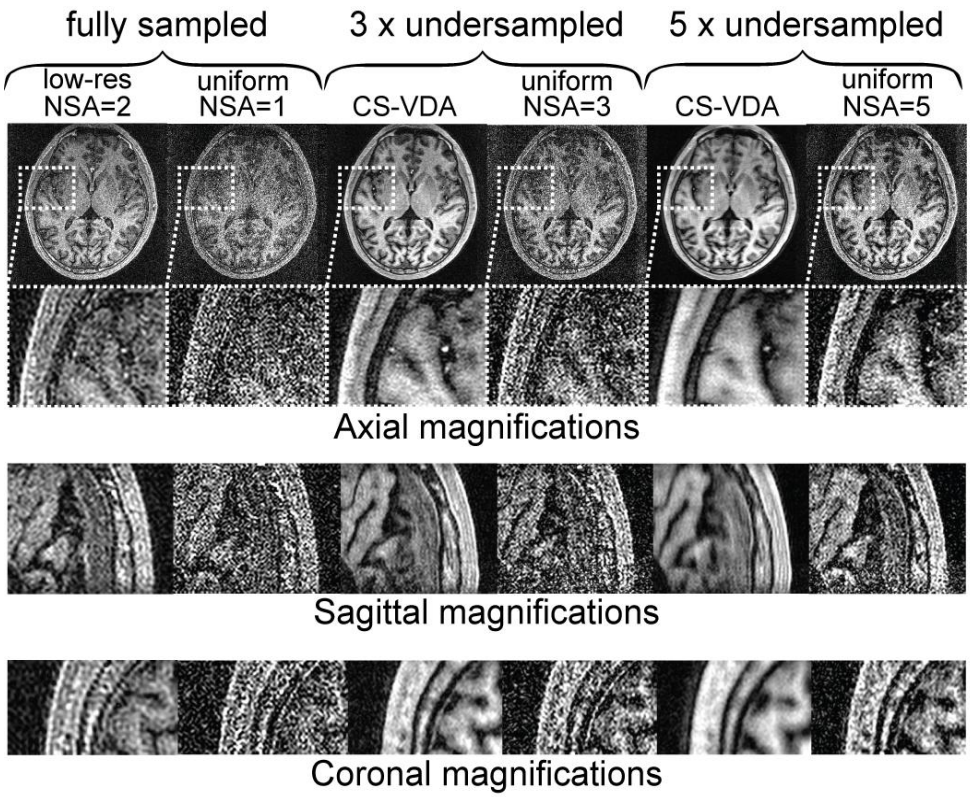

(a)

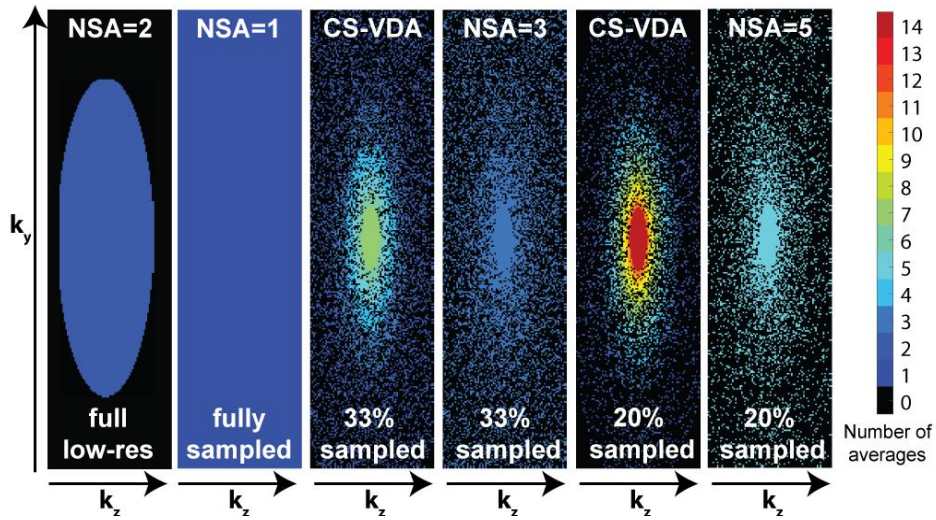

Figure 8. Inversion prepared 3D T1-FFE brain scans of a single volunteer acquired with 6 sampling schemes of equal total scan times. (A) Reconstructed images with magnifications in the three orientations. (B) Corresponding k-space sampling patterns. Colors indicate the number of averages for every k-space line**.**

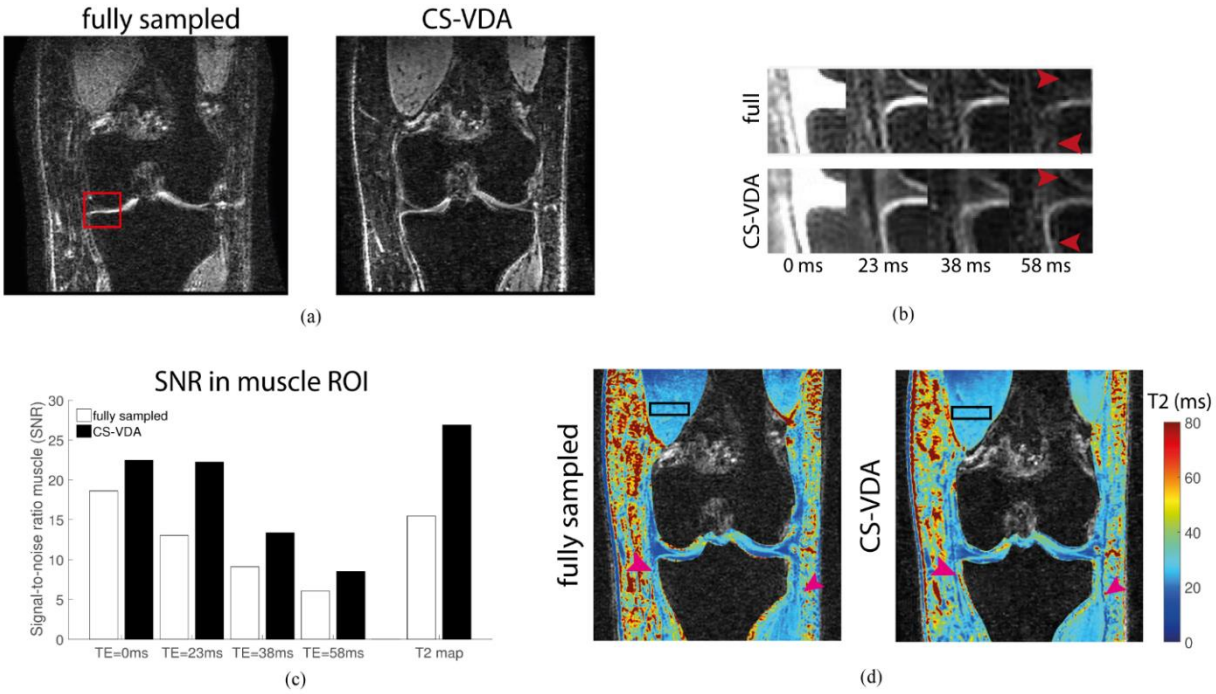

Figure 9. T2 mapping experiment. (A) Coronal slice of a T2-prepared acquisition with TE=58 ms. Red arrows indicate loss of details in the fully sampled acquisition, with respect to the CS-VDA acquisition (B). Zoomed-in section of image for four different echo times, corresponding to the red arrow with the white star. Loss of structural detail in the fully sampled acquisitions is apparent for TE=38 ms and TE=58 ms. (C) Signal-to-noise ratio in a section of the muscle (box of subplot a). For all echo times and for the T2 map, the SNR is higher in CS-VDA compared to full sampling (D) T2-maps for the cartilage. Arrows indicate regions of difference between the two acquisitions: the high T2 of fluid and the delineation of the muscle is represented more clearly in the CS-VDA T2 map.

lowest, *i.e.* the interface is sharpest for the center-dense sampling scheme with $\lambda = 5\times10^{-3}$ and $R = 4$. This approach results in a sharper interface than the corresponding fully-sampled scan, approaching the sharpness of a very high-SNR reference. Only for the higher values of λ, fully sampled scans are sharper than the undersampled counterparts, but this is due to over-smoothing of all images (Fig. 6B).

For the *in vivo* experiments, both a CS-VDA brain scan with center-dense averaging ($R = 3$), as well as a fully sampled scan were acquired at 0.7 mm isotropic resolution. In addition, a low-resolution (1 mm isotropic) fully sampled scan was acquired. All acquisitions were performed in equal total scan time. Because of the – deliberately chosen – low flip angle of the read-out train, images resulting from the fully sampled scan were noisy with almost no visible anatomical details (middle row, Fig. 7). In comparison, the CS-VDA scans with center-dense averaging showed considerably better signal-to-noise (top row, Fig. 7) and clearly displayed detailed anatomical features such as vessels and outlines of sulci.

To prove that the improved signal-to-noise and image sharpness was due to the specific k-space sampling pattern with center-dense averaging and not merely a signal smoothing effect, we also scanned with lower resolution in the same scan time (bottom row, Fig. 7). As expected, lower resolution scans did not present the level of anatomical detail as was seen for the images acquired with the CS-VDA approach.
Figure 8A shows scans of one volunteer for varying degrees of undersampling (full sampling, R = 3 and 5) and magnifications in three orientations. Corresponding k-space sampling patterns are shown in Fig. 8B. Again, fully sampled scans at low and high resolution as well as scans with uniform k-space averagingwere noisy and lack anatomical detail. However, the variable density averaging images have much better image sharpness and signal-to-noise. For R = 5 though, images appear slightly smoothed, particularly for the coronal cross section. Figure 9 shows results from the T2-mapping knee acquisitions. The images in Fig. 9A corresponds to the highest T2-prepared echo time (TE = 58 ms), which has the lowest SNR. Red arrows indicate detailed structures of cartilage and muscle that are recovered in CS-VDA, while appearing not sharp (or lost in the noise) in the fully sampled acquisition. Fig. 9B *shows* the loss of details in a zoomed-in section, corresponding to the red box in subplot A, occurring at the later echo times in the fully sampled acquisition. This leads to underestimation of T2, as shown in Fig 9C. Finally, the calculated SNR values of a ROI in the muscle reveals an increased SNR for CS-VDA, for all acquired echo times, as well as for the reconstructed T2-map. The calculated T2 for muscle was (mean ± standard deviation) T2 = 26.1±0.9 ms (CS-VDA); T2 = 25.0±1.6 ms (fully sampled). Supplementary figure S1 provides an animated gif, covering a range of slices of the same acquisition.

2.6 Discussion

In this study, we demonstrated that image quality in SNR-deprived volumetric scans can be improved by using both k-space undersampling and averaging, combined with CS reconstruction while maintaining the same total scan time as a fully sampled scan. We introduced and tested three different undersampling and averaging methods. The averaging strategies were: uniform averaging; more averages in the center and more averages in the periphery of k-space. We found that in terms of image quality, most benefit was gained by center-dense averaging. In Fig. 6, the three different strategies are employed for a retrospectively undersampled acquisition of a grapefruit. The measured thickness of the fruit skin, a surrogate for image sharpness, was lowest for the center-dense averaging at four times scan acceleration. Uniform averaging also impacted the resolution positively, compared to full sampling with only one average.

Deterministic variable averaging has been used as an alternative to a low-pass filter [23], [24], with an SNR benefit that was found to be 17 percent in 31P-MRI [25]. The deterministic approaches do not average multiply sampled points, but rather sum the points as to achieve low-pass filtering to reduce Gibbs ringing. In contrast to these earlier works, we do average all sampled points, and combine it with a compressed sensing acquisition. Instead of Gibbs ringing removal, we achieve image quality improvements explained by the noise characteristics and the wavelet-Fourier relation. The link between wavelet-domain sparsity and k-space was used to design the Subband Compressed Sensing with Quadruplet Sampling method [13], where parallel imaging was used in the low-frequency k-space. As opposed to CS-VDA, this method requires high SNR and high contrast.

Since variable k-space averaging introduces a non-uniform noise variance, we included a weighted l_2-norm in the image reconstruction minimization function. This led to a significant improvement in image quality, in agreement with Johnson *et al* [16] who introduced the l_2-norm weighting to improve image reconstructions of data with unfavorable contrast evolutions in k-space. In the presence of an l_1-norm, the noise reduction gain when using a weighted l_2-norm was smaller but still significant and therefore we recommend the addition of the weighted l_2-norm for these types of acquisitions. Note that for uniform sampling, the added weights have no effect, since they are the same for all k-space lines. At low iteration numbers, the weighted l_2-norm + l_1-norm for the center-dense acquisitions (Fig. 5C) resulted in more blurring as compared to the non-weighted versions. The reason for this is that at the start of iterative reconstruction – when convergence has not been reached yet – there is more weight on the center of k-space. This initially leads to some blurring, which is resolved at higher iteration numbers.

In our experiments, the number of signal averages was based on a power function (Eq. 3). The optimal distribution of averages throughout k-space will depend on several factors, such as the specific sampling distribution, noise level, matrix size, etc. Such optimization may be a topic of future research. Supplemental Figure 2 shows the effect of varying p on different image quality measures for the R = 4 case in Figure 6. These results justify the choice for $p = 4$ in Eq. 3 to create the center-dense averaging distribution.

As an *in vivo* proof of concept, we applied the center-dense averaging strategy to high-resolution 3D imaging of the human brain (Figs. 7 and 8). The quality of images acquired with center-dense averaging method was significantly better than fully sampled images acquired in the same scan time. Image quality in terms of sharpness and signal-to-noise was also better than fully sampled images at lower resolution, which shows that center-dense averaging is not equivalent to low-resolution high SNR imaging. Nevertheless, the distribution of points should remain balanced between the k-space center and periphery and we have observed that $R = 4$ resulted in the sharpest images (Fig. 6). While the proposed approach is well-suited to counterbalance decreased SNR of high-spatial resolution acquisitions, effective resolution can be decreased as a result of motion. To achieve true high resolution images, strategies to minimize physical motion or apply prospective motion correction could be considered [26]. Although we did not investigate this explicitly, an additional benefit of center-dense averaging could be increased motion robustness. While this might explain some of the quality improvement in the brain images, the sharpness improvements in retrospective grapefruit scans, which were not influenced by any motion, show that this is not the only factor. We here again want to explain that 3D brain scans were acquired purposely with a low flip angle resulting in low SNR images for the fully sampled scans. Although we are aware that better image quality for the fully sampled scans can be obtained with a higher excitation flip angle, these SNR-deprived scans provided a good starting point to demonstrate the improvement in image quality resulting from our non-uniform k-space averaging approach.

An application in a clinically relevant sequence is the T2-mapping experiment of the knee we performed, shown in Fig. 9. The images acquired with a high T2 weighting are naturally SNR-deprived. We noticed that for the higher T2-prepared acquisitions, which suffer from low SNR, CS-VDA recovered details that were lost in the noise in the fully sampled acquisition. Figure 9B shows an example of an image detail that is being lost in the fully sampled acquisition, for decreasing SNR. This behavior could lead to the loss of high T2 values in a T2-map. The CS-VDA T2 map showed regions of high T2, and a sharp delineation of muscle, which were not visible on the fully sampled T2-map. Furthermore, we saw an increase in SNR in all acquired images, and the calculated T2-map, when using CS-VDA. While the signal shows a convincing

decay curve, and a T2 estimate that is in agreement with both methods, the noise behavior is not as straightforward, owing to the optimized l_1 constraints. Therefore, the noise is not necessarily constant over the decay times, which reflects on the SNR values.

The effects on the SNR arising from accelerated imaging are well understood for parallel imaging [29], however, the noise penalty in CS is more complicated for several reasons. First, the spatial distribution of sampling points in a typical CS measurement gives rise to colored noise [30]. Secondly, l_1 regularization inherently leads to denoising, the effect of which depends greatly on the chosen regularization parameter and which makes it difficult to quantify SNR in CS reconstructed images. While application of CS in MRI is one of the most promising applications of this technique, research into the effects of noise on CS reconstruction has been mostly limited to the mathematical literature [31]–[33]. Our work now shows that the link between the sparsifying transform and the sampling transform can be used to design sampling methods that include averaging of k-space points. These insights can be valuable in other imaging fields where CS is used with binary sampling, such as fluorescence microscopy [34], and other Fourier-based sampling modalities, such as radio interferometry [35].

Our proposed CS and variable density averaging method will be beneficial specifically when dealing with acquisitions that have low SNR per unit of time and may otherwise require regular averaging to achieve sufficient image quality. This is for instance the case when sequences are designed to achieve a specific contrast weighting at the expense of SNR. While in the current manuscript we used T2 prepared imaging as an example (Figure 9), other applications could be diffusion-, T1ρ- or ASL-based imaging protocols that are affected by similar low SNR acquisitions. Finally, we believe our approach may significantly improve applications with an inherently low sensitivity, such as non-proton MRI or low-field MRI (< 0.5T), with the latter gaining much interest because of its low costs and possibility to use as an intra-operative imaging modality [27]. A well-known problem in CS literature is to find objective metrics for image quality [28]. Frequently-used measures like the structural-similarity index or the mean squared error did not work well in our study because these are strongly biased by the noise characteristics of the images and there is no gold-standard image for comparison for the in-vivo data. For this reason, we chose to evaluate image sharpness as the main quality measure by determining the width of the air/grapefruit-skin interface.

In conclusion, we implemented 3D Cartesian k-space undersampling with a variable number of k-space averages. Additionally, we incorporated the weighted l_2-norm into a CS reconstruction. We have shown that variable center-dense k-space averaging outperforms fully sampled k-space sampling for low-SNR MRI

acquisitions. We think this novel approach will facilitate improved image quality of inherently low SNR data, such as those with high-resolution or specific contrast-weightings with low SNR efficiency.

2.7 References

[1] M. Lustig, D. Donoho, and J. M. Pauly, "Sparse MRI: The application of compressed sensing for rapid MR imaging," Magn. Reson. Med., vol. 58, no. 650, pp. 1182–1195, 2007.

[2] D. J. Larkman and R. G. Nunes, "Parallel magnetic resonance imaging," Phys. Med. Biol., vol. 52, no. 7, pp. R15–R55, Apr. 2007.

[3] S. Ravishankar, "Magnetic resonance image reconstruction from highly undersampled k-space data using Dictionary Learning," IEEE Trans. Med. Imaging, vol. 30, no. 5, pp. 1028–1041, 2011.

[4] X. Qu, D. Guo, B. Ning, Y. Hou, Y. Lin, S. Cai, and Z. Chen, "Undersampled MRI reconstruction with patch-based directional wavelets," Magn. Reson. Imaging, vol. 30, no. 7, pp. 964–977, 2012.

[5] F. Knoll, K. Bredies, T. Pock, and R. Stollberger, "Second order total generalized variation (TGV) for MRI," Magn. Reson. Med., vol. 65, no. 2, pp. 480–491, 2011.

[6] R. G. Baraniuk, "More is less: signal processing and the data deluge," Sci. Mag, vol. 462, 2011.

[7] F. Knoll, C. Clason, C. Diwoky, and R. Stollberger, "Adapted random sampling patterns for accelerated MRI," Magn. Reson. Mater. Physics, Biol. Med., vol. 24, no. 1, pp. 43–50, 2011.

[8] S. Ravishankar and Y. Bresler, "Adaptive sampling design for compressed sensing MRI," Conf. Proc. ... Annu. Int. Conf. IEEE Eng. Med. Biol. Soc. IEEE Eng. Med. Biol. Soc. Conf., vol. 2011, pp. 3751–3755, 2011.

[9] F. Zijlstra, M. A. Viergever, and P. R. Seevinck, "Evaluation of variable density and data-driven K-space undersampling for compressed sensing magnetic resonance imaging," Invest. Radiol., vol. 51, no. 6, pp. 410–419, 2016.

[10] J. P. Haldar and D. Kim, "OEDIPUS: an experiment design framework for sparsity-constrained MRI," IEEE Trans. Med. Imaging, pp. 1–1, 2019.

[11] B. Roman, A. Hansen, and B. Adcock, "On asymptotic structure in compressed sensing," arXiv Prepr. arXiv1406.4178, no. c, pp. 1–10, 2014.

[12] Q. Wang, M. Zenge, H. E. Cetingul, E. Mueller, and M. S. Nadar, "Novel sampling strategies for sparse MR image reconstruction," Int. Soc. Magn. Reson. Med., vol. 55, no. 3, p. 4249, 2014.

[13] K. Sung and B. A. Hargreaves, "High-frequency subband compressed sensing MRI using quadruplet sampling," Magn. Reson. Med., vol. 70, no. 5, pp. 1306–1318, 2013.

[14] B. Adcock, A. C. Hansen, C. Poon, and B. Roman, "Breaking the coherence barrier: a new theory for compressed sensing," Forum Math. Sigma, vol. 5, p. e4, 2017.

[15] Klaas P. Pruessmann, "Advances in sensitivity encoding with arbitrary k-space trajectories," Magn. Reson. Med., vol. 651, pp. 638–651, 2001.

[16] K. M. Johnson, W. F. Block, S. B. Reeder, and A. Samsonov, "Improved least squares MR image reconstruction using estimates of k-Space data consistency," Magn. Reson. Med., vol. 67, no. 6, pp. 1600–1608, Jun. 2012.

[17] J. I. Tamir, F. Ong, J. Y. Cheng, M. Uecker, and M. Lustig, "Generalized magnetic resonance image reconstruction using the Berkeley Advanced Reconstruction Toolbox," Proc. ISMRM 2016 Data Sampl. Image Reconstr. Work., vol. 2486, p. 9660006, 2016.

[18] H. Greenspan, G. Oz, N. Kiryati, and S. Peled, "MRI inter-slice reconstruction using super-resolution," Magn. Reson. Imaging, vol. 20, no. 5, pp. 437–446, 2002.

[19] P. C. Hansen, "The L-curve and its use in the numerical treatment of inverse problems," Comput. Inverse Probl. Electrocardiology, ed. P. Johnston, Adv. Comput. Bioeng., vol. 4, pp. 119–142, 2000.

[20] R. Colotti, P. Omoumi, G. Bonanno, J.-B. Ledoux, and R. B. van Heeswijk, "Isotropic three-dimensional T 2 mapping of knee cartilage: Development and validation," J. Magn. Reson. Imaging, pp. 1–10, 2017.

[21] M. Uecker, P. Lai, M. J. Murphy, P. Virtue, M. Elad, J. M. Pauly, S. S. Vasanawala, and M. Lustig, "ESPIRiT - An eigenvalue approach to autocalibrating parallel MRI: Where SENSE meets GRAPPA," Magn. Reson. Med., vol. 71, no. 3, pp. 990–1001, 2014.

[22] P. Qu, K. Zhong, B. Zhang, J. Wang, and G. X. Shen, "Convergence behavior of iterative SENSE reconstruction with non-cartesian trajectories," Magn. Reson. Med., vol. 54, no. 4, pp. 1040–1045, 2005.

[23] D. L. Parker, G. T. Gullberg, and P. R. Frederick, "Gibbs artifact removal in magnetic resonance imaging," Med. Phys., vol. 14, no. 4, pp. 640–645, 1987.

[24] J. W. Hugg, A. A. Maudsley, M. W. Weiner, and G. B. Matson, "Comparison of k-space sampling schemes for multidimensional MR spectroscopic imaging," vol. m, pp. 469–473.

[25] R. Stobbe and C. Beaulieu, "Advantage of sampling density weighted apodization over postacquisition filtering apodization for sodium MRI of the human brain," Magn. Reson. Med., vol. 60, no. 4, pp. 981–986, 2008.

[26] M. Zaitsev, J. Maclaren, and M. Herbst, "Motion artifacts in MRI: A complex problem with many partial solutions," J. Magn. Reson. Imaging, vol. 42, no. 4, pp. 887–901, Oct. 2015.

[27] J. P. Marques, F. F. J. Simonis, and A. G. Webb, "Low-field MRI: An MR physics perspective," J. Magn. Reson. Imaging, vol. 49, no. 6, pp. 1528–1542, 2019.

[28] L. Feng, T. Benkert, K. T. Block, D. K. Sodickson, R. Otazo, and H. Chandarana, "Compressed sensing for body MRI," J. Magn. Reson. Imaging, vol. 45, no. 4, pp. 966–987, 2017.

[29] K. P. Pruessmann, M. Weiger, M. B. Scheidegger, and P. Boesiger, "SENSE: Sensitivity encoding for fast MRI," Magn. Reson. Med., vol. 42, no. 5, pp. 952–962, 1999.

[30] P. Virtue and M. Lustig, "On the empirical effect of Gaussian noise in under-sampled MRI reconstruction," arXiv, pp. 1–24, 2016.

[31] D. L. Donoho, A. Maleki, and A. Montanari, "The noise sensitivity phase transition in compressed sensing," Arxiv, vol. 57, no. 10, p. 40, 2010.

[32] E. Arias-Castro and Y. C. Eldar, "Noise folding in compressed sensing," IEEE Signal Process. Lett., vol. 18, no. 8, pp. 478–481, 2011.

[33] J. Zhu and D. Baron, "Performance regions in compressed sensing from noisy measurements," 2013 47th Annu. Conf. Inf. Sci. Syst. CISS 2013, pp. 2–6, 2013.

[34] M. Dahan, "Compressive Fluorescence Microscopy for Biological and Hyperspectral Imaging," Imaging Appl. Opt. Tech. Pap., vol. 109, no. 26, p. IM4C.5, 2012.

[35] Y. Wiaux, L. Jacques, G. Puy, A. M. M. Scaife, and P. Vandergheynst, "Compressed sensing imaging techniques for radio interferometry," Mon. Not. R. Astron. Soc., vol. 395, no. 3, pp. 1733–1742, 2009.

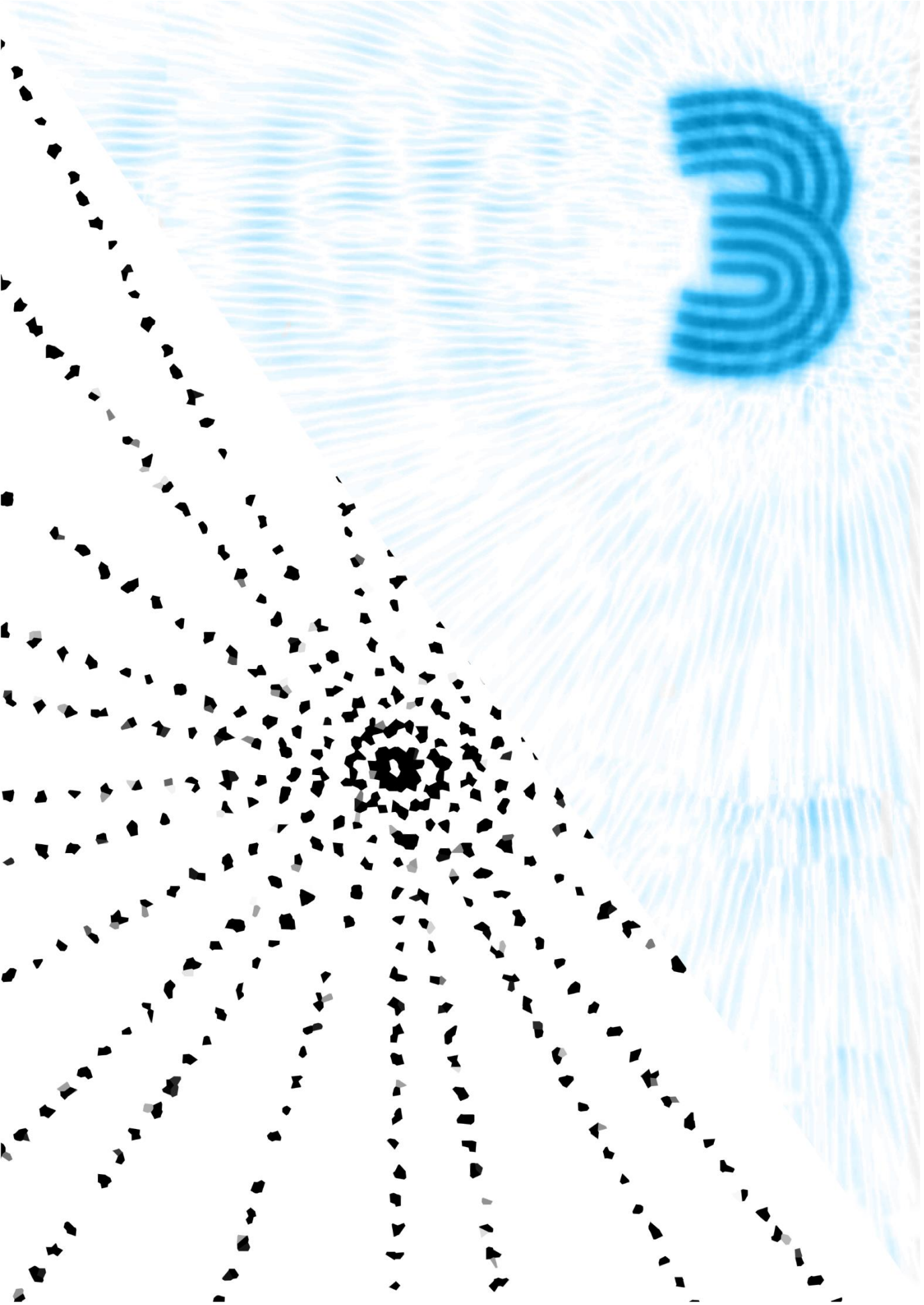

Chapter 3

Plaque permeability assessed with dynamic contrast-enhanced MRI predicts ferumoxytol nanoparticle uptake in patients with peripheral artery disease

Kang H. Zheng, MD*,
Jasper Schoormans*,
Lotte C.A. Stiekema,
Claudia Calcagno,
Iwona Cicha,
Christoph Alexiou,
Gustav J. Strijkers,
Aart J. Nederveen,
Erik S.G. Stroes,
Bram F. Coolen

Adapted from JACC: Cardiovascular Imaging, 2019; 12(10):2081-2083

3.1 Abstract

Objectives: This study investigated whether uptake of ultrasmall superparamagnetic iron oxide (USPIO; ferumoxytol) nanoparticles is related to atherosclerotic plaque permeability, assessed with dynamic contrast-enhanced (DCE-)MRI, in patients with peripheral artery disease (PAD).
Background: Nanomedicine holds promise for drug delivery of therapeutic agents to manage atherosclerosis. Because adequate delivery of nanoparticles to the plaque is a prerequisite to achieve a therapeutic response, non-invasive assessment of plaque permeability to nanoparticles is essential to identify patients suitable for nano therapy. Preclinical studies demonstrated that nanoparticle uptake in the atherosclerotic plaque is dependent on endothelial permeability.
Methods: Patients with PAD and healthy control subjects were recruited for USPIO-enhanced MRI and DCE-MRI of the femoral arteries. Quantitative R2* measurements before and 72 hours after USPIO administration were used to calculate regional ΔR2* values, representative of USPIO uptake. For femoral artery DCE-MRI, we implemented a novel 3D black-blood sequence with high spatiotemporal resolution. DCE images were acquired using Gadovist and AUC values were calculated from the signal intensity-time curves during the initial two minutes after contrast agent administration.
Results: 18 patients with PAD and 8 control subjects underwent all study procedures. Patients with PAD clearly demonstrated USPIO uptake with R2* changes in femoral plaques being markedly increased compared with the vessel wall of healthy controls (ΔR2* 19.9±12.5 s^{-1} vs. 5.67±4.38 s^{-1}; $p<0.001$). DCE-MRI revealed a wide range of contrast enhancement patterns, while showing co-localization with USPIO R2* maps. In plaques, there was a significant correlation between AUC and ΔR2* ($r=0.52$; $p=0.002$). In multivariable analysis the AUC remained a significant predictor of ΔR2* ($p=0.007$).
Conclusions: MRI-detected USPIO nanoparticle uptake in atherosclerotic plaques is associated with plaque permeability assessed with DCE-MRI, in patients with PAD. Further development of these imaging modalities may assist in a personalized approach to identify patients most suitable for nanomedical therapies.

3.2 Introduction

Since advances in drug development allow for very low levels of LDL-cholesterol to be achieved without any apparent safety concerns [1,2], the ensuing focus is shifting towards intervening in non-lipid pathways to reduce the residual cardiovascular (CV) risk [3]. Novel therapeutics including anti-inflammatory [4] and anti-coagulant [5] drugs have recently achieved risk reduction beyond contemporary drug regimens. However, an unacceptable high number of CV events still occur, underlining the need to further increase pharmacological efficacy. In contrast to LDL-cholesterol lowering strategies, dose-escalation of compounds targeting inflammatory or coagulant pathways cannot invariably be achieved, since higher efficacy is likely to be counterbalanced by increased systemic toxicity. In fact, this has already been illustrated by observations of an increased number of fatal infections for interleukin-1β antibody administration [4] and an increased bleeding risk for factor Xa-inhibition [5].

Encapsulating drugs in nanoparticles for atherosclerotic plaque targeted delivery could resolve this issue [6]. Nanomedicine has the potential to enhance drug delivery to target organs and thus increase efficacy, while minimizing systemic adverse effects due to a lower total dose administered [7]. We previously accomplished proof of concept in patients showing that administered nanoparticles reached the atherosclerotic plaque [8,9], but important questions remain to be answered before this approach can successfully be translated to a clinical setting [10]. One of the pivotal questions is how to non-invasively assess nanoparticle uptake efficiency in atherosclerotic lesions. Because sufficient delivery of drug-loaded nanoparticles to the atherosclerotic plaque is crucial for a therapeutic response and such therapy is likely to be costly, identifying patients who are likely to respond to nanomedical therapy prior to drug administration is important.

In the current study, we developed an MRI protocol to investigate whether nanoparticle delivery can be predicted non-invasively by assessment of plaque permeability. To this end, we used ultrasmall superparamagnetic iron-oxide (USPIO; ferumoxytol) nanoparticles, which are long circulating nanoparticles that are taken up by tissue macrophages [11]. By using quantitative R2* MRI measurements before and after USPIO administration, uptake of these nanoparticles in plaques can be assessed [12,13]. On the other hand, dynamic contrast-enhanced (DCE-)MRI using gadolinium (Gd)-based contrast agents measures uptake kinetics in the plaque and thus quantifies microvascular permeability [14]. We developed a novel 3D black-blood DCE-MRI technique with high spatiotemporal resolution and combined this with USPIO-enhanced imaging in patients with peripheral artery disease (PAD), in order to assess whether USPIO uptake in femoral plaques was related to plaque permeability as assessed by DCE-MRI.

3.3 Methods

Study design

This was a single-center, observational study performed in the Amsterdam UMC, location Academic Medical Center in Amsterdam. The study was conducted in accordance with the Declaration of Helsinki, the approval of the ethics committee of the Academic Medical Center and the written informed consent of all participants. All participants underwent blood withdrawal for lipid measurements and MRI scanning at baseline before ferumoxytol infusion and returned for repeat imaging after 72 hours.

Study populations

Patients with peripheral artery disease and healthy control subjects were included in this study. Patients were recruited based on the presence of atherosclerotic plaques in the femoral arteries as detected by duplex ultrasound. Exclusion criteria included contraindications for MRI scanning, history of anaphylaxis or severe allergic reactions, renal dysfunction (eGFR < 30 ml/min) or hepatic dysfunction (liver transaminases > 3 upper limit of normal) and femoral angioplasty. Healthy controls were age- and sex matched to patients.

USPIO administration

Ferumoxytol (AMAG Pharmaceuticals, Waltham, Massachusetts) at the dose of 4 mg/kg was diluted in 250 ml saline and administered intravenously over a period of 30 minutes. After infusion, participants were monitored for 30 minutes for adverse reactions.

MRI acquisitions

All imaging was performed on a 3 T MRI (Philips Ingenia, Best, the Netherlands) using a 16-channel phased-array anterior coil and a 16-channel phased-array posterior coil. After initial scout scans, a 3D improved motion-sensitized driven equilibrium (iMSDE) black-blood gradient echo sequence covering both femoral arteries was performed using the following parameters: TR = 10 ms, TE = 3.4 ms, FA = 8°, ETL = 60, FOV = 320 x 320 x 50 mm^3, resolution = 0.7 x 0.7 x 0.7 mm^3, NSA = 3. This acquisition was used to localize atherosclerotic plaques, non-plaque containing regions of patients (patient non-plaque vessel wall) and a standardized region of the femoral artery of healthy controls located approximately 10 mm cranial from the flow divider (healthy control vessel wall).

USPIO-enhanced MRI – USPIO accumulation was detected using a 2D Double Inversion Recovery (DIR) T2*-weighted multi-echo gradient echo sequence. Single slices of plaques (at point of maximum stenosis, carefully avoiding slices with overt calcification because of insufficient MRI signal), as well as patient non-plaque vessel wall and healthy control vessel wall were acquired with the following parameters: TR = 41.15 ms, TE = 3.28 ms, FA = 90°, ETL = 8, FOV = 280 x 280 mm^2, resolution = 0.58 x 0.58 mm^2, slice thickness = 2 mm, NSA = 2. Repeat imaging at 72 hours was meticulously performed using anatomical landmarks to ensure accurate co-localization with baseline images. The multi-echo data was used for quantitative mapping analysis to derive pixel-wise T2* and R2* (=1/T2*) values.
DCE-MRI acquisition – Additionally, a 3D DCE-MRI scan was performed during the baseline visit. Participants were scanned continuously for 10 minutes. Four minutes after the start of the scan, a Gd-based contrast agent (Gadovist, Bayer, Leverkusen, Germany) at the dose of 0.1 mmol/kg bodyweight was injected intravenously. For acquisition, we used a 3D T1-weighted FFE scan with a tiny golden angle radial stack-of-stars sampling scheme and iMSDE pre-pulses for blood suppression [15]. Every TFE-shot acquired one z-stack of radial spokes, while a low-high sampling order in the k_z-direction assured good blood suppression. Additionally, fat signal was suppressed by a spectral presaturation with inversion recovery (SPIR) fat-saturation pre-pulse. Further scan parameters were: TR = 7.2 ms, TE = 3.2 ms, FA=15°, TFE-factor = 36, FOV = 250 x 250 x 60 mm^3, resolution = 0.7 x 0.7 x 2 mm^3. The radial stack-of-stars acquired data was reconstructed with a compressed sensing reconstruction using a temporal variation constraint, which resulted in a temporal resolution of 11.8 seconds per volume.

Image analysis

Vessel wall dimensions of the common femoral arteries were analyzed using the 3D black-blood MRI scans in a standardized segment of 20.3 mm long, starting from 10.5 mm away from the flow divider of the bifurcation, similar to previously described methods.[16] To calculate mean wall area and mean wall thickness, lumen and outer wall contours were manually delineated using VesselMass (Leiden University, Leiden, the Netherlands). T2*-weighted multi-echo images for each participant were analyzed using Medis Medical Imaging Systems (Leiden, the Netherlands). Regions of interest (ROI) were drawn by delineating lumen and outer wall contours on the generated quantitative T2* maps. To quantify USPIO uptake, we calculated the absolute change in R2* between baseline and post USPIO infusion scans for the arterial wall. For atherosclerotic plaques, we divided the ROI in 6 segments and calculated the mean R2* for all plaque-containing segments, defined as having a mean wall thickness greater than 1.5 mm. For patient non-plaque vessel wall and healthy control vessel wall, R2* was calculated for the entire vessel wall ROI. DCE-MRI images were co-localized to the slices of the T2*-weighted multi-echo images

and ROIs were drawn in the same manner. Signal-intensity time curves of the ROI were generated, in which the signal was normalized by removing and dividing by the pre-injection baseline signal. The relative area-under-the-curve (AUC) was calculated for all analyzed tissues by summing the normalized signal intensity for the two minutes following injection.

Statistical analysis

All data are presented as mean with standard deviation or median with interquartile ranges. To assess differences in vessel wall dimensions, a Student T-test was performed. For evaluation of USPIO uptake between groups, a one-way analysis of variance was performed. If significance was found, post-hoc testing was performed using Tukey's range test. Correlation between USPIO uptake and DCE-MRI contrast enhancement was tested using Pearson's correlation coefficients. Statistical analyses were performed using the SPSS Statistics package version 24 (IBM, Armonk, New York).

3.4 Results

18 PAD patients (mean age 55.8 ± 10.1 years; 13 males) and 8 age- and sex-matched healthy controls provided written informed consent and were subjected to all study procedures. As expected, PAD patients were characterized by the preponderance of cardiovascular risk factors, as well as receiving standard of care medication for secondary prevention of cardiovascular disease. Clinical characteristics are listed in Table 1. No adverse events or reactions occurred upon USPIO administration, which was well tolerated by all participants.

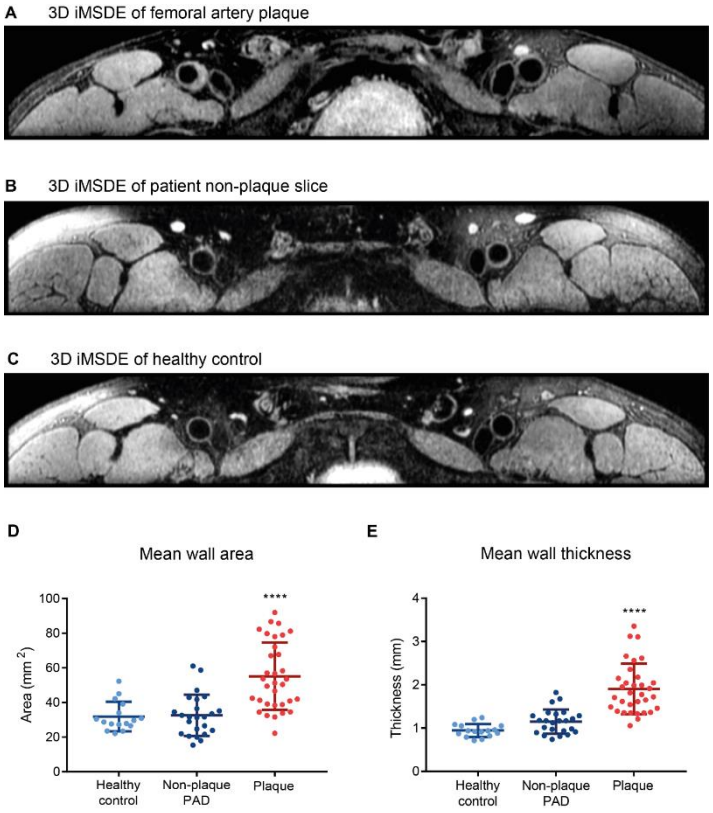

Figure 1. Vessel wall dimensions are increased in PAD patients.
3D black-blood MRI scans were performed to identify (A) femoral artery plaques and (B) non-plaque vessel wall in patients with PAD, as well as (C) vessel wall in healthy control subjects. Analysis of vessel wall dimensions demonstrated that (D) mean wall area and (E) mean wall thickness was increased for plaques compared with patient non-plaque vessel wall and healthy control femoral artery wall.

Vessel wall dimensions are increased in PAD patients

Arterial wall dimensions in a standardized segment of each femoral artery were determined using 3D black-blood MRI. In total, 35 femoral arteries of PAD patients and 15 femoral arteries of healthy controls were suitable for analysis. One patient had a total occlusion of the common femoral artery on one side and 1 healthy control had an anatomical variant of the femoral artery precluding vessel wall dimension analysis. PAD patients had thickened femoral arteries compared with healthy controls, as evidenced by a mean wall area of 47 ± 17 mm^2 vs. 32 ± 8 mm^2 ($p=0.003$) and a mean wall thickness of 1.70 ± 0.59 mm vs. 0.95 ± 0.11 mm ($p<0.001$).
Using the 3D black-blood scans, we identified 34 plaques and 24 non-plaque vessel wall slices in patients with PAD and 16 control vessel wall slices in healthy control

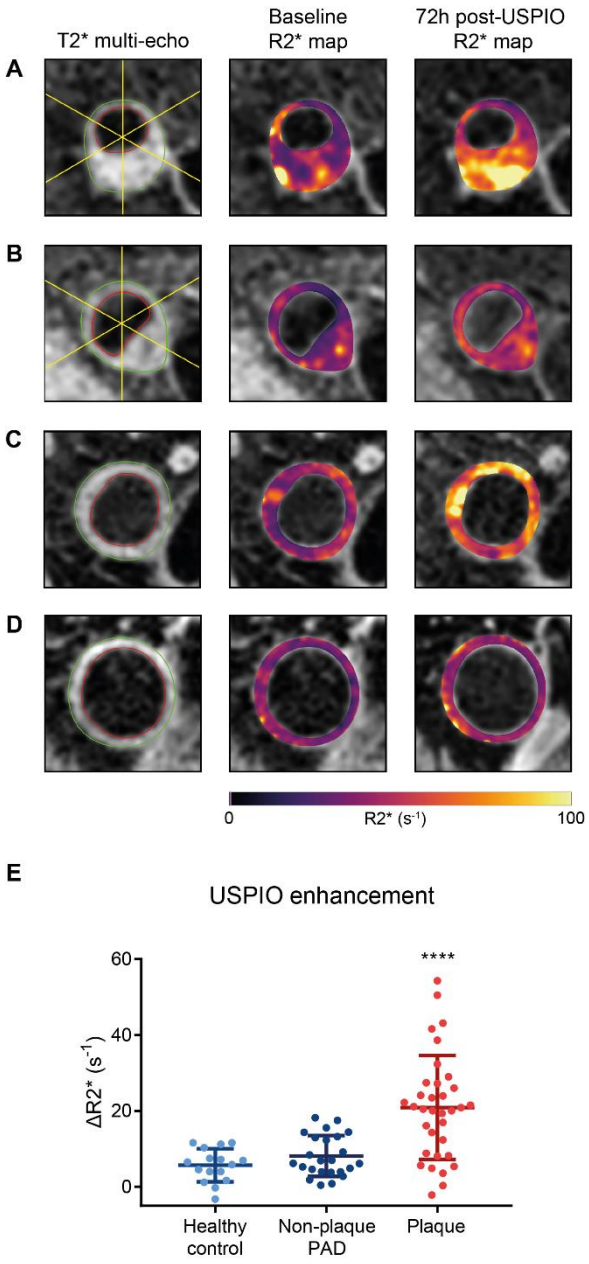

Figure 2. USPIO uptake is enhanced in PAD patients. USPIO-enhanced MRI scans were performed using T2* multi-echo sequences (TE=3.2 ms presented as anatomical reference, left) and color-coded R2* maps were generated to illustrate quantification of USPIO uptake, before (middle) and 72 hours (right) after administration of USPIO nanoparticles. For femoral artery plaques, the ROI was divided in 6 segments and the mean R2* of all plaque-containing segments (defined as having a mean wall thickness greater than 1.5 mm) was calculated (A+B, left). We detected varying degrees of USPIO uptake as measured by an increase in R2*, as depicted by examples of high (A) and low (B) uptake in femoral artery plaques. (C) In patients with PAD, USPIO uptake was occasionally also observed in non-plaque vessel wall. (D) Healthy control vessel walls were characterized by low uptake of USPIO. (E) R2* changes 72 hours after administration of USPIO nanoparticles.

subjects for USPIO-enhanced MRI and DCE-MRI (Figure 1A- C). Vessel wall dimensions of plaques were markedly increased compared with the patient non-plaque and healthy control vessel wall: mean wall area was 55.2 ± 19.5 mm^2 vs. 32.6 ± 11.9 mm^2 vs. 31.9 ± 8.5 mm^2, respectively ($p<0.001$ for comparisons vs. plaque), and mean wall thickness was 1.90 ± 0.58 mm vs. 1.15 ± 0.28 mm vs. 0.94 ± 0.15 mm, respectively ($p<0.001$ for comparisons vs. plaque) (Figure 1D+E).

USPIO uptake is enhanced in femoral plaques

Next, we performed quantitative USPIO MRI for the identified plaques, patient non-plaque vessel wall and healthy control vessel wall. At baseline, R2* values of plaques were not different compared with non-plaque vessel wall in patients with PAD (44.3 ± 10.1 s^{-1} vs. 40.4 ± 5.8 s^{-1}, p=0.153), but were slightly increased compared with the vessel wall of controls (35.5 ± 4.3 s^{-1}, p=0.001). Repeat imaging 72 hours after USPIO administration revealed USPIO enhancement of the vessel wall especially in PAD patients, detected by clear regional increases in the R2* maps (Figure 2A). Importantly, a wide spectrum of USPIO uptake patterns could be detected (Figure 2B and 2C). Furthermore, the change in R2* in plaques (ΔR2* = 19.9±12.5 s^{-1}) was markedly increased compared with patient non-plaque vessel wall (ΔR2* = 8.1±5.4 s^{-1}; p<0.001) and healthy control vessel wall (ΔR2* = 5.67 ± 4.38 s^{1}; p<0.001). USPIO enhancement between patient non-plaque vessel wall and healthy control vessel wall was not different (p=0.694).

Table 1. Baseline characteristics of participants

	PAD patients	Healthy controls
N	18	8
Clinical parameters		
Age, years	55.8 ± 10.1	56.3 ± 7.2
Male sex	13 (72.2%)	6 (75%)
Body mass index, kg/m2	26.5 ± 4.6	25.5 ± 2.7
Ischemic heart disease	3 (16.7)	0 (0)
Stroke/TIA	2 (11.1)	0 (0)
Active smoker	8 (44.4)	1 (12.5)
Diabetes	5 (27.8)	0 (0)
Hypertension	15 (83.3)	0 (0)
Laboratory data		
Total cholesterol, mg/dL	174 ± 83	213 ± 52
LDL cholesterol, mg/dL	97 ± 78	120 ± 35
HDL cholesterol, mg/dL	47 ± 14	66 ± 25
Triglycerides, mg/dL	151 (94-248)	127 (43-234)
Lipoprotein (a), mg/dL	11.3 (5.9-37.2)	8.6 (5.7-44.5)
Medication		
Lipid lowering therapy	18 (100)	0 (0)
Anti-hypertensive	15 (83.3)	0 (0)
Anti-platelet	17 (94.4)	0 (0)
Anti-diabetic	5 (27.8)	0 (0)
Femoral artery dimensions		
Mean wall area, mm2	47 ± 17	32 ± 8
Mean wall thickness, mm	1.70 ± 0.59	0.95 ± 0.11

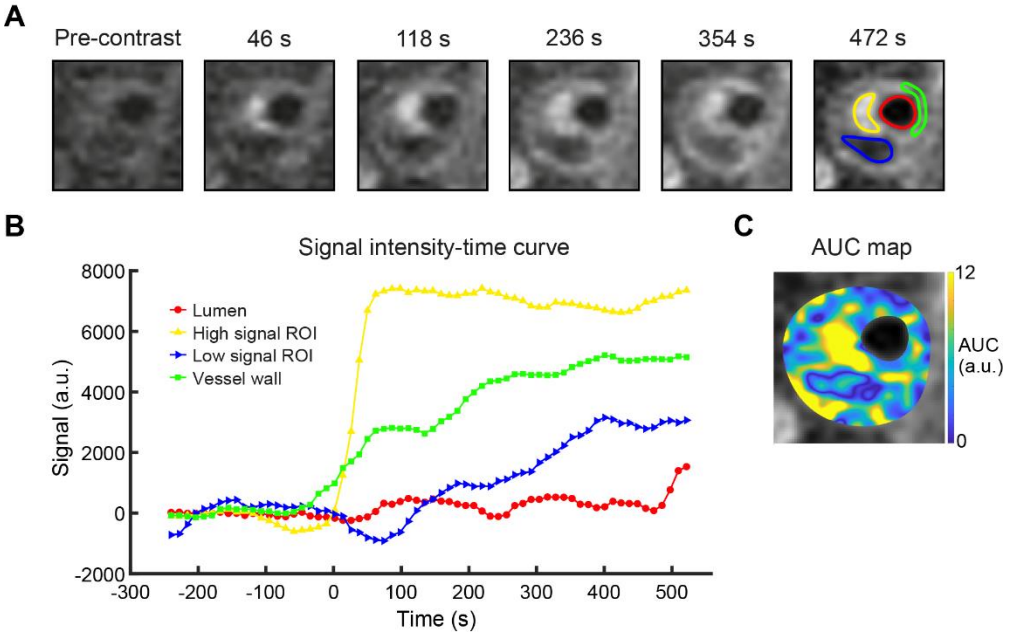

Figure 3. DCE-MRI reveals heterogeneous enhancement patterns in PAD patients. (A) Dynamic contrast-enhanced scans of femoral artery plaque demonstrating heterogeneous enhancement after injection of Gadovist, illustrated by the observed differences between the colored ROIs and (B) corresponding signal intensity-time curves (normalized for baseline signal intensity). (C) Area-under-the-curve maps covering the first two minutes after injection were generated to allow for further analysis of plaques.

DCE-MRI predicts USPIO uptake in femoral plaques

At the baseline visit, all study subjects were subjected to a DCE-MRI to assess vessel wall permeability. DCE-MRI slices were co-registered to plaques previously identified for USPIO imaging (33 out of 34 plaques; one DCE-MRI image was of insufficient quality). Figure 3A shows an example of a DCE-MRI time series with corresponding signal-intensity time curves in different plaque regions (Figure 3B), as well as the quantitative pixel-wise AUC map calculated from the first two minutes following Gadovist injection (Figure 3C).

In patients with PAD, these AUC maps showed co-localization with USPIO uptake as indicated by the R2* maps of the corresponding plaques (Figure 4A-C). For plaques there was a significant correlation between the AUC and ΔR2* (r=0.52; p=0.002) (Figure 4D). In multivariable analysis, adjusting for age, sex, BMI, smoking, diabetes, hypertension, LDL-cholesterol and Lp(a), the AUC remained a significant predictor of ΔR2* (ß 3.24 (1.00-5.49), p=0.007). In a secondary analysis, we assessed the AUC values for patient non-plaque vessel wall and healthy control vessel wall. There were no correlations with the co-registered patient non-plaque and healthy control vessel wall ΔR2* values.

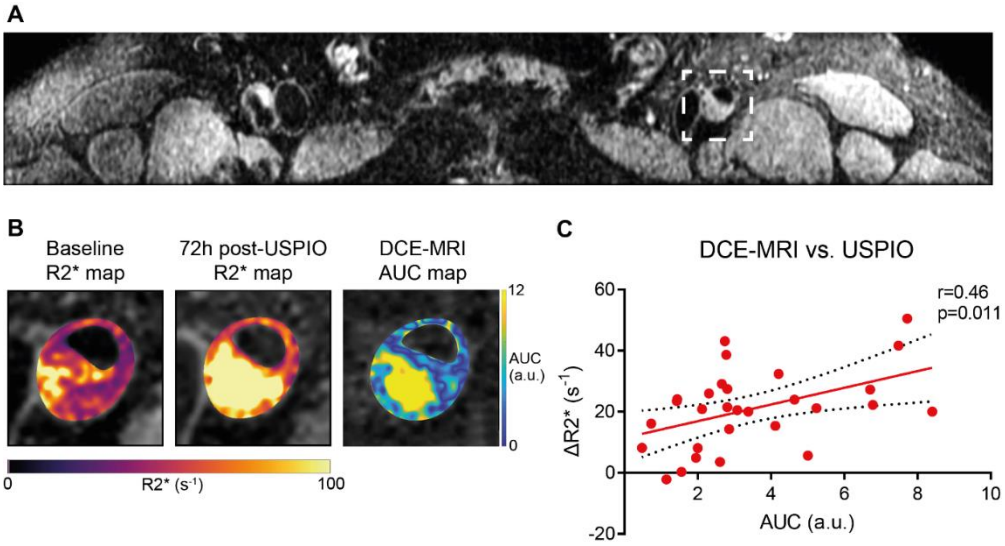

Figure 4. DCE-MRI associates with USPIO enhancement. (A) Example of femoral artery plaque identified with 3D iMSDE sequence which demonstrated (B) strong USPIO uptake which co-localized with DCE-MRI enhancement. (C) DCE-MRI and USPIO-enhanced MRI of plaques were significantly correlated in patients with PAD.

3.5 Discussion

We report for the first time the assessment of USPIO nanoparticle uptake in femoral artery plaques in patients with PAD using quantitative USPIO-enhanced MRI, which was found to be associated with plaque permeability as measured with DCE-MRI. These MRI techniques provide important phenotypic information on atherosclerotic plaques and hold potential for future decision algorithms to allocate nanomedical treatment using a personalized approach.

In this proof-of-concept study, we used ferumoxytol as nanoparticle agent, which could be detected using MRI. Previous studies have established that ferumoxytol and other USPIOs are engulfed by macrophages in human atherosclerotic plaques and other inflamed cardiovascular tissues [17-23]. We quantified USPIO enhancement using R2* mapping, allowing us to detect heterogeneous USPIO enhancement among and within femoral artery plaques. These observations may relate to local variations in inflammatory cell content and/or other features which affect nanoparticle penetration in the plaque.

Clinical imaging studies investigating atherosclerotic plaque vulnerability have used DCE-MRI to study plaque microvasculature, recognizing that plaque inflammation, neovascularization and impaired endothelial barrier function are closely related processes [24-27]. Ideally, vascular DCE-MRI requires high spatial resolution and optimal blood suppression to accurately delineate the vessel wall; as well as high temporal resolution to capture the signal dynamics. To this end, we developed a novel 3D black-blood DCE-MRI protocol with sufficient anatomical coverage to enable characterization of contrast enhancement patterns in femoral atherosclerotic plaques. Plaque permeability, semi-quantitatively assessed with the AUC of the signal enhancement curves, was positively and independently correlated to the level of USPIO enhancement. The correlation between plaque permeability assessed with DCE-MRI and USPIO nanoparticle accumulation in patients substantiates findings from preclinical studies, linking nanoparticle deposition to endothelial barrier function [28,29].

Our data also herald potential clinical utility. First, DCE-MRI holds promise to predict nanoparticle delivery in plaques in humans, allowing for tailored decisions in patients with advanced atherosclerotic disease. Despite the promise of nanomedicine to specifically target atherosclerotic plaques using nanoparticle encapsulated drugs, most research remains in the preclinical setting [30]. The use of non-invasive imaging methods such as DCE-MRI to assess plaque susceptibility to nanoparticle uptake may help to accelerate development of nanomedicine-based strategies. Second, DCE-MRI also provides information on the degree of arterial wall inflammation. In support, the majority of clinical studies in carotid atherosclerosis have reported a positive association between 18F-FDG-PET/CT and DCE-MRI measurements [31-33]. Thus, DCE-MRI also holds potential in assisting personalized management of high-risk patients in the context of novel anti-inflammatory drugs

[4], or to serve as surrogate endpoint in drug development trials. Note that theoretically also USPIOs can be used for aforementioned purposes. However, it should be taken into account that this is a burdensome procedure for patients, as it requires two imaging sessions 72 hours apart. In addition, the availability of USPIOs has been restricted in Europe, following the observed risk of severe allergic reactions upon ferumoxytol administration in post-marketing safety data. Awaiting the development of safer USPIOs [34], these challenges confine implementation of USPIO-enhanced MRI in clinical practice.

Limitations of this study include the absence of tissue samples, although previous studies provided human histological validation of USPIO uptake by plaque macrophages [17-21] and of the correlation between DCE-MRI and plaque microvessel density [24-27,32]. In this proof-of-concept study, we used ferumoxytol as a model for nanoparticle delivery. However, prospective studies are needed to establish whether plaque permeability as assessed by DCE-MRI is also related to plaque uptake of other nanomedicinal formulations. Finally, we found that the AUC values from patient non-plaque and healthy controls did not correlate with the ΔR2* values. This may be due to the partial volume effect, inherent to a thin vessel wall, decreasing the accuracy of DCE-MRI measurements in patient non-plaque vessel wall and healthy controls. Increasing spatial resolution will be required to investigate whether DCE-MRI measurements in the diseased vessel wall, but before the presence of an overt plaque, are useful.

In conclusion, we demonstrate that USPIO nanoparticle uptake in atherosclerotic plaques is associated with plaque permeability as assessed with DCE-MRI in patients with PAD. We envision that further development of these imaging modalities may assist in evaluation of novel therapeutics and personalized decisions in high-risk CV patients.

3.6 References

[1] Giugliano RP, Pedersen TR, Park JG et al. Clinical efficacy and safety of achieving very low LDL-cholesterol concentrations with the PCSK9 inhibitor evolocumab: a prespecified secondary analysis of the FOURIER trial. Lancet 2017;390:1962-1971.

[2] Schwartz GG, Steg PG, Szarek M et al. Alirocumab and Cardiovascular Outcomes after Acute Coronary Syndrome. N Engl J Med 2018.

[3] Bohula EA, Giugliano RP, Leiter LA et al. Inflammatory and Cholesterol Risk in the FOURIER Trial. Circulation 2018;138:131-140.

[4] Ridker PM, Everett BM, Thuren T et al. Antiinflammatory Therapy with Canakinumab for Atherosclerotic Disease. N Engl J Med 2017;377:1119-1131.

[5] Eikelboom JW, Connolly SJ, Bosch J et al. Rivaroxaban with or without Aspirin in Stable Cardiovascular Disease. N Engl J Med 2017;377:1319-1330.

[6] Lobatto ME, Fuster V, Fayad ZA, Mulder WJ. Perspectives and opportunities for nanomedicine in the management of atherosclerosis. Nat Rev Drug Discov 2011;10:835-52.

[7] Mulder WJ, Jaffer FA, Fayad ZA, Nahrendorf M. Imaging and nanomedicine in inflammatory atherosclerosis. Sci Transl Med 2014;6:239sr1.

[8] van der Valk FM, van Wijk DF, Lobatto ME et al. Prednisolone-containing liposomes accumulate in human atherosclerotic macrophages upon intravenous administration. Nanomedicine 2015;11:1039-46.

[9] Zheng KH, van der Valk FM, Smits LP et al. HDL mimetic CER-001 targets atherosclerotic plaques in patients. Atherosclerosis 2016;251:381-388.

[10] Cicha I, Chauvierre C, Texier I et al. From design to the clinic: practical guidelines for translating cardiovascular nanomedicine. Cardiovasc Res 2018;114:1714-1727.

[11] Sadat U, Usman A, Gillard JH. Imaging pathobiology of carotid atherosclerosis with ultrasmall superparamagnetic particles of iron oxide: an update. Curr Opin Cardiol 2017;32:437-440.

[12] Patterson AJ, Tang TY, Graves MJ, Muller KH, Gillard JH. In vivo carotid plaque MRI using quantitative T2* measurements with ultrasmall superparamagnetic iron oxide particles: a dose-response study to statin therapy. NMR Biomed 2011;24:89-95.

[13] Smits LP, Tiessens F, Zheng KH, Stroes ES, Nederveen AJ, Coolen BF. Evaluation of ultrasmall superparamagnetic iron-oxide (USPIO) enhanced MRI with ferumoxytol to quantify arterial wall inflammation. Atherosclerosis 2017;263:211-218.

[14] van Hoof RH, Heeneman S, Wildberger JE, Kooi ME. Dynamic Contrast-Enhanced MRI to Study Atherosclerotic Plaque Microvasculature. Curr Atheroscler Rep 2016;18:33.

[15] Schoormans J, Zheng KH, Stroes ES, Strijkers G, Nederveen AJ, Coolen BF. 3D black-blood DCE-MRI using radial stack-of-stars acquisition and CS reconstruction: application in carotid and femoral arteries. Proceedings of the 25th Annual Meeting of the ISMRM, Honolulu, 2017.

[16] Duivenvoorden R, de Groot E, Elsen BM et al. In vivo quantification of carotid artery wall dimensions: 3.0-Tesla MRI versus B-mode ultrasound imaging. Circ Cardiovasc Imaging 2009;2:235-42.

[17] Kooi ME, Cappendijk VC, Cleutjens KB et al. Accumulation of ultrasmall superparamagnetic particles of iron oxide in human atherosclerotic plaques can be detected by in vivo magnetic resonance imaging. Circulation 2003;107:2453-8.

[18] Trivedi RA, JM UK-I, Graves MJ et al. In vivo detection of macrophages in human carotid atheroma: temporal dependence of ultrasmall superparamagnetic particles of iron oxide-enhanced MRI. Stroke 2004;35:1631-5.

[19] Trivedi RA, Mallawarachi C, JM UK-I et al. Identifying inflamed carotid plaques using in vivo USPIO-enhanced MR imaging to label plaque macrophages. Arterioscler Thromb Vasc Biol 2006;26:1601-6.

[20] Howarth SP, Tang TY, Trivedi R et al. Utility of USPIO-enhanced MR imaging to identify inflammation and the fibrous cap: a comparison of symptomatic and asymptomatic individuals. Eur J Radiol 2009;70:555-60.

[21] Metz S, Beer AJ, Settles M et al. Characterization of carotid artery plaques with USPIO-enhanced MRI: assessment of inflammation and vascularity as in vivo imaging biomarkers for plaque vulnerability. Int J Cardiovasc Imaging 2011;27:901-12.

[22] Richards JM, Semple SI, MacGillivray TJ et al. Abdominal aortic aneurysm growth predicted by uptake of ultrasmall superparamagnetic particles of iron oxide: a pilot study. Circ Cardiovasc Imaging 2011;4:274-81.

[23] Stirrat CG, Alam SR, MacGillivray TJ et al. Ferumoxytol-enhanced magnetic resonance imaging assessing inflammation after myocardial infarction. Heart 2017;103:1528-1535.

[24] Kerwin W, Hooker A, Spilker M et al. Quantitative magnetic resonance imaging analysis of neovasculature volume in carotid atherosclerotic plaque. Circulation 2003;107:851-6.

[25] Kerwin WS, O'Brien KD, Ferguson MS, Polissar N, Hatsukami TS, Yuan C. Inflammation in carotid atherosclerotic plaque: a dynamic contrast-enhanced MR imaging study. Radiology 2006;241:459-68.

[26] Kerwin WS, Oikawa M, Yuan C, Jarvik GP, Hatsukami TS. MR imaging of adventitial vasa vasorum in carotid atherosclerosis. Magn Reson Med 2008;59:507-14.

[27] van Hoof RHM, Voo SA, Sluimer JC et al. Vessel wall and adventitial DCE-MRI parameters demonstrate similar correlations with carotid plaque microvasculature on histology. J Magn Reson Imaging 2017;46:1053-1059.

[28] Kim Y, Lobatto ME, Kawahara T et al. Probing nanoparticle translocation across the permeable endothelium in experimental atherosclerosis. Proc Natl Acad Sci U S A 2014;111:1078-83.

[29] Stein-Merlob AF, Hara T, McCarthy JR et al. Atheroma Susceptible to Thrombosis Exhibit Impaired Endothelial Permeability In Vivo as Assessed by Nanoparticle-Based Fluorescence Molecular Imaging. Circ Cardiovasc Imaging 2017;10.

[30] Chan CKW, Zhang L, Cheng CK et al. Recent Advances in Managing Atherosclerosis via Nanomedicine. Small 2018;14.

[31] Calcagno C, Ramachandran S, Izquierdo-Garcia D et al. The complementary roles of dynamic contrast-enhanced MRI and 18F-fluorodeoxyglucose PET/CT for imaging of carotid atherosclerosis. Eur J Nucl Med Mol Imaging 2013;40:1884-93.

[32] Taqueti VR, Di Carli MF, Jerosch-Herold M et al. Increased microvascularization and vessel permeability associate with active inflammation in human atheromata. Circ Cardiovasc Imaging 2014;7:920-9.

[33] Truijman MT, Kwee RM, van Hoof RH et al. Combined 18F-FDG PET-CT and DCE-MRI to assess inflammation and microvascularization in atherosclerotic plaques. Stroke 2013;44:3568-70.

[34] Unterweger H, Dezsi L, Matuszak J et al. Dextran-coated superparamagnetic iron oxide nanoparticles for magnetic resonance imaging: evaluation of size-dependent imaging properties, storage stability and safety. Int J Nanomedicine 2018;13:1899-1915.

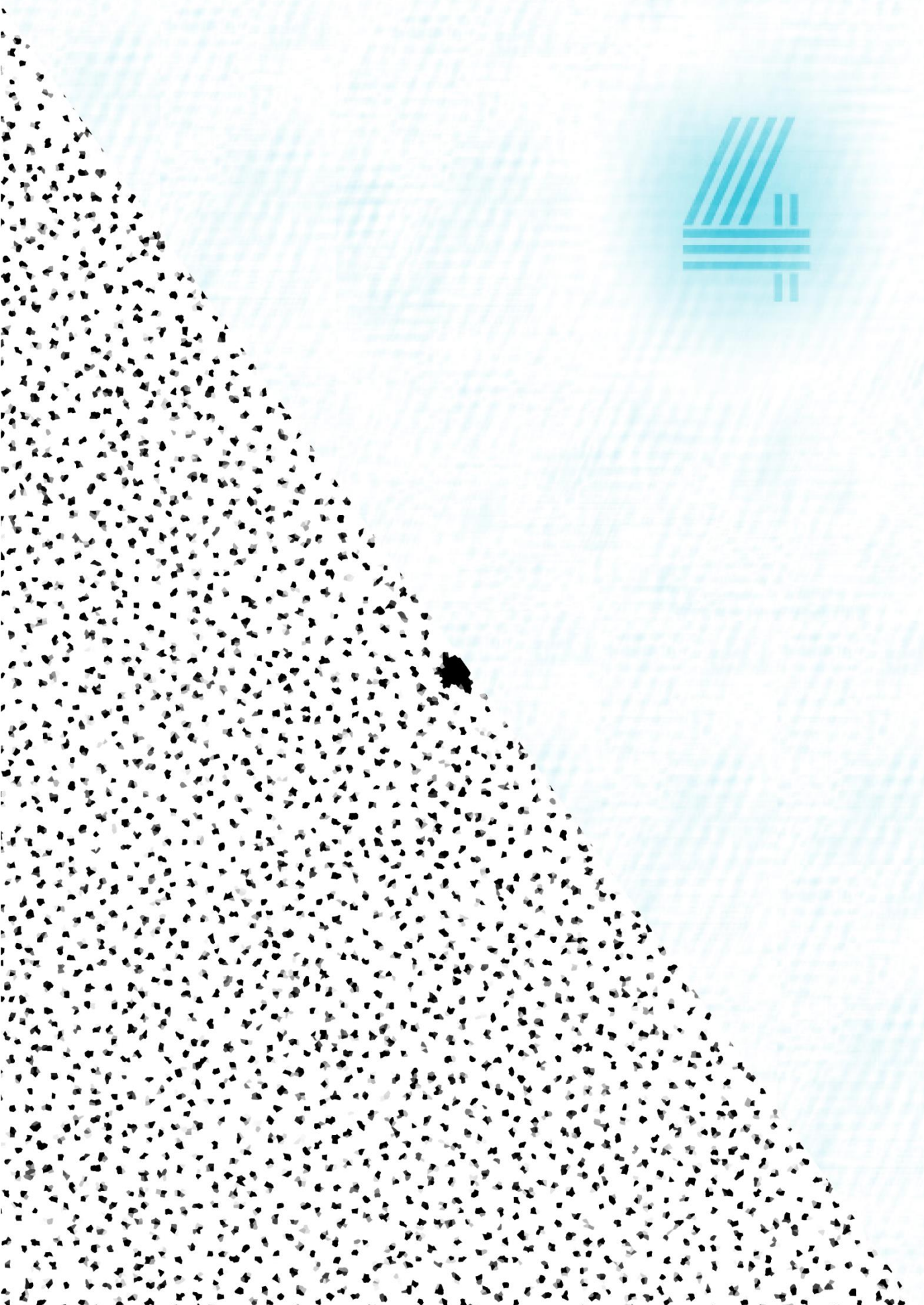

Chapter 4

Pharmacokinetic modeling of 3D black-blood vessel wall DCE imaging using an AIF independent reference region method.

4.1 Abstract

Purpose: Changes in pharmacokinetic (PK) parameters have been associated with plaque vulnerability. To enable clinical implementation, fast volumetric dynamic contrast-enhanced (DCE) sequences have been developed. Vessel wall delineation necessitates blood suppression; however, this prohibits Arterial Input Function (AIF)-based PK parameter estimation. We aim to evaluate reference-region PK analysis for vessel wall DCE applications.

Methods: A compressed sensing-accelerated black-blood DCE protocol was used. Monte Carlo simulation of the signal evaluation and analysis were used to estimate the feasibility of the method. Patient scans of peripheral artery disease patients (PAD, n=18) and abdominal aortic aneurysm (AAA) patients (n=7) were evaluated.

Conclusions: In all cases, the blood signal was sufficiently suppressed throughout the scan. We were able to model PK parameters without an AIF, using the constrained extended reference region with additional constraints. Reproducibility in a patient population with AAAs was moderate. The presented method yielded good discrimination between vessel wall and plaque tissue types both in Monte Carlo simulations and in vivo patient data.

4.2 Introduction

Atherosclerotic plaque microvascularization and increased vessel wall permeability are characteristic features of vulnerable plaques, which are associated with cardiovascular events, such as myocardial infarction and stroke. Dynamic contrast-enhanced (DCE) vessel wall magnetic resonance imaging (MRI) using fast T1-weighted gradient-echo sequences allows assessment of these parameters in a quantitative way by applying pharmacokinetic (PK) modeling to the measured signal curves providing parameters such as K^{trans} and v_p [1], [2]. Changes in PK parameters have been associated with increased plaque vulnerability. Moreover, these imaging biomarkers are increasingly used as secondary endpoints in the evaluation of novel therapeutic strategies [3].

Recently, innovations in accelerated imaging have allowed the development of 3D DCE protocols with high isotropic resolution [4]–[6]. These protocols are highly beneficial because they provide large coverage of the arterial segment of interest. Moreover, the imaging volume can be oriented (and reconstructed) independent of the vessel orientation even when multiple arteries are involved, e.g. both carotids or femoral arteries. 3D protocols are usually performed with non-selective blood suppression to prevent severe flow artefacts and achieve good delineation of the vessel wall. However, this suppression highly compromises simultaneous measurement of the blood arterial input function (AIF), information which is generally required to perform pharmacokinetic modeling of the DCE data.

Several strategies could be employed to overcome the AIF issue. First, a low concentration pre-bolus could be given and measured with a fast bright-blood sequence. Timing and scaling of the low-bolus AIF to the full-bolus DCE data increases complexity of both the examination and the postprocessing, and might introduce errors [7]. Secondly, a population-based AIF can be simply assumed. However, this could introduce bias in PK parameters, especially in a patient population with cardiac output differences. Third, DCE protocols with interleaved bright-blood and black-blood acquisitions have been developed to acquire both AIF and vessel response curves. While most of these interleaved methods are two-dimensional [8], the recently developed LABBI sequence [5] uses a compressed sensing accelerated volumetric black-blood sequence interleaved with a 2D bright-blood AIF measurement. Still, this approach may suffer from several disadvantages since the interruption of the steady-state condition requires complex models to relate the signal to the contrast agent (CA) concentration. Furthermore, scan efficiency is compromised, while fast sampling is paramount for good accuracy of tissue perfusion parameter estimations [9]. To achieve the required fast AIF sampling without sacrificing spatial resolution, dual imaging approaches have been

proposed [10], [11]. Finally, a semi-quantitative analysis could be performed, such as determination of the area-under-the-curve (AUC). While AUC has been shown to correlate to plaque micro vessel count [12], and positively correlated with K^{trans} [13], it remains difficult to relate semi-quantitative parameters to relevant tissue properties, such as plaque permeability and blood volume.

For tumor imaging, Yankeelov et al. [14] have shown that reliable pharmacokinetic parameters can be made without the use of an AIF, by means of analyzing data from a reference tissue within the same dynamic scan. Often, muscle is taken as the reference tissue, meaning that resulting PK parameters are relative to those of muscle. An additional benefit is that reference methods seem to be more robust for lower temporal resolutions [15], making this approach feasible for 3D applications. The original Reference Region Method (RRM) is derived from the Tofts model [16] and therefore does not take into account the vascular contribution (v_p) in the solution of the two-compartment model. While v_p is usually very low in tumors, it is a significant parameter in vessel wall imaging. For vessel wall DCE applications, the extended Tofts model was found to have superior performance [17]. In contrast to the RRM, the recently published Constrained Extended RRM (CERRM) does incorporate v_p [18] and could therefore be used to perform AIF-independent pharmacokinetic modeling of vessel wall DCE data. However, to our knowledge, this has not been studied so far in literature.

Recently, we developed an accelerated volumetric black-blood DCE sequence, which can be applied to different vascular beds [19]. The DCE sequence uses a stack-of-stars golden angle radial sampling strategy with center-out ordering to achieve high-spatial and high-temporal resolutions, while maintain blood suppression. In this study, we combined this approach with CERRM modelling to obtain AIF independent vessel wall PK parameters. Firstly, we added additional constraints to the CERRM model to improve fitting reliability and investigate through simulations how the performance of the CERRM model compares to other published models in terms of sensitivity to changes in PK parameters. Furthermore, we demonstrate the feasibility our approach by analyzing data from repeated DCE measurements in patients with abdominal aorta aneurysms (AAA), as well as data from patients suffering from peripheral artery atherosclerotic plaques (Peripheral Artery Disease; PAD).

4.3 Methods

DCE acquisition and reconstruction We implemented a radial stack-of-stars sampling scheme [6] with an improved motion-sensitized driven-equilibrium (iMSDE) pre-pulse [20]. The tiny golden angle scheme of angle increments was used to minimize eddy current effects, while maintaining a near-uniform k-space coverage after sorting the data in time-frames [21]. The blood signal was suppressed continuously throughout the scan by the iMSDE pre-pulse at the beginning of each TFE shot. Also, a CHESS fat-suppression pre-pulse was given at the beginning of each shot. The TFE-shot length was chosen such that it could acquire either one stack or half a stack of radial spokes. A low-high sampling order in the k_z-direction assured good blood suppression. A diagram of the sequence is shown in Figure 1. A compressed sensing reconstruction was performed with a total-variation constraint in the temporal dimension [22]. Slices were reconstructed in parallel, after inverse FFT of the k-space in the fully sampled k_z-direction. Coils were compressed to six virtual channels [23]. Sensitivity maps were estimated from the center of k-space acquired before contrast injection using the adaptive method [24]. The radial spokes were sorted in time-frames. For every slice, the following equation was minimized:

$$\hat{x} = argmin\ |NS^{-1}X - Y|_2^2 + \lambda|TV(X)|_1, \quad (1)$$

Where X is the multi-dimensional image, TV is the finite difference operator in the temporal dimension; Y is the multi-channel, multi-frame k-space; N is the NUFFT operator, and S is the coil sensitivity operator. The sparsity parameter λ was chosen to prevent smoothing of the initial contrast-arrival peak. The computationally expensive NUFFT operator was accelerated [25] and reconstructions were performed on a computer cluster containing two Tesla P100 GPUs.

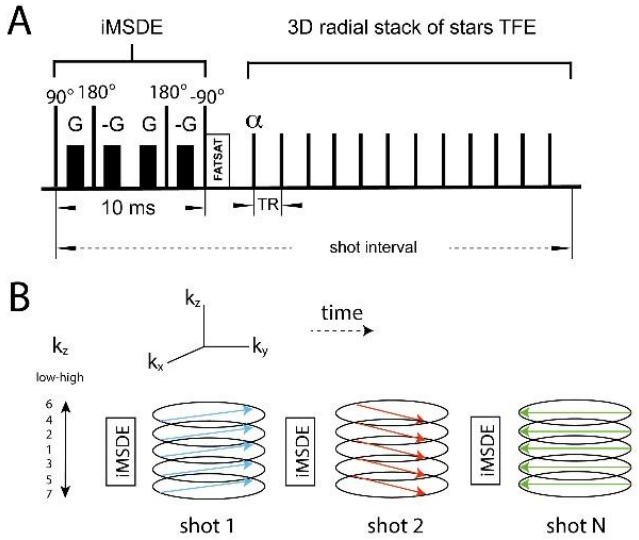

Figure 1. The accelerated black-blood DCE pulse sequence. A) A 3D Fast-Field Echo module is preceded by an iMSDE pre-pulse and spectrally selective fat saturation. B) A stack-of-stars readout with golden angle increments covers the k-space. To ensure efficient blood and fat suppression, k-lines within each shot are ordered in a center-out fashion.

Signal values and tracer concentrations

In order to perform pharmacokinetic modeling using our proposed sequence, the signal evolution of the sequence during pre-contrast and post-contrast was modeled based on the Bloch equations. To this end, signal values were converted to tracer concentrations by a nonlinear fit of the steady-state signal for a T1 weighted FLASH sequence, interrupted by an iMSDE black-blood prepulse after every *K* pulses, given by [26]:

$$Mss = \frac{M_0(1-E1)E2\sin\beta}{1-E1\cos\beta}\,\frac{1-(E1\cos\beta)^K}{1-E2\,(E1cos\beta)^K} \qquad (2)$$

where M_0 is the full relaxation, E2 represents T2 decay between the last RF-pulse and *TE*, β is the flip angle, and E1 represents T1 recovery. It is clear that this steady state has both T1 as well as T2 weighting. The parameter M_0 was found by solving the signal equation for the time-frames before contrast injection. Using this M_0, E1 and E2 can be found by a nonlinear fit of the signal value for every time point after contrast injection. The dynamic R1 and R2 values are to Gadolinium concentrations in the tissue, using the following equations:

$$R_1(t) = R_{1,0}(t) + r_1C(t); \qquad R_2(t) = R_{2,0}(t) + r_2C(t) \qquad (3)$$

where the relaxitivities used were r_1=4.5 L/mmol/s, r_2=5.09 L/mmol/s.

Pharmacokinetic analysis using an adaptation to the Reference Region model

The original CERRM method [18] is a least-squares solution of A**x**=b, where A contains the signal concentration and B is a matrix containing integrals of the muscle and signal-of-interest concentrations. **x** is a vector containing linear combinations of the PK parameters. The CERRM methods consists of two steps: the first one (ERRM) fits a model for all voxels. The fitted parameter **x** is a vector consisting of four terms, x_1 to x_4, which are linear combinations of the (relative) pharmacokinetic parameters. Subsequently, a second fit is done with a $k_{ep,RR}$ fixed for all voxels. In the second fit, a three-term vector **y** is fitted. However, we have experienced in our analyses that the global solution to this problem sometimes results in unphysical (negative) values for $k_{ep,RR,}$ or other PK parameters. To prevent this, we have introduced additional constraints to this model, and solve it by minimization of an l_2 norm:

$$\min|Ax - b|_2^2 \; s.t. \; k_{ep,rr} > 0 \tag{4}$$

.

From the model, we know:

$$k_{ep,RR} = 0.5\,\frac{x_1}{x_3} - 0.5\sqrt{\left(\frac{x_1}{x_3}\right)^2 - 4\,\frac{x_2}{x_3}} \tag{5}$$

Using the nonnegativity constraint, the term inside the square root cannot be negative and therefore we constrain:

$$\min|Ax - b|_2^2 \; s.t. \;\; x_1^2 > 4x_2x_3, \;\; x_n > 0. \tag{6}$$

Similarly, in the second step of [18] we added additional constraints to ensure a positive K^{trans}:

$$\min|Gy - b|_2^2 \; s.t. \;\; y_1 > y_2y_3 \tag{7}$$

The constrained fit was performed in Matlab (v2018a, The Mathworks, Natick, Massachusetts), and the YALMIP toolbox [27].

Area-under-the-curve (AUC) analysis

Signal-intensity time curves of the ROI were generated, in which the signal was normalized by removing and dividing by the pre-injection baseline signal. The relative area-under-the-curve (AUC) was calculated for all analyzed tissues by summing the normalized signal intensity for the two minutes following injection.

Monte Carlo Simulations

The performance of the CERRM method was investigated by means of numerical simulations. In the simulations, we focus on atherosclerotic plaque applications. First, we estimated how much parameters deviated from true values in the range of PK parameters expected in atherosclerotic plaques. Secondly, we compare the CERRM with 1) an ERRM, 2) a Patlak model with known AIF [28], and 3) a semi-quantitative AUC, to estimate how derived parameters differed between tissues.

An arterial input function (AIF) $C_p(t)$ was simulated, according to the Parker model [28], which is an empirically derived function consisting of two Gaussians plus an exponential decay. The contrast concentration in the simulated tissue-of-interest (TOI) and reference-region (RR), $C_t(t)$ and $C_{RR}(t)$ respectively, was simulated with the Extended Tofts model [16]:

$$C_t(t) = v_p C_p(t) + K_{trans} \int_0^t C_p(\tau)\, e^{-\left(\frac{K_{trans}}{v_e}(\tau - t)\right)} d\tau \ , \qquad (8)$$

where values of K^{trans}, v_p, and v_e for the vessel wall (VW) and plaque components being intra-plaque hemorrhage (IPH); necrotic core (NC) and fibrous tissue (FT); were taken from probability ranges constructed from reported literature values [2], [26], [29]–[33]; and for reference muscle a fixed literature value was used [34]. Relaxation values were fixed and taken from [5]. All values used in the simulations are reported in Table 1.

Table 1. Parameters used for Monte Carlo simulation and fitting. For image analysis, only the relaxation parameters and the muscle PK parameters were used. For MC Simulations, PK parameters were sampled from a normal distribution with the means and standard deviations reported.

	Healthy vessel wall	**Necrotic Core**	**Fibrous Tissue**	**Intra-plaque Hemorrhage**	**Muscle**
K^{trans} (min^{-1})	0.0273 ± 0.0052	0.0221 ± 0.0034	0.0649 ± 0.01497	0.00595 ± 0.0077	0.14
v_p	0.0152 ± 0.0042	0.0248 ± 0.00311	0.1084 ± 0.0141	0.0042 ± 0.0025	0.07
v_e	0.53 ± 0.1	0.53 ± 0.1	0.53 ± 0.1	0.53 ± 0.1	0
T_1 (ms)	1150	1150	1150	500	1450
T_2 (ms)	54	37	56	107	50

To limit discretization errors, simulations were performed with a temporal resolution of 0.1 seconds. From the simulated CA concentrations, the signal was reconstructed using equations 2 and 3. Sequence parameters used were: TR/TE = 7.2/3.2 ms, FA=15 degrees, the iMSDE-pulse wait-time T_{iMSDE} was 11 ms. For the error

simulations, five different noise regimes were simulated (0, $5x10^{-5}$, 10^{-4}, $5x10^{-4}$, 10^{-3} x M_0 respectively), and 50 signals were simulated for every tissue/noise combination. For the second simulation, no noise was added, and N=250 signal evolutions were simulated per tissue.

Patient data

Data was analyzed from two different ongoing clinical studies which involved measurements of PAD and AAA patients. Patients were recruited based on the presence of atherosclerotic plaques in the femoral arteries as detected by duplex ultrasound or presence of an asymptomatic AAA of at least 30 mm in diameter, respectively. Studies were conducted in accordance with the Declaration of Helsinki, the approval of the ethics committee of the Academic Medical Center and the written informed consent of all participants.

Sequence parameters for the 3D black-blood iMSDE DCE acquisitions in both applications are given in Table 2. All scans were performed on a Philips Ingenia 3T MRI system using a 32-channel torso coil. 3D black-blood iMSDE prepared DCE scan was performed 4 min. before and at least 5 min. after intravenous infusion of a Gd-based contrast agent (Gadovist; 0.1 mmol/kg). In case of femoral artery imaging, the field-of-view covered both femoral arteries. As the reference region, a region of the abdominal muscle was used. From all patients, a total of 18 DCE datasets from different plaques were used. In addition, 10 femoral artery segments from age- and sex-matched controls were included.
AAA patients were scanned twice with a one-week interval. From all available scan-rescan datasets, seven were included in this study based on sufficient image quality in both scans. As a reference region, a region of the back muscle was used.

CERRM analysis was performed in Matlab (Mathworks, USA) and Python. Signal intensity curves were converted to concentration curves using the signal model described in Equation 4. Pre-contrast vessel-wall T1 and T2 values were used from literature values (Table 1).

Table 2 Anatomy-specific scan parameters of the iMSDE-DCE sequence.

	PAD	AAA
Scan time	478 s	501 s
Resolution (mm^3)	0.7 x 0.7 x 2	1.2 x 1.2 x 3
FOV (mm^3)	250 x 250 x 60	420 x 420 x 87
FOV orientation	coronal	coronal
Golden Angle (deg)	38.98	111.25
Spokes per frame	37	34
Temporal resolution (s)	9.8	8.5

FA	15	11
TR/TE (ms)	7.38 / 3.22	7.37/3.46
TFE-factor	36	35
Coil compression channels	6	5
Total spokes	1800	1584
Kz oversampling	1.2	1.2
Total number of frames	48	46
Z-stack size (no oversampling)	36 (30)	35 (29)

Analysis of plaque composition in PAD patients

PAD patient and control data was delineated as described in Chapter 3 (healthy control VW; in patients: plaque; lipid; and non-plaque vessel wall). The delineated vessel wall components regions were transferred to the CERRM $K^{trans,ref}$ maps. Additionally, a simple area-under-the-curve analysis was also done. The $K^{trans,ref}$ and AUC values for all analyzed voxels were collected and the distribution of these for the different components were compared using a cumulative-density function (CDF). The average $K^{trans,ref}$ for every plaque component and every patient was collected and analyzed by means of a mixed linear model.

Analysis of AAA patient data

For the AAA patient group, the area of the aneurysm wall and muscle region-of-interest was delineated manually using VesselMass (Leiden University Medical Center, the Netherlands) in both scan and re-scan datasets. The volumetric $K^{trans,ref}$ maps were divided into three parts in the foot-head direction, and 12 parts in the circular direction centered around the centroid of the segmentation. The mean $K^{trans,ref}$ in the resulting segments was compared for the scan and re-scan, and the coefficients of variation (CoV) were calculated from this dataset for all patients and all segments.

4.4 Results

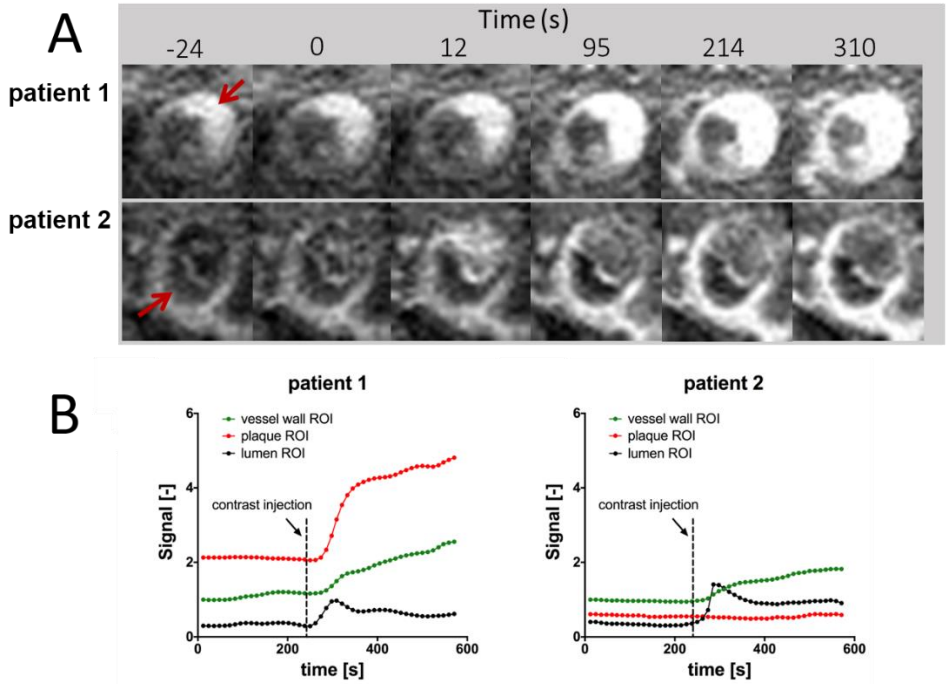

Figure 2. 3D black-blood DCE of femoral arteries, showing A) close-ups of two arterial plaques from two different patients (red arrows), and B) the signal intensity in the plaque, lumen and vessel wall. In patient 1, high enhancement of the plaque was observed. On the other hand, in patient 2, the plaque intensity does not change substantially over time, while the border between the plaque and the lumen does enhance strongly. This agrees with the presence of a lipid necrotic core.

Figure 2 shows close-ups of two different arterial plaques. A wide variety of uptake enhancement patterns was seen in the femoral plaque patient population. Adequate blood suppression was maintained throughout the dynamic scan.

The percentage error of PK parameters from the original ERRM method and the ERRM with additional fit constraints is shown in Figure 3. For both methods, the errors in v_p are very small; only with increasing noise does the error grow for IPH – however the v_p is very low in IPH to begin with. For the parameters K^{trans} and k_{ep}, the additional fit constraints considerably stabilize the fits, showing smaller median errors and smaller interquartile ranges. A positive bias was found in k_{ep} estimates, for VW and NC. For fibrous tissue however, there is sometime a large underestimation in k_{ep}. This is accompanied by a similar overestimation in K^{trans}. For

the other tissues, K^{trans} was accurate (median error 10 to 20 percent) over the simulated noise ranges.

A histogram of Monte Carlo data comparing different analysis methods for a range of plaque tissues is shown in Figure 4. The largest spread of values is found for a Patlak analysis. Both Reference Region models show very consistent estimates, making distinguishing between healthy and diseased tissue possible. In contrast, Patlak analysis (with a known AIF) gives wider estimates and discrimination between tissue types is compromised.

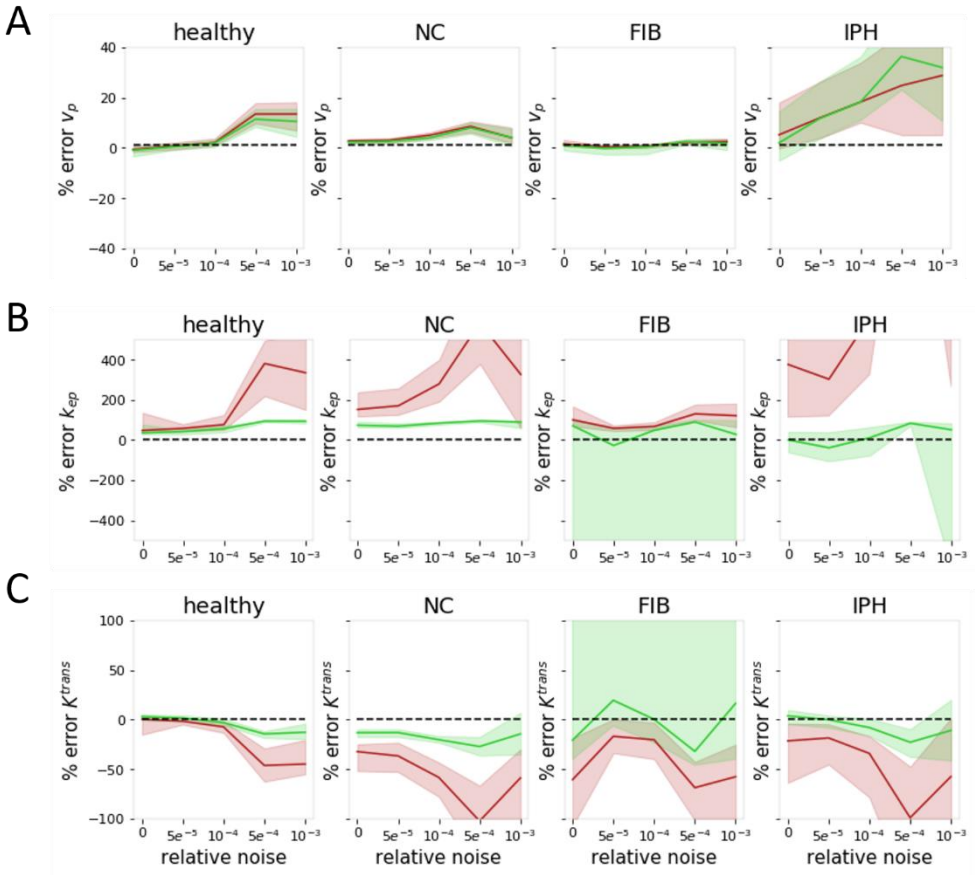

Figure 3. Monte Carlo simulation. Relative error for estimate of PK parameters from the ERRM, original (green), and with a constrained fit method (Red). The solid line shows the median of 50 simulations, and the shaded area signifies the interquartile region. A) The estimates for v_p show a very low error percentage for both methods, even for the higher noise regions, over all the four simulated tissue types. In contrast, estimates for k_{ep}, shown in B), show a positive bias for healthy VW tissue and necrotic core. The constrained fit shows lower error and smaller areas. Similarly, in C), the estimates for K^{trans} show a smaller error over all tissue types for the constrained fit over the unconstrained ERRM. Only the fibrous cap has a considerable number of estimates with over 100 percent error.

Pharmacokinetic parameter values were estimated for in-vivo PAD data. Compared to the reference method, the area-under-the-curve method did not give distinguishable results between control, non-plaque and plaque components. Cumulative probability density functions are shown in Figure 5. The cumulative density functions were more spread out for the $K^{trans,ref}$ values obtained from the adapted CERRM than for the AUC, suggesting that classifying plaque type would be easier using the PK parameter derived from a reference region than using an AUC. A linear mixed model was used for analysis: for the AUC a r^2=0.181 was found, for the adapted CERRM r^2=0.469.

Figure 6 shows a typical example of a AAA patient. Excellent blood suppression was generally found throughout the acquired volume. Heterogeneous enhancement was seen on the AAA wall. A reproducibility analysis for the scan-rescan data of the AAA patients is shown in Figure 7. In general, the method was moderately reproducible. Notably, the additional constraints we added on the CERRM increased the reproducibility; the coefficient of variation improved from 66 to 49 percent.

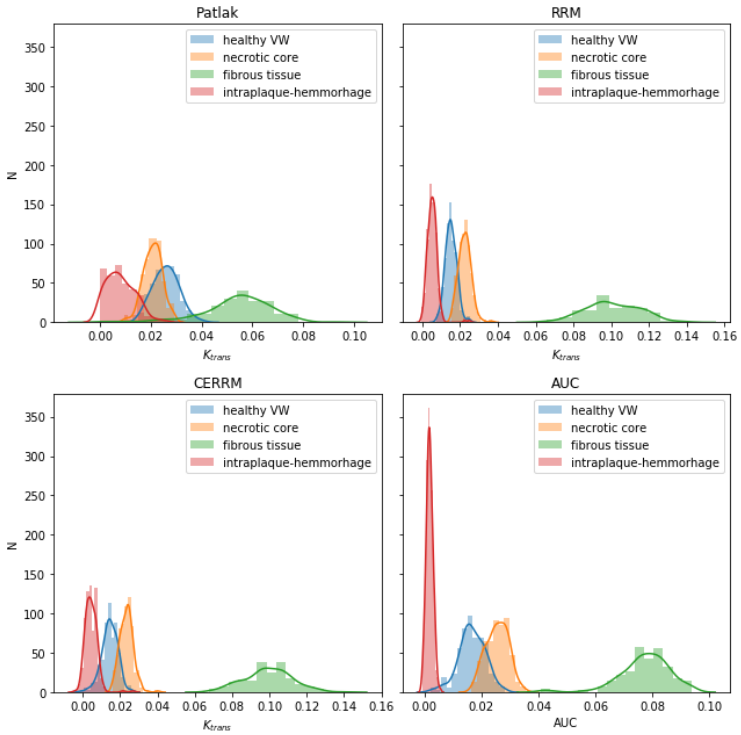

Figure 4. Histogram of Monte Carlo simulation (*N*=250). The Patlak model shows the largest spread of estimated values, and therefore discriminating between the different types of healthy and diseased tissues is more difficult than either reference region method, or even the AUC.

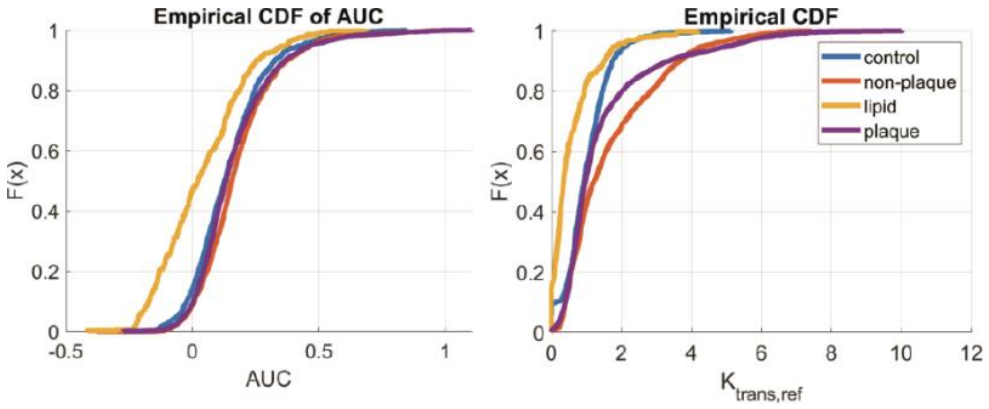

Figure 5. Cumulative Density Functions (CDF) of parameter values of all femoral data. The Area-under-the-curve measure is more similar between the different tissue types than the fitted $K^{trans,ref}$ values.

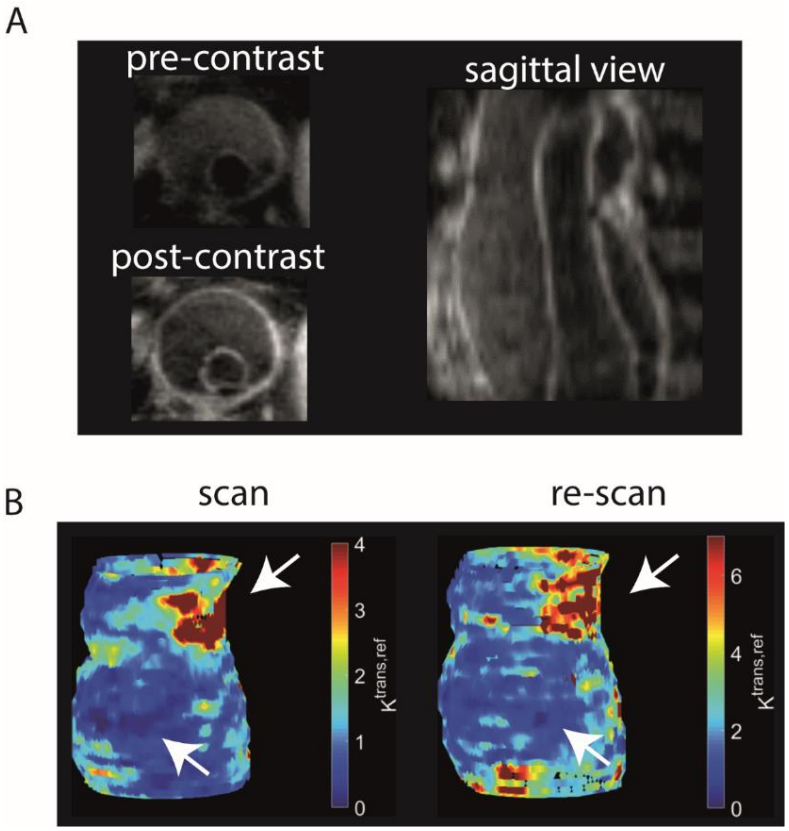

Figure 6. A. Example AAA images, pre- and post-contrast. Good blood signal suppression remains after contrast injection. B. Voxel-wise $K^{trans,ref}$ maps show very good and well-reproducible localization of high- and low uptake regions.

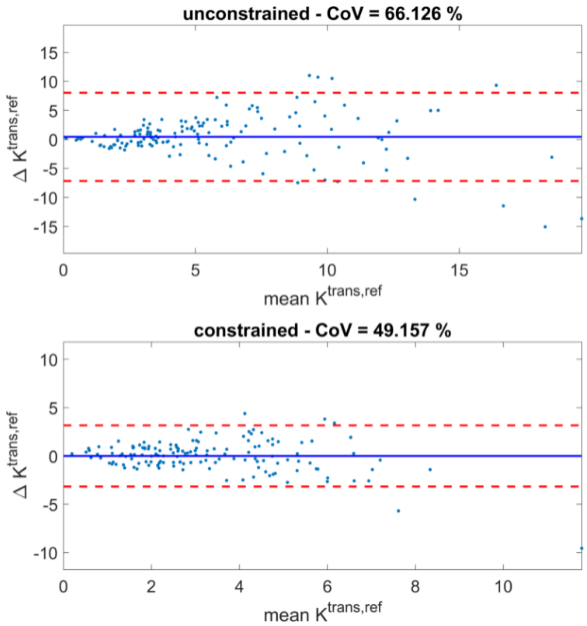

Figure 7. Bland-Altman plots of the $K^{trans,ref}$ of the original (unconstrained) and constrained CERRM methods.

4.5 Discussion

We found that we were able to consistently achieve adequate blood suppression in our black-blood DCE scans. While the lumen signal increased slightly, it did not cause serious flow artifacts or signal bleed into the surrounding tissue. Although the sequence was heavily under sampled, image quality remained good and delineation between vessel wall, lumen and plaque was clear. In some patients with femoral plaques, lipid core regions were characterized by a strong hypointense pre-contrast signal. This may be explained by repetitive use of the T2-preparation in combination with short TFE shots and the low T2 values of the lipid core. This sequence could be easily applied in other areas of the vascular bed, such as the carotid arteries.

Distinguishing between healthy and diseased tissue

The ability of the CERRM to discriminate between different tissue types in PAD patients and controls, much better than a semi-quantitative parameter like AUC, shows that the reference-based K^{trans} adds valuable information. The Monte Carlo simulations suggested that the CERRM could better distinguish plaque components than the Patlak model. This could be explained by the temporal robustness of the reference region methods, which have been shown to receive better permeability estimates than traditional AIF-based fitting for moderate temporal resolutions [15]. Compared to the discrimination ability of semi-quantitative markers, such as AUC,

the effect of permeability and other variables, such as vascular or plasma fractions, are better resolved in CERRM.

Reproducibility

A voxel wise $K^{trans,ref}$ map of both the scan and rescan (Fig. 3B) shows good spatial correspondence of the high and the low enhancement regions. The scan-rescan coefficient of variation was 49 percent. Nguyen [35] found a AAA scan-rescan CoV of 38% in a 2D bright-blood sequence with a Patlak fit. We found a CoV that is slightly worse. This may be caused by the mis-registration between scan and rescan which could be improved by elastic registration.

Additional constraints to the CERRM

The additional constraints gave considerably smaller errors in the relevant parameter space for atherosclerotic imaging. In the Monte Carlo simulations in Figure 3, we see a similar performance for v_p, smaller errors in k_{ep} and K^{trans} for all tissues except the fibrous cap, where the median value estimate is good, but for some simulations, a considerable error, leading to a positive bias in K^{trans} for fibrous tissue. A similar bias can be seen in the histogram of Figure 3.

The constrained fit lowered the CoV from 66% to 49%, it also removed the bias (Fig. 7). Additionally, the constraint has removed unphysical values entirely (i.e. negative K^{trans}, negative v_e, v_p). Also, the fit cost has substantially lowered, while we saw that the overall $K^{trans,ref}$ distribution remained similar.

Future outlook

Ideally, robust, high-resolution T_1 and T_2 estimates would be necessary to do a full analysis. Unfortunately, quantitative MRI is very slow and unfeasible for coverage and resolution described here.

We were unable to compare an in-vivo scan with a known AIF to our AIF-free method, due to the inability to scan two protocols after each other in the same volunteer (the T1-effects of Gd injection remain for a long time).

The combination of a CERRM approach with a highly accelerated golden-angle strategy sampling DCE protocol is very promising. While high spatial and temporal resolutions are achievable in this way, a sub-second temporal resolution remains out of grasp, and therefore indirect PK estimation methods will be useful. New reference region work using a low-temporal resolution AIF-tail could improve reproducibility, as fewer assumptions would be necessary [36].

4.6 Conclusion

We have shown the feasibility of 3D black blood dynamic contrast enhancement, with sufficient resolution to determine the vessel wall and plaque. In all cases, the blood signal was sufficiently suppressed throughout the scan. We were able to model PK parameters without an AIF, using the constrained extended reference region with additional constraints. Reproducibility in a patient population with abdominal aortic aneurysm was moderate. According to Monte Carlo simulations and patient data, good discrimination of vessel wall and plaque tissue types was found.

4.7 References

[1] W. Kerwin, A. Hooker, M. Spilker, P. Vicini, M. Ferguson, T. Hatsukami, and C. Yuan, "Quantitative Magnetic Resonance Imaging Analysis of Neovasculature Volume in Carotid Atherosclerotic Plaque," vol. i, 2003.

[2] W. S. Kerwin, K. D. O'Brien, M. S. Ferguson, N. Polissar, T. S. Hatsukami, and C. Yuan, "Inflammation in carotid atherosclerotic plaque: A dynamic contrast-enhanced MR imaging study," *Radiology*, vol. 241, no. 2, pp. 459–468, 2006.

[3] R. H. M. van Hoof, S. Heeneman, J. E. Wildberger, and M. E. Kooi, "Dynamic Contrast-Enhanced MRI to Study Atherosclerotic Plaque Microvasculature.," *Curr. Atheroscler. Rep.*, vol. 18, no. 6, p. 33, 2016.

[4] K. H. Zheng, J. Schoormans, L. C. A. Stiekema, C. Calcagno, I. Cicha, C. Alexiou, G. J. Strijkers, A. J. Nederveen, E. S. G. Stroes, and B. F. Coolen, "Plaque Permeability Assessed With DCE-MRI Associates With USPIO Uptake in Patients With Peripheral Artery Disease," *JACC Cardiovasc. Imaging*, pp. 24–25, 2019.

[5] H. Qi, F. Huang, Z. Zhou, P. Koken, N. Balu, B. Zhang, C. Yuan, and H. Chen, "Large coverage black-bright blood interleaved imaging sequence (LaBBI) for 3D dynamic contrast-enhanced MRI of vessel wall," *Magn. Reson. Med.*, vol. 00, 2017.

[6] L. Feng, R. Grimm, K. T. obias Block, H. Chandarana, S. Kim, J. Xu, L. Axel, D. K. Sodickson, and R. Otazo, "Golden-angle radial sparse parallel MRI: combination of compressed sensing, parallel imaging, and golden-angle radial sampling for fast and flexible dynamic volumetric MRI," *Magn. Reson. Med.*, vol. 72, no. 3, pp. 707–717, 2014.

[7] L. E. Kershaw and H. L. M. Cheng, "A general dual-bolus approach for quantitative DCE-MRI," *Magn. Reson. Imaging*, vol. 29, no. 2, pp. 160–166, 2011.

[8] T. Wu, J. Wang, Y. Song, X. Deng, A. Li, J. Wei, L. He, X. Zhao, R. Li, Z. Zhou, W. Wu, J. Huang, S. Jiao, C. Yuan, and H. Chen, "Homologous black-bright-blood and flexible interleaved imaging sequence (HOBBI) for dynamic contrast-enhanced MRI of the vessel wall," *Magn. Reson. Med.*, vol. 73, no. 5, pp. 1754–1763, 2015.

[9] T.-Y. L. Elizabeth Henderson, Brian K. Rutt, "Temporal sampling requirements for the tracer kinetics modeling of breast disease," *Magn. Reson. Imaging*, vol. 16, no. 9, pp. 1057–1073, 1998.

[10] C. Calcagno, P. M. Robson, S. Ramachandran, V. Mani, M. Kotys-Traughber, M. Cham, S. E. Fischer, and Z. A. Fayad, "SHILO, a novel dual imaging approach for simultaneous HI-/LOw temporal (Low-/Hi-spatial) resolution imaging for vascular dynamic contrast enhanced cardiovascular magnetic resonance: numerical simulations and feasibility in the carotid arteries," *J Cardiovasc Magn Reson*, vol. 15, no. 1, p. 42, 2013.

[11] Z. Zhou, B. Sharif, Z. Fan, Y. Xie, and D. Li, "High spatial and temporal resolution black-blood dynamic contrast-enhanced carotid artery wall MRI using compressed sensing," *J. Cardiovasc. Magn. Reson.*, vol. 16, no. Suppl 1, p. W40, 2014.

[12] C. Calcagno, E. Vucic, V. Mani, G. Goldschlager, and Z. A. Fayad, "Reproducibility of Black Blood Dynamic Contrast- Enhanced Magnetic Resonance Imaging in Aortic Plaques of Atherosclerotic Rabbits," vol. 198, pp. 191–198, 2010.

[13] C. Mri, H. Chen, J. Ricks, M. Rosenfeld, and W. S. Kerwin, "Progression of Experimental Lesions of Atherosclerosis : Assessment by Kinetic Modeling of Black-Blood Dynamic," vol. 1720, pp. 1712–1720, 2013.

[14] T. E. Yankeelov, J. J. Luci, M. Lepage, R. Li, L. Debusk, P. C. Lin, R. R. Price, and J. C. Gore, "Quantitative pharmacokinetic analysis of DCE-MRI data without an arterial input function: A reference region model," *Magn. Reson. Imaging*, vol. 23, no. 4, pp. 519–529, 2005.

[15] M. Heisen, X. Fan, J. Buurman, N. A. W. Van Riel, G. S. Karczmar, and B. M. Ter Haar Romeny, "The use of a reference tissue arterial input function with low-temporal-resolution DCE-MRI data," *Phys. Med. Biol.*, vol. 55, no. 16, pp. 4871–4883, 2010.

[16] P. S. Tofts, "Modeling Tracer Kinetics in Dynamic Gd-DTPA MR Imaging," *J. Magn. Reson. Imaging*, vol. 7, no. 1, pp. 91–101, 1997.

[17] M. E. Gaens, W. H. Backes, S. Rozel, M. Lipperts, S. N. Sanders, K. Jaspers, J. P. M. Cleutjens, J. C. Sluimer, S. Heeneman, M. J. A. P. Daemen, R. J. T. J. Welten, J. W. H. Daemen, J. E. Wildberger, R. M. Kwee, and M. E. Kooi, "Dynamic contrast-enhanced MR imaging of carotid atherosclerotic plaque: Model selection, reproducibility, and validation," *Radiology*, vol. 266, no. 1, pp. 271–279, 2013.

[18] Z. Ahmed and I. R. Levesque, "An extended reference region model for DCE-

MRI that accounts for plasma volume," *NMR Biomed.*, vol. 31, no. 7, pp. 1–13, 2018.

[19] J. Schoormans, K. Zheng, E. Stroes, G. Strijkers, A. Nederveen, and B. Coolen, "3D Black-Blood DCE-MRI Using Radial Stack-Of-Stars Acquisition and CS Reconstruction: Application in Carotid and Femoral Arteries," in *Proceedings of the Annual Meeting of the ISMRM*, 2017.

[20] J. Wang, V. L. Yarnykh, and C. Yuan, "Enhanced image quality in black-blood MRI using the improved motion-sensitized driven-equilibrium (iMSDE) sequence," *J. Magn. Reson. Imaging*, vol. 31, no. 5, pp. 1256–1263, 2010.

[21] S. Wundrak, J. Paul, J. Ulrici, E. Hell, and V. Rasche, "A small surrogate for the golden angle in time-resolved radial MRI based on generalized fibonacci sequences," *IEEE Trans. Med. Imaging*, vol. 34, no. 6, pp. 1262–1269, 2015.

[22] L. Feng, L. Axel, H. Chandarana, K. T. Block, D. K. Sodickson, and R. Otazo, "XD-GRASP: Golden-angle radial MRI with reconstruction of extra motion-state dimensions using compressed sensing," *Magn. Reson. Med.*, vol. 75, no. 2, pp. 775–788, 2016.

[23] M. Buehrer, K. P. Pruessmann, P. Boesiger, and S. Kozerke, "Array compression for MRI with large coil arrays," *Magn. Reson. Med.*, vol. 57, no. 6, pp. 1131–1139, 2007.

[24] D. O. Walsh, "Adaptive Reconstruction and Enhancement of Phased Array MR Imagery," *Magn. Reson. Med.*, vol. 5067, no. 520, pp. 1–23.

[25] D. K. S. Florian Knoll, Andreas Schwarzl, Clemens Diwoky, "gpuNUFFT - An open source GPU library for 3D regridding with direct Matlab interface Florian," *Int. Soc. Magn. Reson. Med.*, pp. 4297–4297, 2014.

[26] H. Qi, F. Huang, Z. Zhou, P. Koken, N. Balu, B. Zhang, C. Yuan, and H. Chen, "Large coverage black-bright blood interleaved imaging sequence (LaBBI) for 3D dynamic contrast-enhanced MRI of vessel wall," *Magn. Reson. Med.*, vol. 79, no. 3, pp. 1334–1344, 2018.

[27] J. Löfberg and L. Johan, "YALMIP : A toolbox for modeling and optimization in MATLAB," no. December, 2016.

[28] G. J. M. Parker, C. Roberts, A. Macdonald, G. A. Buonaccorsi, S. Cheung, D. L. Buckley, A. Jackson, Y. Watson, K. Davies, and G. C. Jayson, "Experimentally-derived functional form for a population-averaged high-temporal-resolution arterial input function for dynamic contrast-enhanced MRI," *Magn. Reson. Med.*, vol. 56, no. 5, pp. 993–1000, 2006.

[29] M. T. B. Truijman, R. M. Kwee, R. H. M. Van Hoof, E. Hermeling, R. J. Van Oostenbrugge, W. H. Mess, W. H. Backes, M. J. Daemen, J. Bucerius, J. E. Wildberger, and M. E. Kooi, "Combined 18F-FDG PET-CT and DCE-MRI to assess inflammation and microvascularization in atherosclerotic plaques," *Stroke*, vol. 44, no. 12, pp. 3568–3570, 2013.

[30] J. Sun, Y. Song, H. Chen, W. S. Kerwin, D. S. Hippe, L. Dong, M. Chen, C. Zhou, T. S. Hatsukami, and C. Yuan, "Adventitial perfusion and intraplaque hemorrhage: A dynamic contrast-enhanced MRI study in the carotid artery," *Stroke*, vol. 44, no. 4, pp. 1031–1036, 2013.

[31] K. D. O'Brien, D. S. Hippe, H. Chen, M. B. Neradilek, J. L. Probstfield, S. Peck, D. A. Isquith, G. Canton, C. Yuan, N. L. Polissar, X. Q. Zhao, and W. S. Kerwin, "Longer duration of statin therapy is associated with decreased carotid plaque vascularity by magnetic resonance imaging," *Atherosclerosis*, vol. 245, pp. 74–81, 2016.

[32] H. Chen, J. Cai, X. Zhao, H. Underhill, H. Ota, M. Oikawa, L. Dong, C. Yuan, and W. S. Kerwin, "Localized measurement of atherosclerotic plaque inflammatory burden with dynamic contrast-enhanced MRI," *Magn. Reson. Med.*, vol. 64, no. 2, pp. 567–573, 2010.

[33] C. Calcagno, S. Ramachandran, D. Izquierdo-Garcia, V. Mani, A. Millon, D. Rosenbaum, A. Tawakol, M. Woodward, J. Bucerius, E. Moshier, J. Godbold, D. Kallend, M. E. Farkouh, V. Fuster, J. H. F. Rudd, and Z. A. Fayad, "The complementary roles of dynamic contrast-enhanced MRI and 18F-fluorodeoxyglucose PET/CT for imaging of carotid atherosclerosis," *Eur. J. Nucl. Med. Mol. Imaging*, vol. 40, no. 12, pp. 1884–1893, 2013.

[34] Z. Ahmed and I. R. Levesque, "An extended reference region model for DCE-MRI that accounts for plasma volume," *NMR Biomed.*, vol. 31, no. 7, pp. 1–13, 2018.

[35] V. L. Nguyen, M. E. Kooi, W. H. Backes, R. H. M. Van Hoof, A. E. C. M. Saris, M. C. J. Wishaupt, F. A. M. V. I. Hellenthal, R. J. Van Der Geest, A. G. H. Kessels, G. W. H. Schurink, and T. Leiner, "Suitability of Pharmacokinetic Models for Dynamic Contrast-Enhanced MRI of Abdominal Aortic Aneurysm Vessel Wall : A Comparison," vol. 8, no. 10, pp. 6–12, 2013.

[36] Z. Ahmed and I. R. Levesque, "Pharmacokinetic modeling of dynamic contrast-enhanced MRI using a reference region and input function tail," *Magn. Reson. Med.*, vol. 83, no. 1, pp. 286–298, 2020.

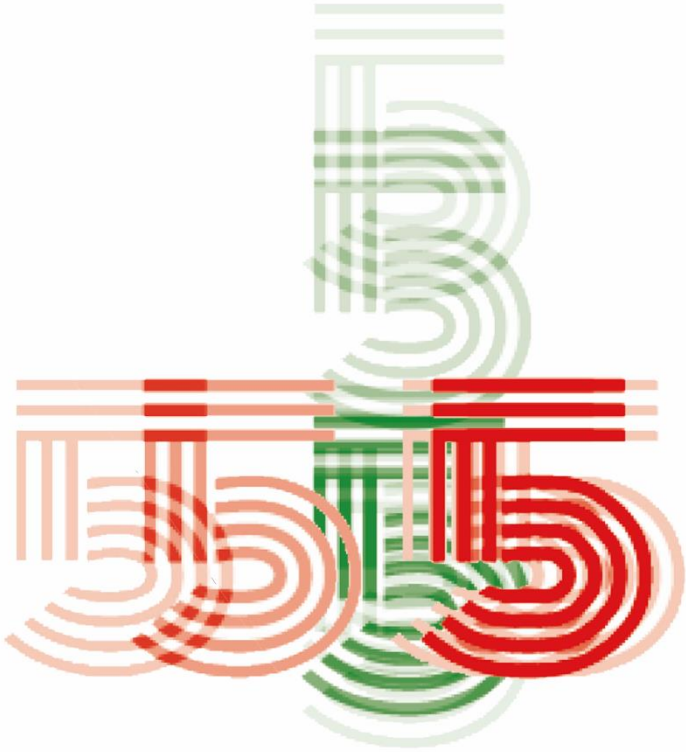

Chapter 5

An iterative sparse deconvolution method for simultaneous multicolor ^{19}F-MRI of multiple contrast agents

Jasper Schoormans,
Claudia Calcagno,
Mariah R R Daal,
Rob C I Wüst,
Christopher Faries,
Alexander Maier,
Abraham J P Teunissen,
Sonum Naidu,
Brenda L Sanchez-Gaytan,
Aart J Nederveen,
Zahi A Fayad,
Willem J M Mulder,
Bram F Coolen,
Gustav J Strijkers

Published in Magnetic Resonance in Medicine, 2020; 83(1):228-231

5.1 Abstract

Purpose: ^{19}F-MRI is gaining widespread interest for cell tracking and quantification of immune and inflammatory cells in-vivo. Different fluorinated compounds can be discriminated based on their characteristic MR spectra, allowing in-vivo imaging of multiple ^{19}F compounds simultaneously, so-called multicolor ^{19}F-MRI . We introduce a method for multicolor ^{19}F-MRI using an iterative sparse deconvolution method to separate different ^{19}F compounds and remove chemical shift artifacts arising from multiple resonances.

Methods: The method employs cycling of the readout gradient direction to alternate the spatial orientation of the off-resonance chemical shift artifacts, which are subsequently removed by iterative sparse deconvolution. Noise robustness and separation was investigated by numerical simulations. Mixtures of fluorinated oils (PFCE and PFOB) were measured on a 7T MR scanner to identify the relation between ^{19}F signal intensity and compound concentration. The method was validated in a mouse model after intramuscular injection of fluorine probes, as well as after intravascular injection.

Results: Numerical simulations show efficient separation of ^{19}F compounds, even at low SNR. Reliable chemical shift artifact removal and separation of PFCE and PFOB signals was achieved in phantoms and in-vivo. Signal intensities correlated excellently to the relative ^{19}F compound concentrations (r^2=0.966/0.990 for PFOB/PFCE).

Conclusions: The method requires minimal sequence adaptation, and is therefore easily implemented on different MRI systems. Simulations, phantom experiments, and in-vivo measurements in mice showed effective separation and removal of chemical shift artifacts below noise level. We foresee applicability for simultaneous in-vivo imaging of ^{19}F-containing fluorine probes or for detection of ^{19}F-labeled cell populations.

5.2 Introduction

Fluorine (^{19}F) magnetic resonance imaging (MRI) is rapidly gaining traction for in vivo cell tracking as it possesses several advantages over traditional ^{1}H MRI and other imaging methods[1]. Firstly, the human body contains negligible amounts of ^{19}F. Therefore, any detected ^{19}F-MRI signal originates solely from exogenously administered fluorine probes, making accurate quantification possible [2]. Secondly, since the ^{19}F resonates at a frequency distinguishable from ^{1}H, the ^{19}F signal does not influence the ^{1}H contrast, allowing imaging with regular PD, T1- and T2-weighted ^{1}H-MRI.

For most cell tracking and inflammation ^{19}F-MRI studies, perfluorocarbon (PFC) based nanoparticles are applied [3]–[5] . Upon intravenous injection, these fluorinated nanoparticles accumulate at inflamed tissues, hematopoietic organs, such as the bone marrow and spleen, as well as in the liver, where they are taken up by phagocytic cells. So far, ^{19}F-MRI has shown great potential and has been explored in a variety of studies including Alzheimer's disease, lung imaging, cancer, myocardial infarction and stroke, and inflammatory bowel disease [2], [6]–[8].
The different PFCs differ from one another in terms of the number of ^{19}F resonances and their chemical shifts. This enables unambiguous discrimination on the basis of their MR spectrum. This property has been previously exploited to separate confounding signal from isoflurane (a commonly used anesthetic) from the ^{19}F signal of interest [9]. More importantly, these differences can be leveraged to detect different ^{19}F-containing nanoparticles –and thus populations of ^{19}F-labeled cells– in the same sample and in the same imaging session, enabling "multicolor" or "multiplex" ^{19}F-MRI. This technique has potential as an in vivo, non-invasive readout of tissue immune cells composition, similar to commonly used ex vivo immunological assays, such as flow cytometry.

However, recording multiple ^{19}F resonances in a single MR spectrum gives rise to chemical shift artifacts, which present themselves as signal ghosts in the readout gradient direction and hinder accurate localization and quantification. Several strategies have been proposed to avoid or mitigate these. The first is spectrally selective excitation and selective suppression of certain resonances [10]–[13] ,which can also be used to image multiple different compounds [14]–[16], at the cost of increased scan times and excluding signal of non-excited resonances.
A second strategy is chemical shift imaging (CSI) [17][18]. CSI suffers from long acquisition times though and therefore acceleration by the use of pseudo-radial projections [19] and compressed sensing [20] has been proposed. While effective in terms of SNR [21], lengthy acquisitions remain a problem for 3D acquisitions at moderate to high spatial and spectral resolutions. DIXON-type bSSFP (Balanced

Steady-State Free Precession) and multi-echo acquisitions methods separate the ^{19}F resonances based on their phase evolution [9][22]. These methods require the acquisition of multiple echoes with increasing TE. This comes at the cost of increased scan time, and decreased SNR and increased sensitivity to T2* effects and motion with increasing TE.

As an alternative to acquisition-based methods, sensitivity encoding [23] includes coil sensitivities and spectra in a linear model, which is subsequently solved by pseudo-inversion. While artifact-free multicolor imaging was demonstrated, this method is prone to noise and in this implementation requires multiple coil elements. Finally, chemical shift artifacts can be resolved during image reconstruction. As early as in the 1980s, deconvolution methods were proposed as an approach to remove chemical shift image artifacts [24]. However, plain deconvolution in the presence of noise results in noise amplification, thereby affecting image quality. More advanced deconvolution algorithms, such as the reblurred deconvolution method [25], have been proposed to overcome this issue. More recently, iterative regularized deconvolution under the assumption of sparsity in the image domain as an additional prior [26] has been introduced. However, these deconvolution techniques do not allow discrimination of multiple fluorinated compounds because the underlying models assume an equal MR spectrum for all ^{19}F signal.

Here, we introduce an alternative deconvolution approach that is based on cycling of the readout gradient, allowing multicolor imaging of different ^{19}F compounds with complex and overlapping spectra. The method exploits the sparse nature of most ^{19}F images by iterative deconvolution, removes the chemical shift artifacts associated with multiple peaks in the ^{19}F spectra, and thereby enables discrimination of ^{19}F compounds in the resulting images. We show reliable separation and artifact removal in numerical simulations and in phantoms, as well as in mice after intramuscular injection of PFOB and PFCE nanoparticles and in mouse liver and spleen at several time points after intravenous administration.

5.3 Methods

Our method is based on a sequential or interleaved acquisition of images with different readout directions. While in our experiments we have used a 3D gradient echo (GE) acquisition (see Table 1 for imaging parameters), this method can be applied to 3D imaging (e.g. fast spin echo (FSE)), or any other sequences with predictable chemical shift artifacts, optimized to SNR per unit time. Imaging requires a broadband excitation to excite all peaks in the ^{19}F spectra and k-space sampling method resulting in well-defined chemical shift artifacts.

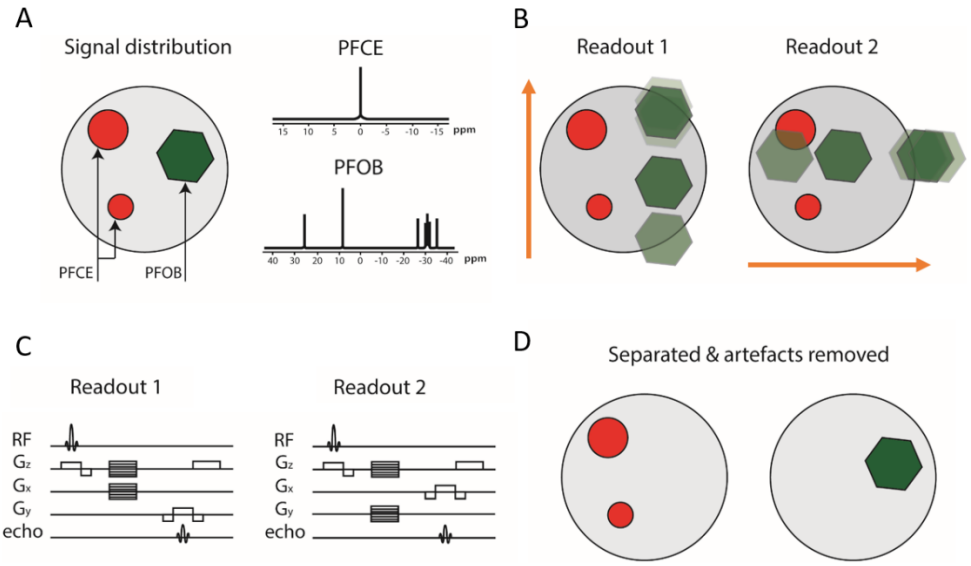

Figure 1. Schematic illustration of the technique to correct chemical shift artifacts and separate multiple compounds in ^{19}F-MRI. (A) PFOB and PFCE at different locations in the image. PFOB has a complex spectrum with several resonances, whereas PFCE has a single resonance. (B) Two acquisitions with readout in down-up and left-right directions (orange arrows), leading to chemical shift artifacts from the multiple PFOB resonances in vertical and horizontal direction, respectively. (C) The FLASH sequence diagrams describing the two acquisitions with different readout directions .(D) The 2 acquisitions are combined using the algorithm described, showing that PFOB and PFCE are separated and chemical shift artifacts resolved.

A two compound - two measurement model

We illustrate the method by considering two ^{19}F compounds with different resonance spectra, *i.e.* perfluorooctyl bromide (PFOB) and perfluoro-15-crown-5-ether (PFCE), in Figure 1A. PFOB has a complex ^{19}F spectrum with multiple resonance peaks originating from 1 CF_2Br, 1 CF_3, and 6 CF_2 groups, whereas PFCE has a single peak from 10 identical CF_2 groups at a different resonance frequency than those of PFOB [17].

To spectrally un-mix the two compounds in MR imaging, at least two acquisitions with different chemical shift artifact behavior are required, *e.g.* one with a readout direction in the horizontal orientation and one with the readout in the vertical direction. We will represent these measurements by the column vectors $\bar{y}_h$ and $\bar{y}_v$, respectively. Let F be the Fourier sampling operator, and C_h and C_v the circular convolution operators convolving an image with the spectrum of PFOB in horizontal and vertical directions of frequency encoding, respectively. A single reconstructed PFOB and PFCE image x_i will thus contain chemical shift artifacts, described by

$$\bar{x}_i = C_i\,\bar{x}_{PFOB} + \bar{x}_{PFCE} \quad with \quad i \in \{h, v\}. \tag{1}$$

Because PFCE has only a single peak which we center at 0 ppm, the sampling convolution operator for PFCE is the identity operator I. The full measurement model for two frequency encoding directions, horizontal h and vertical v, together now reads

$$\begin{pmatrix}\bar{y}_h\\ \bar{y}_v\end{pmatrix} = \begin{pmatrix}F & 0\\ 0 & F\end{pmatrix}\begin{pmatrix}C_h & I\\ C_v & I\end{pmatrix}\begin{pmatrix}\bar{x}_{PFOB}\\ \bar{x}_{PFCE}\end{pmatrix} + \bar{\eta}, \tag{2}$$

with $\bar{\eta}$ the noise contribution. Equation 2 can be generalized to

$$\bar{y} = \boldsymbol{M}\,\bar{x} + \bar{\eta}\,, \tag{3}$$

with $\boldsymbol{M}$ the full signal encoding matrix for both compounds and readout directions. The method is illustrated in Figure 1.

Generalization of the measurement model

The encoding matrix $\boldsymbol{M}$ can be extended in a straightforward way to include more ^{19}F-containing compounds and more measurements. One needs at least as many measurements as the number of ^{19}F-compounds to solve the reconstruction problem. A higher number of measurements would improve the robustness of the reconstruction. A generalized form of Eq. 2 with y measurements and x compounds reads

$$\begin{pmatrix}\bar{y}_1\\ \vdots\\ \bar{y}_N\end{pmatrix} = \begin{pmatrix}F & \cdots & 0\\ \vdots & \ddots & \vdots\\ 0 & \cdots & F\end{pmatrix}\begin{pmatrix}C_{1,1} & \cdots & C_{1,M}\\ \vdots & \ddots & \vdots\\ C_{N,M} & \cdots & C_{M,M}\end{pmatrix}\begin{pmatrix}\bar{x}_{PFC\text{-}1}\\ \vdots\\ \bar{x}_{PFC\text{-}M}\end{pmatrix} + \bar{\eta}\,, \tag{4}$$

where y_n are the N different directions acquired, and $x_{PFC\text{-}m}$ are the M different ^{19}F ^{19}F-containing compounds. $C_{n,m}$ are the expected spectra for compounds m and readout n. These can be varied by changing readout direction, like we have done in this paper, but also by e.g. modifying the readout bandwidth. The acquisitions y_n need not be full k-space acquisitions, but can be undersampled to accommodate parallel imaging or compressed sensing reconstructions.

Image reconstruction

Equation 3 can be solved by direct inversion, *i.e.* multiplying the measurement data by the pseudo-inverse of the signal encoding matrix $\boldsymbol{M}^+$, according to

$$\hat{\bar{x}} = \boldsymbol{M}^+\,\bar{y}. \tag{5}$$

However, this approach will induce noise amplification, even for very low noise levels [25]. To prevent this, Eq. 3 can be modified to a least absolute shrinkage and selection operator (LASSO)

$$\hat{\bar{x}} = \underset{\bar{x}}{arg\,min}\,||\bar{y} - \boldsymbol{M}\,\bar{x}\,||_2 + \lambda\big||W\,\bar{x}|\big|_1\,, \tag{6}$$

where W is an image transform, such as a wavelet transform or a total-variation operator, and λ a regularization parameter which controls the balance between sparsity and data consistency.
In this study, the wavelet transform was used, and the equation was solved with a non-linear conjugate gradient algorithm [27]. In addition to increased noise robustness, the LASSO method allows for flexibility in k-space acquisition, enabling advanced sampling schemes, such as random undersampling. As such, our approach is also fully compatible with compressed sensing acceleration.

Estimation of the convolution operator

The convolution operator (point-spread function) of PFOB is

$$C_i = \sum_{j=1}^{NR} \alpha_j \, \delta_j \frac{N_i}{BW}, \tag{7}$$

where NR is the number of resonances, α_j is the relative amplitude and δ_j (Hz) the chemical shift of resonance peak j, BW (Hz) the readout bandwidth, and N_i the matrix size in readout direction. PFOB has 7 resonances, but 3 of them are close and their relative chemical shift is generally smaller than a pixel. Therefore, we have used $NR = 5$ for PFOB in this study. The relative amplitudes and pixel shifts of C_i can be calculated from the theoretical spectrum or measured in a phantom with a pure compound.

Numerical simulation of noise robustness

The influence of noise on the ability of our algorithm to reconstruct and separate the signal of two ^{19}F-containing nanoemulsions was investigated by numerical simulations in Matlab (The MathWorks, Inc., Natick, Massachusetts, United States). A two-dimensional image of 64x64 pixels, containing two elliptical PFOB and two elliptical PFCE phantoms, was used. The PFOB chemical shift artifacts were calculated as in Equation 7. Two readout directions were simulated, and Gaussian noise was added to the fully sampled k-space. Reconstruction was performed in two ways: 1) a simple deconvolution, by multiplying the k-space with the pseudo-inverse of M, as in equation 5; 2) minimization of Equation 6 with a non-linear conjugate gradient algorithm. Simulations were performed for a range of noise inputs, with zero mean and a standard deviation ranging from 0 to 20 a.u., (one-fifth of the maximum intensity of the two brighest ellipses), corresponding to the lowest SNR=5. For all simulated noise values, the mean intensity of the reconstructed images was tested in three regions-of-interest (ROI): i) a ROI in the PFOB phantom; ii) a ROI in the PFCE phantom; iii) a ROI in a noise-only region of the image.

Imaging

All imaging was performed on a 7T pre-clinical scanner (Bruker Biospec 70/30, Billerica, MA) using a dedicated $^{1}H/^{19}F$ volume coil with a 4 cm inner diameter (MR Coils, Zaltbommel, the Netherlands). The imaging frequency was centered on the PFCE peak in the MR spectrum before two or four sets of ^{19}F images were acquired using a 3D fast-low angle shot (FLASH) sequence. In the case of two readout directions, half of the data was acquired with readout direction left-to-right, while the other half was acquired with readout direction foot-to-head. In the case of four directions, additional right-to-left, and head-to-foot readouts were acquired.

Phantom ^{19}F MRI

Six 200 µL Eppendorf tubes with a mixture of pure PFOB/PFCE oils (Avanti lipids Alabaster, AL, USA) were prepared by linearly varying the relative volume in the mixtures in a total volume of 100 µL(0/100; 20/80; 40/60; 60/40; 80/20; 100/0 mL PFOB/mL PFCE respectively). These tubes were positioned in a circular phantom set up, also containing an Eppendorf tube filled with water for localization by ^{1}H imaging. Imaging was performed with the scan parameters reported in Table 1. The mean and standard deviation of the intensities in the six phantoms in an ROI covering the entire tube was calculated in the resulting images. Means and standard deviations were then normalized to the mean intensities of the pure compounds.

In vivo ^{19}F MRI

All experiments were performed in accordance with protocols approved by the Mount Sinai Animal Care and Utilization Committee.

Synthesis of the PFOB- and PFCE-containing nanoemulsions

Materials:

PFOB, PFCE, DMPC (1,2-dimyristoyl-sn-glycero-3-phosphocholine), and DPSE-PEG_{2000} (1,2-distearoyl-sn-glycero-3-phosphoethanolamine-N-[methoxy(polyethyleneglycol)-2000]) were obtained from Avanti lipids (Alabaster, AL, USA), chloroform was obtained from Sigma Aldrich (St Louis, MO, USA), and PBS from Gibco (Grand Island, NY, USA). Vivaspin (20 mL variant) centrifugal filters were purchased from Sartorius (Göttingen, Germany). Dynamic light scattering measurements were performed on a ZetaPals analyzer (Brookhaven Instrument corp., Holtsville, NY). Sonication was performed using a 150 V/T ultrasonic homogenizer working at 30% power output.

Experimental procedure:
Nanoemulsions were made by dissolving 1,2-dimyristoyl-sn-glycero-3-phosphocholine (DMPC; 36.17 mg, 53.4 μmol) and 1,2-distearoyl-sn-glycero-3-phosphoethanolamine-N-[amino(polyethyleneglycol)-2000] (DPSE-PEG_{2000}; 63.8 mg, 22.86 μmol) in chloroform (~2 mL) and slowly dripping this in PBS (10 mL) at 80 °C under vigorous stirring. After all chloroform was added, the viscous solution was allowed to cool to room temperature and additional PBS added to compensate for evaporation. The lipid solution (1 mL) was combined with PBS (9 mL) in a Falcon tube (15 mL), and either (PFOB or PFCE (320 μL) added. This solution was subsequently sonicated using a tip sonicator (30 minutes) while cooled in an ice bath. Large precipitates were removed by carefully decanting the solution. The particles were concentrated by centrifugal filtration (1 MDa molecular weight cut-off) to approximately 1 mL. Samples for dynamic light scattering measurements were prepared by diluting the nanoparticles with PBS. The mean of the number average size distribution was typically 160-180 nm.

	Phantom	**Mouse**			
		Intramuscular		Intravascular	
	^{19}F	^{19}F	^{1}H	^{19}F	^{1}H
Sequence	3D FLASH	3D FLASH	3D FLASH	3D FLASH	3D FLASH
Readout direction	FH, HF, LR, RL	FH & LR	FH	FH & LR	FH
Acquisition matrix	128x128x128	128x128x128	128x128x128	64x64x64	128x128x128
Field of view (mm^3)	40x40x40	40x40x40	40x40x40	40x40x40	40x40x40
TE (ms)	3.03	3.03	2.76	2.76	2.76
TR (ms)	20	20	20	20	20
Flip angle	35°	25°	25°	25°	25°
Excitation BW (Hz)	33000	33000	33000	33000	33000
Receiver BW (Hz)	44600	44600	44600	44600	44600
Number of Averages	4	6	2	24	4
Scan time	4x 21m51s	2x 32m46s	10m55s	2x 32m46s	10m55s

Table 1. Scan parameters.

Intramuscular injection

A male C57BL/6 mouse was injected with the PFCE nanoemulsion in the right upper leg and with the PFOB nanoemulsion in both left and right upper legs. The animal was anesthetized with 1.5% isoflurane. Subsequently, ^{1}H and ^{19}F MRI was performed using the parameters described in Table 1. After image reconstruction, the PFCE and PFOB images were color-coded and overlaid on the proton scan in Matlab.

Intravascular injection

Three male C57BL/6 mice were anesthetized with 1.5% isoflurane and underwent 3 longitudinal imaging sessions 24 hours apart, after intravenous injections of PFCE and PFOB containing nanoemulsions. At the beginning of each imaging session, ^{1}H images were acquired using a FLASH 3D sequence. Relevant scan parameters can be found in Table 1. Prior to the first imaging session, PFCE nanoemulsion (200 µL) was injected through a lateral tail vein. Twenty-four hours afterward, the mice were injected with PFOB nanoemulsion (200 µL) and immediately imaged using the same protocol. The third and final imaging session was performed 24 hours later (48 hours after PFCE nanoemulsion injection, and 24 hours after PFOB nanoemulsion injection). After image reconstruction, a coronal slice was chosen that contained both liver and spleen tissue. The liver and spleen were segmented and the mean image intensity was determined. The PFCE and PFOB images were colored and overlaid on the proton scan in Matlab.

Reconstruction and post-processing

Translation errors may occur when the PFCE resonance is not exactly centered at 0 ppm. Prior to spectral un-mixing, the images with different readout directions were three-dimensionally co-registered using Matlab's *imregister*, to quantify the translation mismatch. A regular step gradient descent algorithm was used for *imregister*, with a maximum number of iterations of 100, and a relaxation factor of 0.5. The translation error was subsequently corrected in k-space. All data in this manuscript were reconstructed with the conjugate gradient algorithm, using a value of λ=0.01 and 75 iterations. These reconstruction parameters were empirically selected for optimal SNR, while limiting oversmoothing. The peak heights in the convolution spectrum (Equation 7) were based on the relative amplitudes of a PFOB phantom scanned with the same sequence parameters. After reconstruction, ^{19}F images were color-coded and overlaid on proton images. Thresholding of the ^{19}F signal was performed by setting all signal below the noise level to zero. Reconstruction code and example data are available online at *https://github.com/amc-mri/19F-multicolor*.

5.4 Results

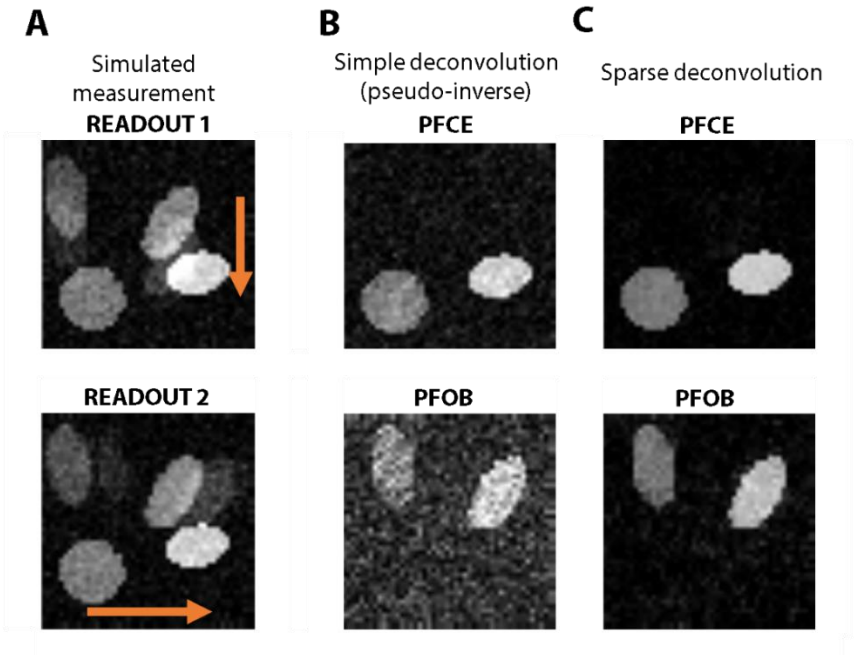

Figure 2. Simulation of PFOB and PFCE signal separation and chemical shift artifact removal. (A) Noisy acquisitions of 2 PFOB and 2 PFCE hot spots with readout in vertical and horizontal directions (orange arrows). The chemical shift artifacts from PFOB are apparent. (B) A pseudo-inverse reconstruction effectively separates the two compounds, but results in noise amplification. (C) Our sparse deconvolution method achieves excellent signal separation, while preserving signal-to-noise.

Numerical simulations

Numerical simulations were performed for an image containing two PFOB and two PFCE hot spots (Figure 2). The regular Fourier transform images for vertical and horizontal readout directions contain chemical shift artifacts for the PFOB (Figure 2A). Reconstruction was performed either as multiplication with the pseudo-inverse (Figure 2B) or by using the LASSO with a conjugate gradient (CG) (Figure 2C). Both methods successfully separated the two compounds and removed the chemical shift artifacts for PFOB. However, the pseudo-inverse reconstruction resulted in visually more noisy images as compared to CG reconstruction. Figure 3 presents the results for a simulation with a range of noise input images. Over the whole range of SNR values, the discrimination of the two compounds remained successful, there was no residual PFCE signal in the PFOB images since the signal at the location of the PFCE hot spots was equal to background signal. Similarly, no residual PFOB signal was observed in the PFCE images. For the CG method the background signal (noise)

essentially followed the nominal input SNR values. However, the pseudo-inverse method leads to significant noise amplification, particularly for the PFOB images.

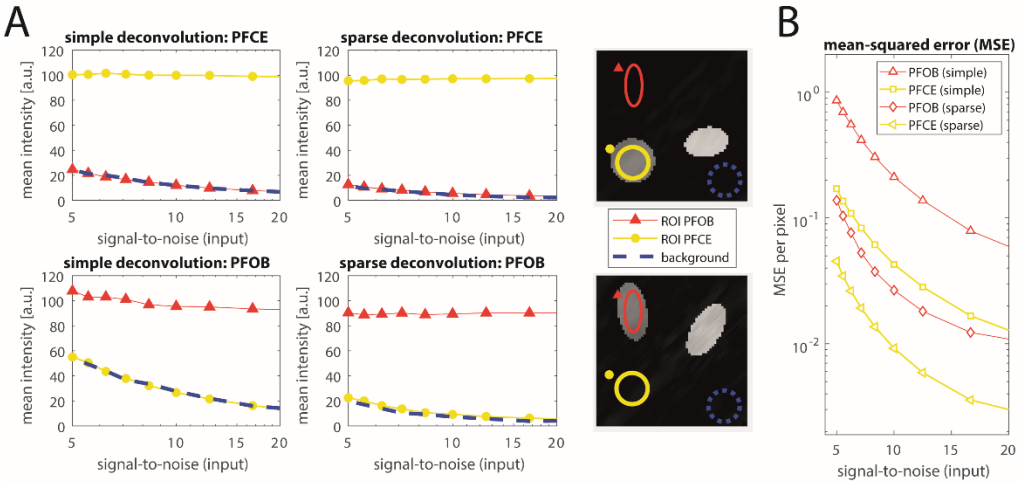

Figure 3. Simulated results for SNR levels between 5 and 20. A) Red triangles represent the mean signal in a ROI at the location of the PFOB phantom, yellow circles represent the mean signal in a ROI at the location of the PFCE phantom, whereas the blue dashed line indicates the mean signal intensity in noise ROI in the background. Both PFOB and PFCE mean signal intensities are relatively constant over the range of SNR values and both methods achieve good signal separation. There is no residual PFOB signal in the PFCE images (top two graphs), since the residual signal in the PFOB ROI (red triangles) is equal to the mean noise signal (blue dashed line). The same holds for residual PFCE in the PFOB image (bottom two graphs). However, noise levels with the new sparse-deconvolution method are much lower compared to simple pseudo-inverse reconstruction. B) Average mean squared-error per pixel for the separated PFOB and PFCE images. Error levels are much lower for sparse deconvolution than for simple deconvolution.

Phantom ^{19}F MRI

Figure 4A shows the linear Fourier transform reconstructions of the PFOB/PFCE mixture phantoms for the acquisitions with readout in 4 different directions. Our CG method successfully discriminated PFCE and PFOB in the different phantoms and removed the chemical shift artifacts (Figure 4B). The relative PFOB and PFCE signal intensities in the images were consistent with the mixture ratios (Figure 4C, D). The coefficients of variations (r^2) were 0.966 and 0.990 for PFOB and PFCE respectively.

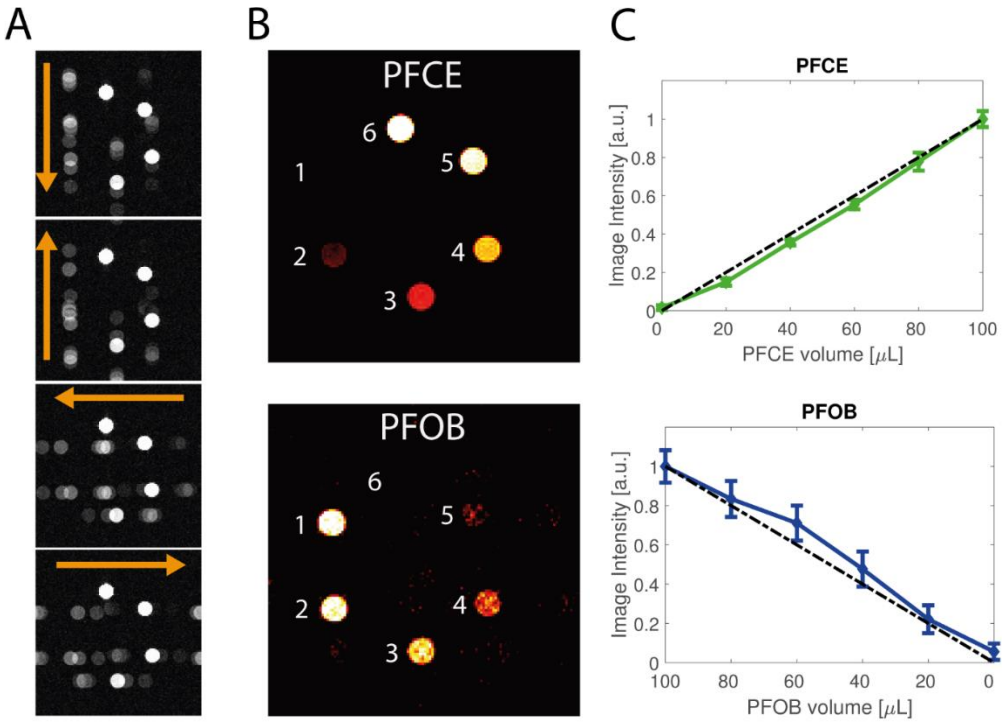

Figure 4. Phantom measurement of six Eppendorf tubes containing PFOB/PFCE with varying volume ratios. (A) **^{19}F**-MRI of the 6 phantoms with readout in 4 different directions (orange arrows). (B) Reconstructions of PFOB and PFCE signals. (C) Normalized mean signal intensities and standard deviation in the phantoms as function of PFCE and PFOB volume contributions. The dashed black line indicates a linear increase from 0 to 1. The coefficients of variation for PFOB and PFCE were r^2=0.966 and r^2=0.990, respectively.

Intramuscular injection

Figure 5 displays an axial, sagittal, and coronal slice, as well as magnifications, through the pockets of PFOB and PFCE nanoemulsions, which were injected in the mouse muscle. The ^{19}F images resulting from PFOB and PFCE are shown as green and red overlays on the ^{1}H MR images. Our CG method successfully removed the chemical shift artifacts from PFOB and separated the PFOB and PFCE signals. The pockets of nanoemulstions are also visible on the ^{1}H MR images as darker regions.

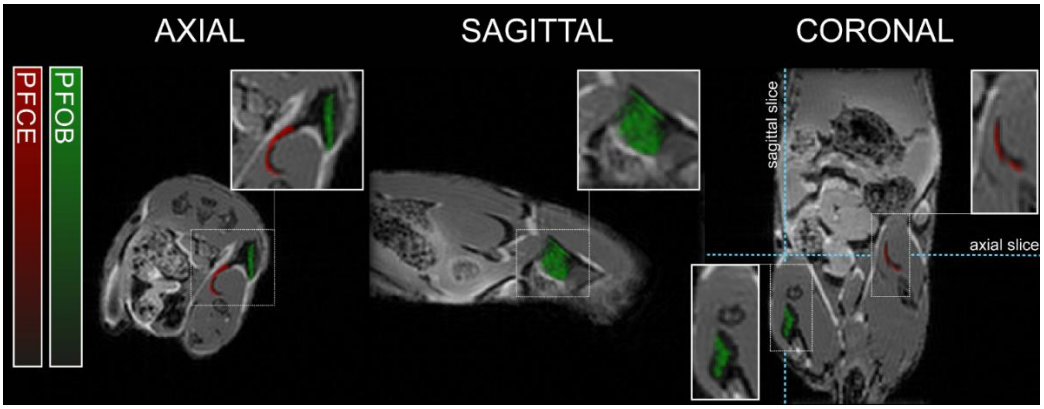

Figure 5. ^{19}F-MRI after intramuscular injections of PFOB and PFCE nanoemulsions. Reconstructed PFOB (green) and PFCE (red) signals (arbitrary units) are overlaid on the 1H-MRI anatomical image. PFOB was injected on both sides and PFCE in the right upper leg only.

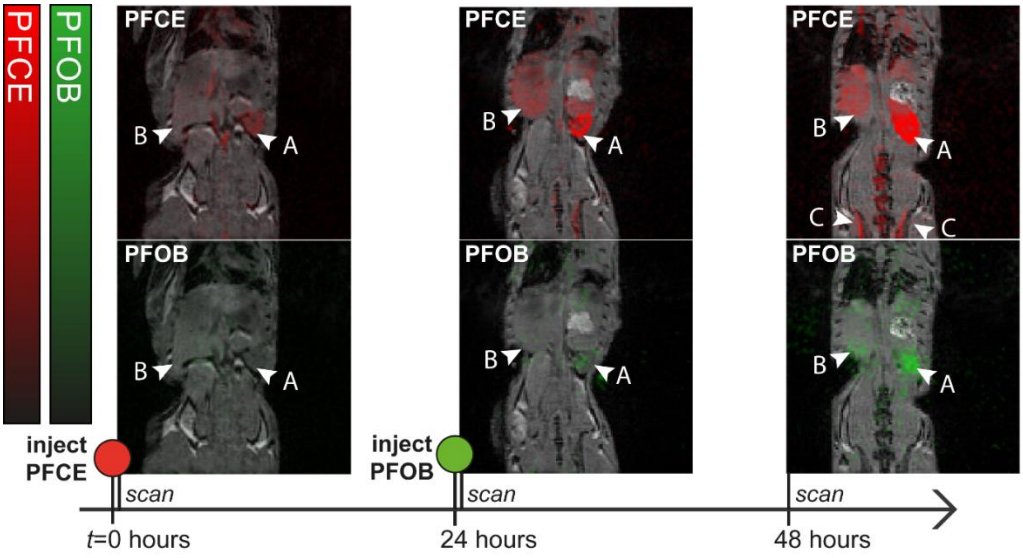

Figure 6. In vivo ^{19}F MRI of a mouse injected with PFCE nanoemulsion at t=0 hours and PFOB nanoemulsion at t=24 hours. PFOB and PFCE signal are reconstructed and overlaid on a **^{1}H**-MRI anatomical image. Color bars indicate PFOB (green) and PFCE (red) signal intensity in arbitrary units. The nanoemulsions accumulate mainly in the spleen (arrow head marked 'a') and to a lesser extent in liver (arrow head marked 'b'). At 48 hours accumulation in bone marrow (arrow heads marked 'c') is also observed.

Intravascular injection

Images of a representative mouse which received intravascular injections of PFCE and PFOB nanoemulsions are shown in Figure 6. Again, ^{19}F signal resulting from

PFOB and PFCE are shown as green and red overlays on ^{1}H MRI anatomical images. After injection, both PFCE and PFOB accumulated in liver and mainly spleen over time. PFCE was injected at day 0 prior to the first imaging session and PFOB emulsion one day later. Therefore, at day 0, only PFCE signal was observed, whereas PFOB appears at the 24-hour time point. At 48 hours, PFCE signal was also observed in the bone marrow in the spine and hip bones.

The mean ^{19}F PFOB and PFCE signal intensities of the spleen and liver of the three mice as function of time are plotted in Figure 7. The PFCE signal in both organs increased after the injection time, between day 0 and day 1, and remained relatively constant between day 1 and day 2. In contrast, the PFOB signal, which was injected 24 hours later, was not visible above the noise level at day 0 and increased between day 1 and day 2.

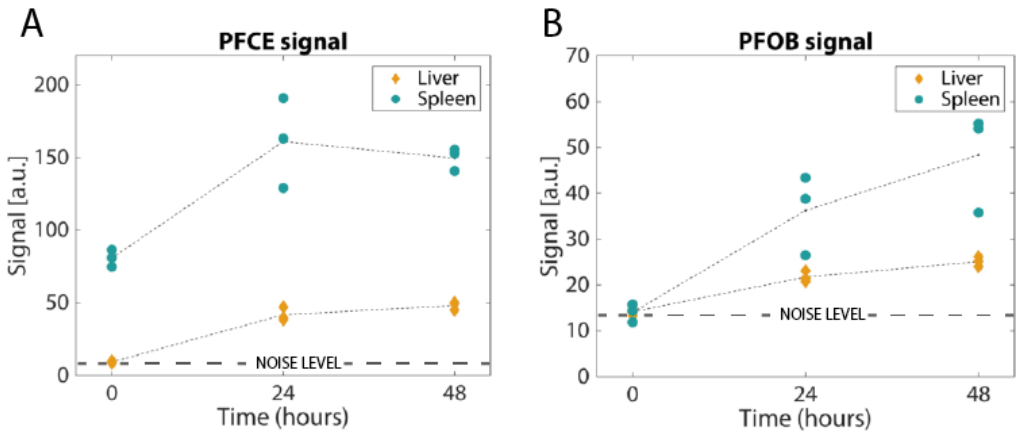

Figure 7. Mean image intensities in liver (yellow diamonds) and spleen (blue circles) of the three measured mice. Intensities are clustered closely together both in the PFCE (panel A) as in the PFOB images (panel B), for similar time points and organs. The increase in intensity over time corresponds to the IV injection times: PFOB image intensity increases overall between 24 to 48 hours, while PFCE intensity remains relatively constant between these time points.

5.5 Discussion

We have introduced a novel deconvolution approach for multicolor imaging of different ^{19}F compounds with complex spectra. Our method exploits the sparse nature of most ^{19}F images by iterative sparse deconvolution, removes the chemical shift artifacts associated with multiple peaks in the ^{19}F spectra, and efficiently separates multiple ^{19}F compounds in the images. We have also successfully applied this technique in in vivo small animal MR imaging.
We showed reliable separation and chemical shift artifact removal in numerical simulations. We found that, even for measurements with an SNR as low as 5, the separation of compounds was successful and signal intensities remained constant over SNR values ranging from 5 to 20, although background signal (noise) for the PFOB with the complex spectrum was consistently higher than for the single-peak PFCE. Nevertheless, this shows that the LASSO reconstruction algorithm, which enforces sparsity in the images, efficiently regularizes the reconstruction to avoid noise amplification while preserving relative signal intensity and separation. We can conclude that this method is robust at low SNRs and does not lead to noise amplification, which is important since ^{19}F-MRI is often signal deprived.

The phantom experiments (Figure 4) demonstrated that chemical shift artifacts are successfully removed and relative concentrations of PFOB and PFCE accurately determined. Relative signal intensities of both PFOB and PFCE scaled linearly with concentrations, although the standard deviation of the PFOB signal was somewhat higher than that of PFCE. This can be explained partly by lower signal of PFOB as compared to PFCE, due to differences in T1, T2 and ^{19}F atom concentration, but also by the higher residual background signal (noise-amplification [25]) associated with the reconstruction of the PFOB signal (Figure 3). The degree of noise amplification due to the deconvolution is controlled by the regularization parameter λ, and is a trade-off between denoising and over smoothing.

Intramuscular injections of PFOB and PFCE nanoemulsions were used to test the acquisition and reconstruction protocol in an in vivo setting. The pockets of PFOB and PFCE in the muscle could be readily identified and separated (Figure 5). The injection pockets were also seen on the anatomical T1-weighted proton images as signal voids. These signal voids co-localized well with the reconstructed PFOB and PFCE hot spots.

Finally, the applicability of our approach was put to the test in three mice which were intravenously injected with PFCE and PFOB nanoemulsions. These experiments indeed demonstrated that PFOB and PFCE nanoemulsion accumulations can be separately imaged, even when both compounds are present in the same organs.

Technical considerations

Although we require multiple acquisitions with different readout gradient directions, our multicolor ^{19}F-MRI experiment does not lead to increased acquisition times. Since ^{19}F-MRI generally involves the detection and localization of low concentrations of ^{19}F-containing compounds, many signal averages are required to achieve acceptable SNR. The measurements in different directions can therefore be distributed over the averages, ensuring that the total acquisition time remains the same as the normal sequence and the resulting image SNR is not affected. SNR can even be improved by an optimized sparse k-space sampling and compressed sensing reconstruction strategy [28]. Our approach can be applied with different sequences, e.g. gradient-echo or spin-echo, provided that the multiple ^{19}F resonances lead to predictable and non-identical point spread functions.

We have neglected phase in our deconvolution model, since no signal cancellations issues were noticed. Also, we think that the deconvolution method is robust to incidental phase-related signal cancellation because the method can rely on the 7 resonances in the PFOB spectrum. Although the introduction of phase would be possible, a magnitude approach was chosen since phase images are much more prone to artifacts resulting from global and local field inhomogeneities.

Our experiments started with carefully centering the PFCE resonance frequency, which resulted in minimal (and often absent) misalignment between different readout directions. Any misalignment was then corrected with an image-based registration algorithm. In case a simple registration fails, the registration can be included in the reconstruction algorithm in a so-called 'blind deconvolution method', which jointly optimizes the deconvolution spectrum as well as the images. In that case, misregistration between images is also included in the optimization.

Although the SNR efficiency of the FLASH sequence is not optimal compared to more SNR-efficient sequences like bSSFP, particularly when T1 and T2 are long, we believe our approach has distinct advantages that justify the use of the FLASH sequence. We collect all the signal from the different resonances in a single acquisition; the deconvolution has the effect of 'collapsing' the signal of all peaks into one. Moreover, the FLASH sequence is relatively robust to Bo and B1 inhomogeneities and movement, which is a big advantage for 3D mouse abdominal imaging. While a regular FLASH sequence may display the inhomogeneity artifacts, the relatively low matrix size in combination with an intermediate acquisition bandwidth limits pixel-shifts. In practice, shimming in the mouse was adequate and we did not encounter problems. Even in the case of the plastic Eppendorf phantoms, which are difficult to shim and can induce considerable B0 inhomogeneities, our technique performed well. B1 inhomogeneities will have the usual influence on flip-angle and signal intensity, but this will not influence the performance of the deconvolution method.

On the other hand, bSSFP is experimentally difficult at high magnetic fields in mouse, and artifacts in the hot spot ^{19}F images will be difficult to recognize. Moreover, bSSFP is not balanced for off-resonance PFOB peaks, adding complexity to the SNR behavior.
Previous work has demonstrated the possibility and usefulness of multicolor ^{19}F imaging. Compared to multicolor imaging with selective excitation [14], [15], our method does not require multiple scans or acquisition of multiple echoes. SNR is maximized because we collect all the signal from the different resonances in a single acquisition and distribute the different readout directions over the averages.
Chemical shift imaging has been proposed [17], [18], however this method suffers from long acquisition times due to the need for an additional phase-encoding dimension. Even accelerated CSI [19], [20] will ultimately be time-limited with excessively long scan times for high-resolution 3D imaging.

Chemical shift encoding [22], uses a Dixon-like approach to separate multiple PFC compounds and remove artefacts. This requires acquisition of multiple echoes with varying TE. However, our approach is sequence independent, and does not suffer from T2* effects.
The usage of a multiple-measurement model is closely related to the SENSE-like coil sensitivity-based decoupling [23]. Here we have demonstrated deconvolution with different readout directions, but if available, acquisition with multiple receive coils can also be included in the reconstruction model.
Future work will focus on comparing our method to other multicolor ^{19}F techniques. We have used a volume coil in this study, but the algorithm does not put constraints on coil type. Multi-coil arrays could further improve SNR.
This method of separating ^{19}F signal can be integrated into recently adapted compressed sensing techniques [20][30]. The here presented approach for multicolor ^{19}F-MRI is fully compatible with parallel imaging and k-space undersampling and future work will focus on this application. More recently, machine learning (ML) techniques have been used to remove ghosts in spectroscopy [31]. In a similar vein, ML methods could be developed for the purposes of multicolor ^{19}F-MRI artifact removal and denoising.
Our experiments were designed with either two or four different readout directions. While keeping the acquisition time the same, one can increase the number of readout directions and reduce the number of averages per direction. We think that it is beneficial to use more readout directions (with less averages) to mitigate direction-related imperfections due to translation, motion, or gradient imperfections. On the other hand, the SNR per readout should be high enough to distinguish the chemical-shifted ^{19}F resonances. The optimal number of directions therefore needs to be balanced with SNR, which could be a topic of future studies
We expect our methodology to find application in non-invasive readout of tissue immune cells composition. In mouse studies, ^{19}F multicolor MRI may replace

commonly used ex vivo immunological assays, such as flow cytometry, and facilitate longitudinal in vivo studies. The methods may be translated to clinical scanners in a straightforward way, since it requires merely a standard 3D FLASH sequence with different readout directions. Of course, the clinical system needs to be equipped with ^{19}F coils, ^{19}F send and receive capability, and multi-nuclear software. At 3T, the lower field strength will result in decreased detection sensitivity, which might be mitigated with improved sampling strategies. Also, the appropriate regulatory approval is required for the safe use of specific ^{19}F compounds in humans. If these conditions are met, we believe that our approach can be a valuable addition to ^{19}F-labeled cell tracking studies in humans.

5.6 Conclusion

We successfully implemented an iterative deconvolution method for multicolor ^{19}F-MRI that is applicable in all sequences exhibiting well-defined chemical shift artifacts. In phantoms as well as in mice in vivo reliable chemical shift artifact removal and separation of PFCE and PFOB compounds was achieved. Our technique efficiently discriminates different ^{19}F compounds and facilitates in vivo MRI localization and quantification of multiple ^{19}F compounds.

5.7 References

[1] E. T. Ahrens, R. Flores, H. Xu, and P. A. Morel, "In vivo imaging platform for tracking immunotherapeutic cells," Nat. Biotechnol., vol. 23, no. 8, pp. 983–987, 2005.

[2] M. Srinivas, A. Heerschap, E. T. Ahrens, C. G. Figdor, and I. J. M. de Vries, "19F MRI for quantitative in vivo cell tracking," Trends Biotechnol., vol. 28, no. 7, pp. 363–370, 2010.

[3] S. Temme, F. Bönner, J. Schrader, and U. Flögel, "19F magnetic resonance imaging of endogenous macrophages in inflammation," Wiley Interdiscip. Rev. Nanomedicine Nanobiotechnology, vol. 4, no. 3, pp. 329–343, 2012.

[4] J. Ruiz-cabello, P. Walczak, D. A. Kedziorek, and V. P. Chacko, "In Vivo 'Hot Spot' MR Imaging of Neural Stem Cells using Fluorinated Nanoparticles," Magn. Reson. Med., vol. 60, no. 6, pp. 1506–1511, 2009.

[5] J. Ruiz-Cabello, B. P. Barnett, P. A. Bottomley, and J. W. M. Bulte, "Fluorine (19F) MRS and MRI in biomedicine," NMR Biomed., vol. 24, no. 2, pp. 114–129, 2011.

[6] D. Yanagisawa et al., "In vivo detection of amyloid β deposition using 19F magnetic resonance imaging with a 19F-containing curcumin derivative in a mouse model of Alzheimer's disease," Neuroscience, vol. 184, no. 19, pp. 120–127, 2011.

[7] B. Ebner et al., "Early assessment of pulmonary inflammation by19F MRI in vivo," Circ. Cardiovasc. Imaging, vol. 3, no. 2, pp. 202–210, 2010.

[8] D. K. Kadayakkara, S. Ranganathan, W. Bin Young, and E. T. Ahrens, "Assaying macrophage activity in a murine model of inflammatory bowel disease using fluorine-19 MRI," Lab. Investig., vol. 92, no. 4, pp. 636–645, 2012.

[9] R. B. van Heeswijk et al., "Chemical shift encoding (CSE) for sensitive fluorine-19 MRI of perfluorocarbons with complex spectra," Magn. Reson. Med., vol. 79.5, pp. 2724–2730, 2018.

[10] Y. S. Freeman DM , Muller HH, Hurd RE, "Rapid 19F magnetic resonance imaging of perfluorooctyl bromide in vivo," Magn. Reson. Imaging, vol. 6.1, pp. 61–64, 1988.

[11] U. Nöth, L. J. E. Jäger, J. Lutz, and A. Haase, "Fast F-19-NMR Imaging in-Vivo Using Flash-Mri," Magn. Reson. Imaging, vol. 12, no. 1, pp. 149–153, 1994.

[12] C. Giraudeau et al., "A new paradigm for high-sensitivity 19F magnetic resonance imaging of perfluorooctylbromide," Magn. Reson. Med., vol. 63, no. 4, pp. 1119–1124, 2010.

[13] M. J. Goette, J. Keupp, J. Rahmer, G. M. Lanza, S. A. Wickline, and S. D. Caruthers, "Balanced UTE-SSFP for 19F MR imaging of complex spectra," Magn. Reson. Med., vol. 74, no. 2, pp. 537–543, 2015.

[14] J. W. M. Bulte, " Detecting Different Cell Populations Using Multispectral 19 F MRI ," Radiology, vol. 291, no. 2, pp. 358–359, 2019.

[15] K. C. Partlow et al., "19 F magnetic resonance imaging for stem/progenitor cell tracking with multiple unique perfluorocarbon nanobeacons," FASEB J., vol. 21, no. 8, pp. 1647–1654, 2007.

[16] C. Chirizzi, D. De Battista, I. Tirotta, and P. Metrangolo, "Multispectral MRI with Dual Fluorinated Probes to Track Mononuclear Cell Activity in Mice," Radiology, no. 20, pp. 1–7, 2019.

[17] C. Jacoby et al., "Probing different perfluorocarbons for in vivo inflammation imaging by19F MRI: Image reconstruction, biological half-lives and sensitivity," NMR Biomed., vol. 27, no. 3, pp. 261–271, 2014.

[18] T. C. Basse-Lüsebrink, G. Stoll, G. Weise, P. M. Jakob, C. Kleinschnitz, and T. Kampf, "In Vivo Imaging of Stepwise Vessel Occlusion in Cerebral Photothrombosis of Mice by 19F MRI," PLoS One, vol. 6, no. 12, p. e28143, 2011.

[19] M. Yildirim, J. Keupp, K. Nicolay, and R. Lamerichs, "Chemical shift independent imaging of 19F contrast agents using ultrafast MRSI (F-uTSI) M.," Proc. 15th Annu. Meet. ISMRM, p. 1249, 2007.

[20] T. Kampf et al., "Application of compressed sensing to in vivo 3D 19F CSI," J. Magn. Reson., vol. 207, no. 2, pp. 262–273, 2010.

[21] R. Pohmann, M. Von Kienlin, and A. Haase, "Theoretical Evaluation and Comparison of Fast Chemical Shift Imaging Methods," J. Magn. Reson., vol. 129, no. 2, pp. 145–160, 1997.

[22] K. D. Ludwig, D. Hernando, N. T. Roberts, R. B. van Heeswijk, and S. B. Fain, "A chemical shift encoding (CSE) approach for spectral selection in fluorine-19 MRI," Magn. Reson. Med., vol. 79, no. 4, pp. 2183–2189, 2018.

[23] O. Lips and J. Keupp, "Reduction of Chemical Shift Artifacts in 19F Imaging utilizing Coil Sensitivities O.," Proc. 16th Annu. Meet. ISMRM, p. 1738, 2008.

[24] L. J. Busse et al., "Deconvolution techniques for removing the effects of chemical shift in 19F nuclear magnetic resonance imaging of perfluorocarbon compounds.," Med. Phys., vol. 13, no. 4, pp. 518–24, 1986.

[25] H. K. Lee and O. Nalcioglu, "Reblurred deconvolution method for chemical shift removal in F-19 (PFOB) MR imaging.," J. Magn. Reson. Imaging, vol. 2.1, pp. 53–61, 1992.

[26] M. Meissner, M. Reisert, T. Hugger, J. Hennig, D. Von Elverfeldt, and J. Leupold, "Revealing signal from noisy 19F MR images by chemical shift artifact correction," Magn. Reson. Med., vol. 73, no. 6, pp. 2225–2233, 2015.

[27] M. Lustig, D. Donoho, and J. M. Pauly, "Sparse MRI: The application of compressed sensing for rapid MR imaging," Magn. Reson. Med., vol. 58, no. 650, pp. 1182–1195, 2007.

[28] E. Darçot et al., "Compressed Sensing with Signal Averaging Reduces Motion Artifacts in Fluorine-19 MRI," Proc. Int. Soc. Magn. Reson. Med., 2018.

[29] O. Yorulmaz, O. B. Demirel, T. Çukur, E. U. Saritas, and A. E. Çetin, "A Blind Deconvolution Technique Based on Projection Onto Convex Sets for Magnetic Particle Imaging," pp. 1–19, 2017.

[30] J. Zhong, P. H. Mills, T. K. Hitchens, and E. T. Ahrens, "Accelerated fluorine-19 MRI cell tracking using compressed sensing," Magn. Reson. Med., vol. 69, no. 6, pp. 1683–1690, 2013.

[31] S. P. Kyathanahally, A. Döring, and R. Kreis, "Deep learning approaches for detection and removal of ghosting artifacts in MR spectroscopy," Magn. Reson. Med., vol. 80, no. 3, pp. 851–863, 2018.

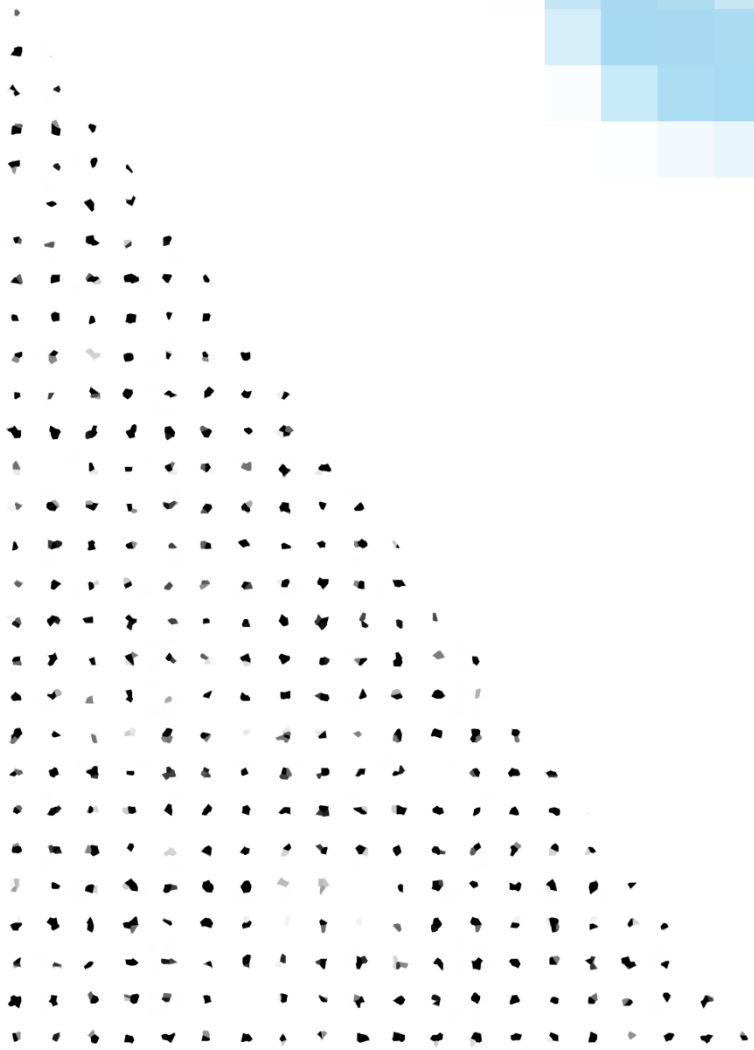

Chapter 6

Accelerated 4D self-gated MRI of tibiofemoral kinematics

Valentina Mazzoli*
Jasper Schoormans*
Martijn Froeling
Andre M. Sprengers
Bram F. Coolen
Nico Verdonschot
Gustav J. Strijkers
Aart J. Nederveen

* These authors contributed equally

Published in NMR in Biomedicine, 2017; 30(11):e3791

6.1 Abstract

Introduction: Anatomical (static) MRI is the most useful imaging technique for evaluation and assessment of internal derangement of the knee, but it does not provide dynamic information and does not allow to study the interaction of the different tissues during motion. Since knee pain is often only experienced during dynamic tasks, the ability to obtain four-dimensional (4D) images of the knee during motion could improve diagnosis and provide a deeper understanding of the knee joint. In this work, we present a novel approach for dynamic, high-resolution 4D imaging of the freely moving knee without a need for external triggering.
Methods: The dominant knee of 5 healthy volunteers was scanned during a flexion/extension task. To evaluate the effects of non-uniform motion and poor coordination skills on the quality of the reconstructed images, we performed a comparison between fully free movement and movement instructed by a visual cue. The trigger signal for self-gating was extracted using Principal Component Analysis (PCA), and the images were reconstructed using a parallel imaging and compressed sensing reconstruction pipeline. The reconstructed 4D movies were scored for image quality and used to derive bone kinematics through image registration.
Results: Using our method, we were able to obtain 4D high-resolution movies of the knee without the need for external triggering hardware. The movies obtained with and without instructions did not significantly differ in terms of image scoring and quantitative values for tibiofemoral kinematics.
Conclusions: Our method showed to be robust to extract self-gating signal even for uninstructed motion. This can make the technique suitable for patients that due to pain may find difficult to exactly comply with instructions. Furthermore, bone kinematics can be derived from accelerated MRI without the need for additional hardware for triggering.

6.2 Introduction

While anatomical MRI is the most commonly used imaging technique for evaluation and assessment of the knee joint, it does not provide dynamic information and therefore does not allow to study the interaction of the different tissues during motion tasks.

The normal mechanism of motion in the tibiofemoral joint depends on both static and dynamic factors. Dynamic interaction between the different tissues during motion plays a fundamental role in the stability of the knee joint. For instance, one of the main dynamic stabilizers of the patella is the quadriceps muscle group. Due to the fundamental role of the musculature in the biomechanical behavior of the patella, active quadriceps contraction is required to get a realistic assessment. This implies that a series of static images is not appropriate for describing the real kinematic behavior. The added value of dynamic imaging has been shown by d'Entremont et al.[1], who compared dynamically acquired MRI datasets with a series of static scans at different knee positions, and found significant differences in kinematic parameters. Furthermore, dynamic MRI of the musculoskeletal system could provide information beyond static imaging to understand the cause of pain. Pain is often absent in static conditions and only present during a specific movement, as it is often the case with impingements for example. The ability to perform this specific movement inside the MRI scanner could provide the radiologist with additional tools to understand the cause of pain and adapt treatment accordingly[2,3].

Fluoroscopy[4] has been proposed as a powerful method to study bone kinematics. Unlike MRI, it can provide bone kinematics under physiologically relevant loading conditions and during daily motion tasks. However, since it requires ionizing radiation, it is not an ideal candidate for longitudinal studies. Furthermore, fluoroscopy provides very limited soft tissue contrast, thus preventing the study of the interaction of the different soft tissue structures during motion.

MRI has been proposed as an alternative technique to assess tibiofemoral kinematic. Unlike fluoroscopy, it does not make use of ionizing radiation and allows for visualization of soft tissues such as cartilage and muscles. Draper et al.[5,6] have assessed patellar tilt in patellofemoral dislocation using single slice real-time MRI. While a real-time approach is desirable, it does not allow for volumetric imaging and thus does not provide 3-dimensional information. Joint motion can also be visualized by Phase Contrast (PC)-CINE (synchronized) techniques[7–9]. These methods rely on the acquisitions of a high-resolution static scans and 3 single-slice dynamic scans. While bone kinematics can be accurately determined using this approach, it is intrinsically unsuitable for 3D visualization of soft tissue motion. Furthermore, since PC techniques encode velocity, they require integration to obtain displacement, which is a procedure prone to error.

Kaiser et al. have developed a 4D MRI imaging technique to study tibiofemoral kinematic in healthy subjects[10]and patients after Anterior Cruciate Ligaments

reconstruction (ACL reconstruction)[11]. After ACL reconstruction altered kinematic parameters were measured in comparison to the contralateral healthy knee. Abnormal kinematic parameters are believed to induce abnormal cartilage loading patterns, which could be a primary cause of osteoarthritis. Therefore, there is great clinical interest in tools to quantify knee kinematic parameter. Kaiser et al. acquired data using a 3D radial k-space encoding scheme. During data acquisition, the knee angle was constantly externally monitored and this information was used for retrospective sorting of the images into a desired number of 3D frames[10].

3D radial methods offer highly incoherent sampling of k-space, which is highly beneficial for compressed sensing reconstruction, and it is inherently insensitive to motion artifacts within a given 3D time frame. However, eddy current related artifacts pose a challenge and the image reconstruction is a computationally expensive process.

Stack-of-stars is an alternative 3D MRI acquisition scheme that consists of a radial sampling pattern in the k_x – k_y plane, and a Cartesian encoding in the k_z direction. Like 3D radial sampling, it is robust to motion artifacts[12] and appropriate for undersampling and compressed sensing reconstruction. The stack-of-stars has some added benefits compared to 3D radial sampling: a reduced sampling time (pi/2 times fewer sampling points are required for a fully sampled image), and easier correction strategies for eddy currents effects[13]. Furthermore, the Cartesian stack direction enables different slices to be reconstructed in parallel, therefore greatly reducing computation times. In non-Cartesian imaging, each readout for the central slice encode passes through the center of k-space, thus facilitating retrospective self-gating [14]and eliminating the need for external sensors and/or navigators.

Radial trajectories can be acquired following a golden angle ordering scheme[15], where the angle between two consecutive radial spokes is increased by 111.246°. This approach allows to obtain an almost uniform coverage of k-space for each given number of consecutive spokes, which has the advantage of allowing continuous data acquisition and retrospective sorting of the spokes into several motion frames. The uniform distribution of the spokes using a golden angle ordering scheme allows for reconstruction of an almost arbitrary number of time frames, thus offering high flexibility in terms of temporal resolution.

For dynamic MRI studies, the knee motion can either be externally imposed, making it less suitable to assess contributions from active muscle contraction in the kinematics [1], or be based on visual/audio instructions, synchronized with an external TTL (transistor-transistor logic) trigger. The latter approach heavily relies on the perfect execution of the motion task, which becomes problematic if the subject is not able to comply with instructions due to poor coordination skills or pain. An alternative approach is the use of an external sensor to continuously monitor the position of the leg in the scanner[10]. However, this requires additional hardware which is not standard available with clinical MRI scanners.

In this study, we have developed a self-gated 4D stack-of-stars protocol to facilitate 4D imaging of the knee during uninstructed motion. We have performed measurements

in healthy volunteers during synchronized as well as free uninstructed movement of the knee, compared image quality, and quantified the derived tibiofemoral kinematics. In addition to dynamic bone imaging, we show feasibility for dynamic visualization of soft tissue structures in the knee.

6.2 Methods

Subjects

We collected images of the dominant knee of 5 healthy female volunteers (age 28±1 y/o, weight 61±6 kg, BMI=22±3 kg/m^2). None of the subjects had a history of knee injury or knee pain. We received informed consent from all the subjects prior to the study, according to our institution's regulations.

Knee motion

The subjects were placed supine on the scanner table, with a triangular-shaped support underneath their knee, and they were asked to perform a knee flexion/extension task. Two sand bags were placed laterally on each side of the knee, in order to prevent sliding and rotation of the knee during the motion task. Three different experiments were performed for each subject: in the first two experiments, the subjects were asked to flex and extend their knee for about 5 minutes at a frequency of 0.67 Hz. In order to improve the repeatability and consistency of the motion task, the subjects were shown a video of a ball bouncing up and down with the required frequency while inside the scanner, and asked to follow the movement of the ball ("with instructions"). Prior to the start of the experiments, subjects were instructed to always touch the support when in the mostly flexed position, and to extend their knees until the edge of the bore would be reached. Consequently, the amount of knee flexion was dependent on the size of the subject, but was kept relatively constant between different repetitions of the motion task for each subject. In order to simulate the effect of poor motor coordination skills on the results, a third experiment was performed without constraints on the frequency of the motion. For this experiment, no instruction was shown and the subjects were asked to move at their preferred pace ("without instructions"). For all experiments, the subjects flexed and extended their knees without any external weight.

Image acquisition

MRI was performed with a 3T Philips Ingenia scanner (Philips, Best, The Netherlands). All acquisitions were performed using a custom built 15 channel flexible coil array (MR Coils BV, Zaltbommel, The Netherlands). The coil array (3x5) was placed around the knee with Velcro straps and centered around the patella. The scan protocol consisted of 5 different datasets: 2 high-resolution anatomical datasets

to be used for segmentation, and 3 dynamic scans during the knee-movement tasks previously described.
The first high-resolution anatomical scan was a Turbo Spin Echo (TSE) scan with proton density contrast (TR=1000 ms and TE=29.9 ms, scan time=8 minutes). The second anatomical scan was a Fast Field Echo (FFE) with ProSet fat suppression (TR=10 ms, TE=4.5 ms, scan time 6 minutes). Both scans had 352x352x230 voxels of 0.68x0.68x0.7 mm^3.
The dynamic scans were obtained using a golden angle stack-of-stars sequence. A spoiled gradient echo sequence was used for data acquisition. Sequence parameters were: matrix size = 160x160x47, voxel size=1.5x1.5x3 mm^3, FOV=240x240x141 mm^3, TE/TR=1.3/3.9 ms. For Experiment 1 a flip angle of 20° was used, to obtain high SNR from the bones. For Experiment 2 the same imaging sequence was used, with a flip angle of 5° to enhance signal from collagen-rich structures such as ligaments and cartilage. For Experiment 3 (movement "without instructions") a flip angle of 20° was used. The acquisition was performed with 47 radial stacks with 1.3x slice oversampling. A zy ordering approach was used for the spoke acquisition, meaning that for each radial angle, spokes from all stacks were acquired before advancing to the next radial angle. A total of 1410 spokes was acquired for each stack, with a tiny golden angle increment of 20.89°. A tiny golden angle increment was used instead of 111.246° in order to reduce eddy current effects, which could lead to artifacts in the reconstructed images [16]. Data were continuously acquired during 5min20s of knee flexion/extension. All static and dynamic scans were acquired with readout in the sagittal orientation.

Image reconstruction

The main steps used in the reconstruction process are summarized in Figure 1. Raw scan data was exported and post-processed with MRecon (Gyrotools, Zürich) and Matlab (The Mathworks Inc.). We applied a coil channel compression routine, reducing the number of channels from 24 (15 ch flexible coil + 8 ch embedded in the scanner table + body coil) to 10 virtual channels[17]. Eddy current correction was performed offline[13,18]. An inverse FFT was applied along the fully sampled z-dimension, resulting in a set of 2D k-spaces which could be reconstructed in parallel[14].
The synchronization signal required for self-gating was derived from the center of k-space after FFT transform in the z-dimension. A principal component analysis (PCA) was calculated on the data matrix from the k-space center of the middle three slices of 10 channels (columns) and 1410 spokes (rows). The matrix on which PCA was performed had size 30*1410, corresponding to 3 slices in 10 channels (rows) and1410 radial spokes (columns). All principal components were analyzed. We selected the principal components with the highest signal power in the frequency bands [0.6-0.75] Hz, and [0.45-0.9] Hz for the instructed and non-instructed motion respectively[14]. Next, the self-gating signal was filtered with a band-pass filter to suppress additional periodic signals not of interest (such as the rotational frequency in k-space). The

cutoff frequencies for the band-pass filter were the upper and lower values of the corresponding frequency bands.
Subsequently, a peak-finding algorithm was applied to the filtered self-gating signal to define a fixed time-point in each motion cycle. This was used to sort the measured spokes into 20 motion states, each with an equal number of k-space spokes. This resulted in 20 k-space frames containing 70 randomly angled spokes, which corresponds to an undersampling factor of 3.59 (with respect to a fully sampled radial acquisition).
A parallel-imaging compressed-sensing reconstruction was performed using the BART toolbox [DOI: https://github.com/mrirecon/bart/releases/tag/v0.3.01]. Relevant parameters were: total-variation L1-regularization 0.01 (temporal and three spatial dimensions) and 100 iterations. Reconstructions were performed in parallel for all slices. Dynamic sensitivity maps used for the reconstruction were estimated using the ESPIRiT method [19]. Sensitivity map estimation was performed for each dynamic frame independently, based on a sliding windows approach, in which the sensitivity map of frame m was constructed using k-lines from frame m-1, m, and m+1. The average reconstruction time for a dataset was 3 hours on a server with two Intel Xeon E5-2690 processors and 256GB RAM. The reconstruction resulted in a set of 20 3D images for each single flexion extension cycle.

Image scoring

The movies obtained with and without instructions (Experiment 1 and Experiment 3) were scored in a blinded fashion by two independent MSK MR imaging experts for sharpness, contrast, bone visibility, fluency of motion, and presence of artifacts. The scores were assigned on a scale from 0 to 3, where 0 was insufficient and 3 diagnostic quality. One-way ANCOVA was used to compare the scoring obtained for the movies with instructions and without instructions. The reviewer was set as a covariate and $p<0.05$ was considered to be significant

Image segmentation

The femur and the tibia of the 5 volunteers were segmented from the high resolution FFE scan using a semiautomatic algorithm based on region growing (ITK-snap[20]). The contours were manually adjusted where necessary using the high-resolution proton density weighted scan as an additional reference.

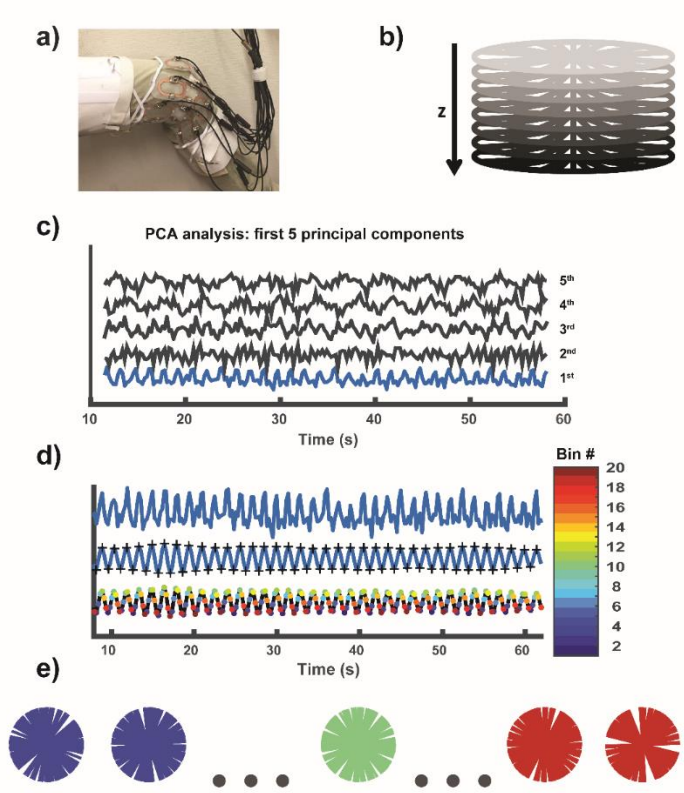

Figure 1. Schematic overview of the image acquisition and reconstruction pipeline. All images were acquired using a 15ch custom-built coil that could be wrapped around the subject's knee, offering high signal-to-noise ratio (SNR) without hindering the flexion/extension range of motion (Figure a). A stack-of-stars sampling scheme was used (Figure b). The 3 center stacks were used to determine the gating signal, based on Principal Component Analysis. The five first principal components are shown in Figure c, from bottom to top. The first component, depicted in blue, represents the knee motion frequency. This component is filtered (Figure d, middle row) and, after detection of minima and maxima, it is used to correctly assign each radial spoke to a given time bin (Figure d, bottom row). The 20 sorted k-spaces, which will be used to reconstruct 20 time frames, have an equal number of uniformly distributed spokes (Figure e).

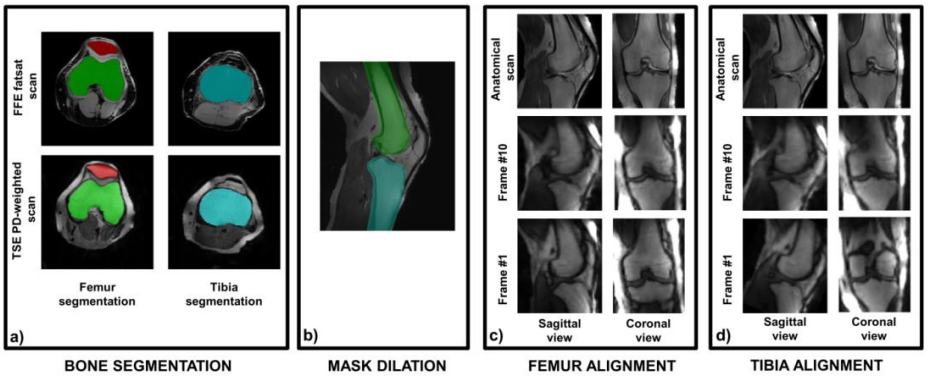

Figure 2. Image registration pipeline used to derive tibiofemoral kinematics from the reconstructed 4D images. a) 3D bone masks are segmented from the high-resolution anatomical scans. b) Bone masks are slightly dilated, in order to contain the interface between bones and other tissues (muscle and fat). c) A rigid registration is performed with constraints on the femur, using the anatomical proton density weighted scan as target. The result is a series of dynamic scans in which the femur is fixed. d) A second rigid registration step is performed with constraints on the tibia. The first time frame of the previously determined dataset with fixed femur was used as registration target. The result is a series of dynamic scans in which the tibia is fixed. The registration parameters of the last registration steps represent the tibiofemoral kinematics (three rotations and three translations).

Determination of bone kinematics

After image reconstruction, a 3D registration pipeline was applied on the datasets obtained from Experiment 1 and Experiment 3 to determine the bone kinematics. The main registration steps are summarized in Figure 2. We used a rigid registration pipeline implemented in Elastix[21], with 500 iteration steps and 2 levels of resolution. First, the segmented bone masks were convolved with a Gaussian kernel, and then dilated by a 3x3x3 cubic voxel to increase their volume. The dilation of the masks was needed in order to include the interface between the bone and the adjacent tissues into the registration target, which is the primary feature that drives the registration of the dynamic datasets. Subsequently, the dynamic datasets were reformatted to an isotropic resolution of 1.5x1.5x1.5 mm^3. The femur in the first dynamic frame was registered to the femur in the proton density weighted scans. The registered frame was used as a registration target for the subsequent 19 dynamic frames over the motion cycle. The results of this registration steps were 20 time frames with a static femur, and a moving tibia. An automated selection routine based on minimum detection of the femur translation curve was applied on this dataset to define the first time frame in a consistent way across the volunteers. This corresponded to the knee in full flexion. After femur registration, the same pipeline was repeated for the tibia, using the images with the registered femur as target.

The final result was a set of rigid-body trajectories (3 rotations and 3 translations) of the tibia with respect to the femur over the full motion cycle (20 dynamic frames). For each volunteer, the center of rotation was defined in the center of mass of the high-

resolution anatomical scan used for segmentation and the axis parallel to the axis of the image. The angles presented refer to the roll pitch and yaw convention, with rotations performed in the order roll, yaw and pitch. All kinematic trajectories were subsequently smoothed using a Gaussian filter with a smoothing factor of 2. Differences between the peak kinematics values measured at time frame #10 (where peak flexion occurred in all the subjects), with and without instructions, were statistically evaluated using a paired t-test, where $p<0.05$ was considered to be significant.

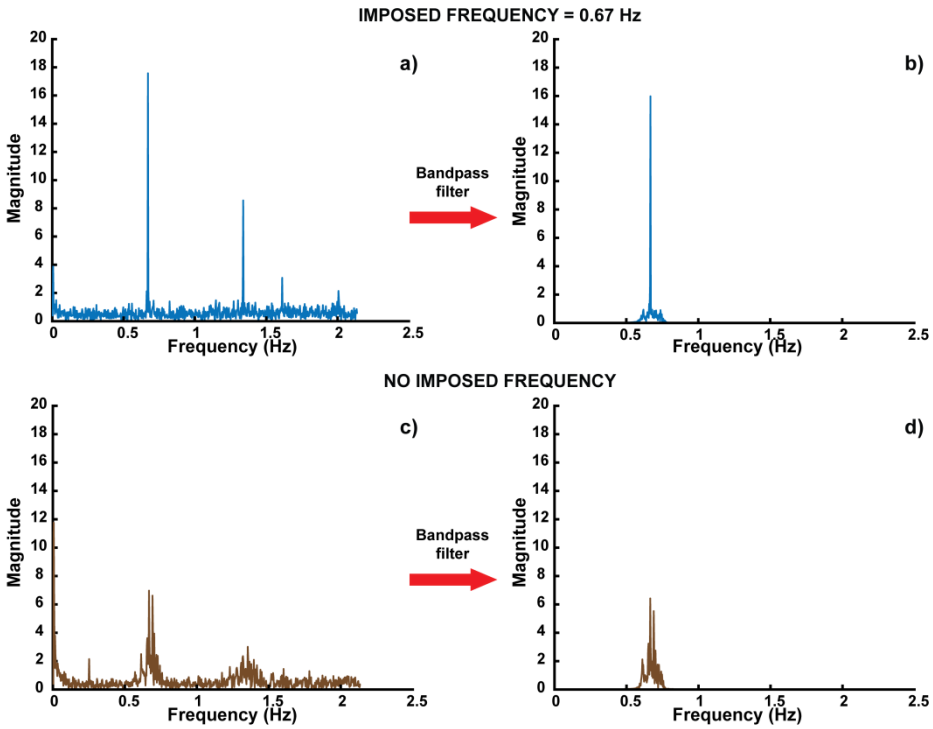

Figure 3. First principal component for one volunteer before (figure a) and after filtering with a bandpass filter (figure b). The main peak corresponds to the frequency of the visual cue (0.67 Hz). When no visual cue is provided, a typical broadening of the motion peak is observed (Figure c and d, before and after filtering respectively). The Fourier transform of the filtered spectra, shown in Figure b and d, are used as self-gating signal.

6.4 Results

All volunteers were able to perform the motion task very consistently when instructed via a visual cue, which is illustrated by a narrow peak in the frequency spectrum of the self-gating signal (**Figure 3a** and **4a**). The typical spectra derived from the first principal component for instructed motion are shown in **Figure 3a** (before filtering) and **Figure 3b** (after the application of a band pass filter) for one of the volunteers.

On the other hand, for uninstructed motion a worse repeatability of the motion task is observed in the same volunteer, as indicated by the broadening of the motion peak in **Figure 3c** (before filtering) and **Figure 3d** (after the application of a band pass filter). **Figure 4a** and **Figure 4b** show the mean self-gating signal averaged over the 5 volunteers. The agreement between the visual cue frequency and the self-gating frequency spectra of all volunteers (**Figure 4a**) indicates a credible self-gating signal. Without visual cue the peak of the motion frequency was different for the different volunteers (**Figure 4b**) and the peak broadened indicating a larger variability in motion during the ~5 min acquisition (**Figure 4b** and **Figure 4c**). However, in both cases, the self-gating approach with PCA analysis allowed for a correct assignment of the motion states resulting in 3D movie frames of high quality without significant motion-related blurring and artifacts (**Figure 5**). There was no significant difference in the expert image scores for the movies reconstructed from the instructed and uninstructed acquisitions (**Table 1**).

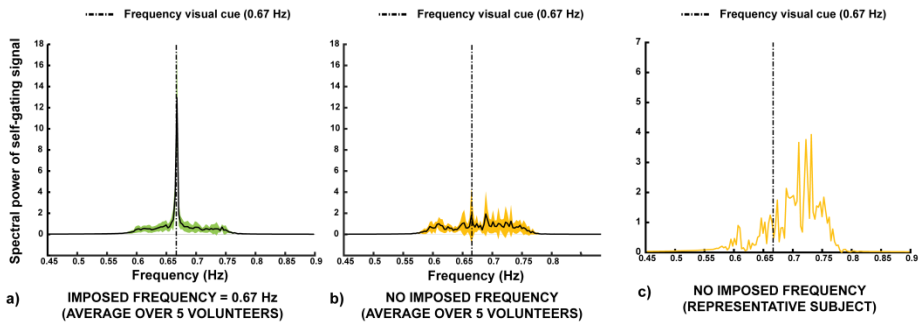

Figure 4. Mean self-gating signal, averaged over the 5 volunteers when instructions were given using a visual cue (Figure a) and when the motion task was performed without instructions (Figure b). The frequency of the visual cue, corresponding to 0.67 Hz, is indicated as dotted line for reference in Figure a, b and c, although the visual cue was only used to acquire the data in Figure a. Figure c shows the representative motion spectrum for one of the volunteers. In this case the frequency peak appears to be broader and at average higher frequency, suggesting that the motion task performed without instruction could be a good way to simulate the motion task performed by an orthopedic patient.

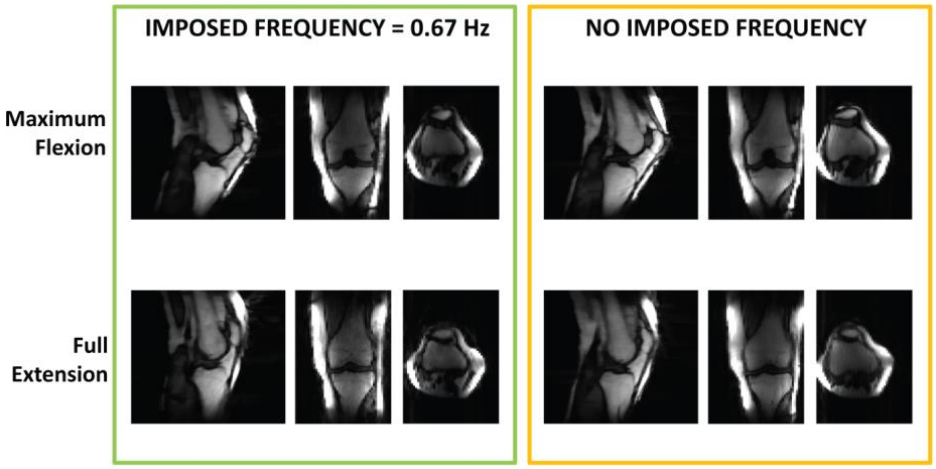

Figure 5. Two reconstructed dynamic frames (out of 20) representing the maximum achieved flexion and the full extension for a volunteer. Sagittal, coronal, and transverse views are presented. The left images were acquired when the subject was instructed to move at 0.67 Hz, while during the acquisition of the right images the subject was free to move at his own preferred pace. For both datasets the flip angle used was 20°.

The range of knee flexion achieved in the scanner by the subjects was 16.2°±1.7° (motion with instructions) and 14.5°±3.0° (motion without instructions) averaged ovm er the 5 subjects. The kinematic parameters representing tibiofemoral motion are presented in **Figure 6.** Taken together, the 3 rotational and 3 translational values and their variability, which describe the full range of possible tibiofemoral motions during knee flexion and extension, were similar for instructed and uninstructed tasks.

A small tibial external/internal rotation was measured for all subjects with increasing flexion angle. The peak tibial internal rotation across subjects was 3.4°±1.9° (motion with instructions) and 2.8°±2.6° (motion without instructions). Bigger inter-subject variation was detected for the translation degrees of freedom, as compared to rotations.

The mean values for each kinematic parameter was calculated at frame #10, which corresponds to the knee in maximum flexion. The results are presented in **Figure 7.** A paired t-test revealed no differences between the results obtained with and without instructions ($p>0.17$).

Using a low flip angle resulted in higher signal from collagen rich structures such as ligaments and cartilage. In **Figure 8,** two timeframes with the knee in maximum flexion and full extension respectively are shown. The Posterior Cruciate Ligament (PCL) presents high curvature in the extended position, and progressively gets more stretched as a function of increasing knee flexion angle.

Representative 4D movies obtained for a volunteer moving with and without instruction are presented as supplementary material (see **Video 1** and **2** respectively), together with the movie obtained with instructions and the low flip angle (**Video 3**).

Criteria	With instructions	Without instructions	p
Sharpness	2.2	2.1	0.721
Contrast	2.3	2.2	0.692
Bone visibility	2.2	2.3	0.703
Fluency of motion	3.0	2.9	0.331
Artifacts	2.0	1.9	0.668

Table 1. Results of scoring of the 4D movies by two musculoskeletal imaging experts. Scores are indicated on a scale from 0 to 3. No statistical difference (p>0.05) was observed in terms of sharpness, contrast, bone visibility, fluency of motion and presence of artifacts when the instructed frequency was 0.67 Hz ("*with instructions*") as compared to free movement ("*without instructions*").

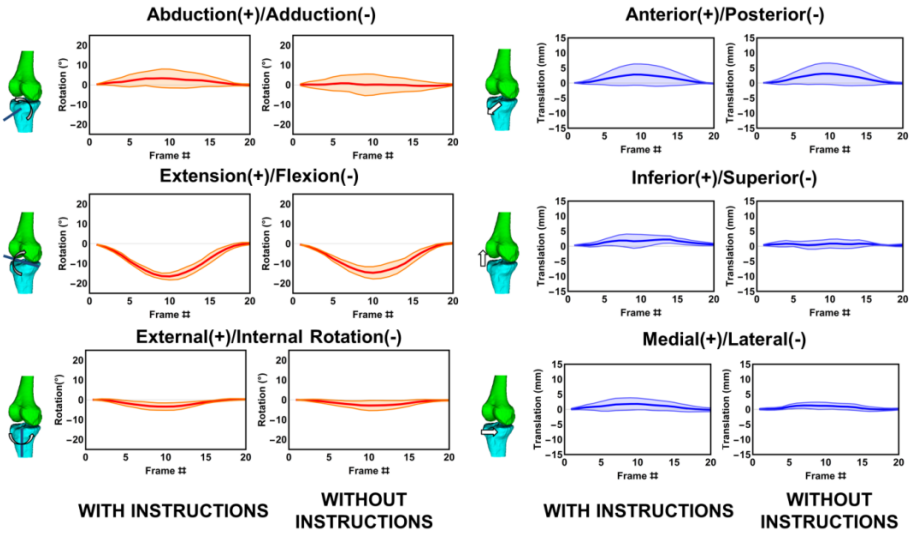

Figure 6: Tibiofemoral kinematics averaged over five healthy volunteers (shaded curves represent mean ± standard deviation) as a function of frame number. The three rotational degrees of freedom (abduction/adduction, extension/flexion and external/internal rotation) are indicated in red. The three translational degrees of freedom (posterior/anterior, superior/inferior and medial/lateral translation) are indicated in blue. Similar curves are observed when the instructed frequency was 0.67 Hz ("*with instructions*") as compared to free movement ("*without instructions*").

6.5 Discussion

The proposed golden angle radial sequence enabled acquisition of self-gating signals which were successfully used for binning the data in 20 time-frames over the flexion/extension cycle of the knee. We tested the sequence in 5 female volunteers, which were instructed to keep a constant frequency of 0.67 Hz during motion. Additionally, the volunteers were also asked to perform flexion extension without any visual instruction. We found no statistically significant differences in image quality scores between the two methods. Furthermore, we obtained similar results in terms of tibiofemoral kinematics extracted from the movies with and without instructions.
Self-gated MRI is gaining popularity for cardiac imaging [22,23] as well as in abdominal imaging [24,25] to estimate motion in relation to radiotherapy treatment planning. The self-gating approach is very attractive since it allows binning of the data in several motion states based on the k-space itself without relying on external triggering devices. Since the binning is done retrospectively, the number of movie frames and the data undersampling factor can be chosen after data acquisition.
A higher number of movie frames with increased data undersampling generally leads to lower SNR and more image artifacts, such as streaking. However, these artifacts can be reduced by compressed sensing image reconstruction[14,26]. In practice, a compromise has to be reached between temporal resolution and presence of image reconstruction artifacts, since a low number of movies frames will result in motion blurring, and a high number of movie frames will lead to undersampling artifacts even with compressed sensing reconstruction. We heuristically found that 20 frames over the flexion/extension cycle was the optimal trade off.

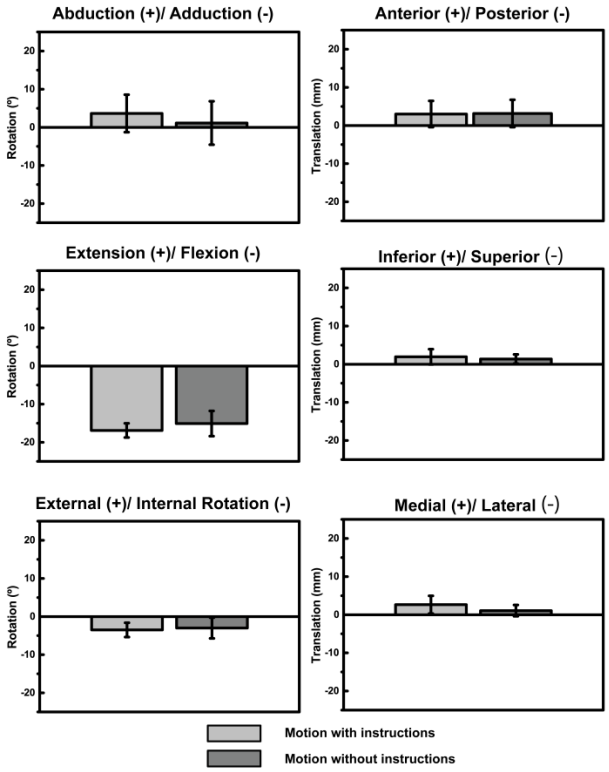

Figure 7. Bar graphs representing the tibiofemoral kinematics in the middle time frame (#10). Results are averaged over the five volunteers and the bars indicate standard deviation. No statistically significant differences observed between the peak kinematics parameters obtained with (light gray) and without instructions (dark gray).

It should be understood that with our technique the motion is not depicted in real time, but rather averaged over several motion cycles. This is not a limitation specific to our particular approach, but rather inherently related to the fact that 3D MRI with sufficient spatial resolution is too slow for real-time imaging even with state-of-the-art acceleration techniques. For the practical application of dynamic knee imaging, this implies that sudden movements such as dislocations cannot be visualized using a gated method. A real-time method[27] would then be required, but this is currently limited to single slice imaging.

Using our imaging method, in combination with novel image registration techniques, we were able to quantify the displacement of the tibia relative to the femur. The current gold standard for determination of bone kinematics is biplane fluoroscopy. This technique allows to acquire functional information during physiologically relevant task such as stair rising[4] and gait[28], with very high temporal and spatial resolution. However, fluoroscopy involves the use of ionizing radiation, which makes its use unpractical for longitudinal studies, and requires highly specialized machines which are not largely available in clinical settings. On the other hand, MRI scanners are present in virtually every hospital and routinely used for evaluation of the knee joint.

Since we used a closed-bore scanner, we had to deal with a limited range of motion of the knee joint due to geometrical constrains. This limitation could be solved with the use of an open-bore[29] or a vertical MRI system[5], although at the expense of temporal and spatial resolution related to the typically lower field strength of these systems.

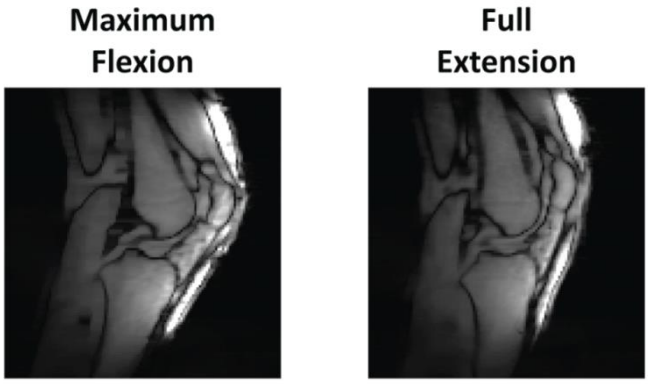

Figure 8. Two different reconstructed dynamic frames (out of 20) representing the maximum achieved flexion and the full extension for a volunteer during instructed motion at a frequency of 0.67 Hz. The flip angle used in the acquisition was 5º. The increasing stretching pattern of the PCL for increasing flexion angle of the knee can be observed.

Previous studies focused on determination of normative patellofemoral and tibiofemoral kinematics using Phase Contrast (PC) MRI[7,8]. PC-MRI relies on velocity measurements over time, which can be integrated to provide displacement measurements. The technique proposed by Rebmann et al. [8] is based on an unloaded flexion/extension task that is synchronized with an external trigger. Due to the need for acquiring velocity information along 3 orthogonal directions and the compliance of the subjects, the measurements are limited to 3 single slice acquisition of 2min48s each (through patella, through femur and through tibia). This technique heavily relies on the ability of the subject to keep a constant motion frequency, and small imperfections in the execution of the task can result in spatial and temporal blurring of the velocity values, that may lead to errors in the quantification of bone kinematics and even make the images unusable.

While bone motion can also be evaluated precisely and with higher frame rate using dynamic CT[30], the ability to simultaneously observe soft tissue and bone during motion makes our MRI-based approach unique. We were able to obtain images of the moving knee with relatively high resolution and sufficient soft tissue contrast, as indicated by the image scoring.

In this study, image scoring by experts was used instead of more conventional SNR and CNR measurements due to the use of compressed sensing reconstruction. In fact, when compressed sensing is used, high SNR can be obtained by simply increasing the regularization factor, without any corresponding increase in image quality or diagnostic information[31].

The images obtained with a low flip angle show high signal from ligaments and cartilage, potentially allowing the evaluation of these tissues during motion. The added values of dynamic imaging for soft tissue assessment in diagnosis still has to be systematically evaluated, and spatial resolution will likely have to be improved in order to increase the usefulness of these images. Nonetheless, the preliminary results presented in this study are a first step towards assessment of soft tissue motion in 3D.
In general, the lack of motion instructions results in a poorer repeatability of the task, as indicated by the lack of a well-defined frequency peak in this condition. Although this might result in incorrect sorting of the k-space spokes in bins, the expert quality scoring of the movies from the instructed and uninstructed tasks were similar, suggesting that sorting was robust to non-repetitive motion. While we believe that visual (or auditory) guidance to motion should always be provided for dynamic MRI study, conventional acquisition strategies based on prospective gating do not offer robustness against deviation from the given instructions. Many repetitions of the motion, especially under load, can lead to error in the executions of the task. Similarly, execution errors can be expected in orthopedic patients or subjects that due to pain may find it difficult to comply with instructions. Therefore, our self-gating method based on PCA and phase binning could be a useful tool for evaluation of those subjects, especially during long and/or loaded acquisitions.
All our acquisitions were obtained using a custom flexible knee coil, consisting of a 3x5 ch coil array. While the coil did add benefits in terms of SNR and image quality, our imaging pipeline is not hardware dependent and can be easily generalized to other anatomies (suck as wrist and ankle) and to other coil configurations.
Our self-gating signal was extracted from the three center slices of k-space. Other methods exist (i.e. ZIP[32]). However, for our application and slice orientation, they proved unreliable. We performed phase binning, instead of magnitude binning often used in respiratory motion[33]. In our experiments the volunteers were instructed to maintain a fixed start and end points for the flexion extension task. In this case an almost fixed magnitude of the motion was expected, but significant variation in the frequency could occur. Therefore, phase binning could be used more robustly than magnitude binning.
A general limitation of self-gating methods is that there is no absolute time stamp that indicates beginning and end of the flexion and extension cycle. For image scoring by the experts this was no problem, since movies were visualized in an infinite loop. However, quantification of the bone kinematics analysis requires knowledge about the time frame of maximum flexion and extension. Here we determined these time points by automatic detection of the minimum in the translation curve after the registration of femur, and this represented the maximum achievable extension. The starting point was chosen to be the full extension position, since the bone position was relatively constant for all volunteers in full extensions, while the maximum flexion position was largely dependent on the size of the subjects.
An additional limitation of our self-gating method is that it fails to determine the motion frequency when too much net translation of the knee occurs in the

mediolateral direction. In our study, the problem was mitigated by placing sand bags on each side of the knee. In order to completely avoid this problem, a motion device should be designed that restricts the range of motion in the mediolateral direction, while allowing full range of motion in the sagittal plane. Furthermore, a loading device could also increase the physiological values of the kinematic measurements, as compared to the "no-load" condition applied in this study.
We did not define an anatomical frame of reference based on the tibia and the femur at this point. Therefore our kinematic results cannot be directly compared previous studies[7,8]. The determination of an anatomical frame of reference based on bony landmarks could introduce additional inter-subject variation[34]. Therefore, for the purpose of this study, we preferred a direct comparison of the derived motions from the datasets obtained with and without instructions. Using our imaging methodology, we were able to obtain 4D images of the moving knee with relatively high resolution and sufficient soft tissue contrast, as indicated by the image scoring. Compressed sensing allowed for high undersampling factor (3.59-fold). The achieved scan time allows application of the technique as an addition to standard clinical protocols.
In conclusion, we have implemented a method to obtain self-gated 4D images of the moving knee using a golden angle radial sampling of k-space. Using a stack-of-stars sampling scheme we were able to derive the trigger signal directly from the data itself, without the need of any external monitoring device. Furthermore, we showed that high-resolution anatomical scans could be co-registered with the dynamic images to provide measurements of bone kinematics. Due to its simplicity, the method shows potential in evaluation of knee structures during motion and to track in vivo skeletal kinematics non-invasively in a clinical setting.

6.6 Supplemental material

Video 1: Sagittal slice for a volunteer moving with instructions (frequency of motion = 0.67 Hz, flip angle = 20°).
Video 2: Sagittal slice for a volunteer moving without instructions (flip angle = 20°).
Video 3: Sagittal slice for a volunteer moving with instructions (frequency of motion = 0.67 Hz, flip angle = 5°).

6.7 References

[1] D'Entremont AG, Nordmeyer-Massner JA, Bos C, Wilson DR, Pruessmann KP. Do dynamic-based MR knee kinematics methods produce the same results as static methods? *Magn Reson Med*. 2013;69(6):1634-1644.

[2] Gold GE. Dynamic and functional imaging of the musculoskeletal system. *Semin Musculoskelet Radiol*. 2003;7(4):245-248.

[3] Shapiro LM, Gold GE. MRI of weight bearing and movement. *Osteoarthr Cartil*. 2012;20(2):69-78.

[4] Akbarshahi M, Fernandez JW, Schache AG, Pandy MG. Subject-specific evaluation of patellofemoral joint biomechanics during functional activity. *Med Eng Phys*. 2014;36(9):1122-1133.

[5] Draper CE, Besier TF, Santos JM, Jennings F, Fredericson M, Gold GE, Beaupre GS, Delp SL. Using real-time MRI to quantify altered joint kinematics in subjects with patellofemoral pain and to evaluate the effects of a patellar brace or sleeve on joint motion. *J Orthop Res*. 2009;27(5):571-577.

[6] Draper CE, Besier TF, Fredericson M, Santos JM, Beaupre GS, Delp SL, Gold GE. Differences in patellofemoral kinematics between weight-bearing and non-weight-bearing conditions in patients with patellofemoral pain. *J Orthop Res*. 2011;29(3):312-317.

[7] Seisler AR, Sheehan FT. Normative three-dimensional patellofemoral and tibiofemoral kinematics: A dynamic, in vivo study. *IEEE Trans Biomed Eng*. 2007;54(7):1333-1341.

[8] Rebmann AJ, Sheehan FT. Precise 3D skeletal kinematics using fast phase contrast magnetic resonance imaging. *J Magn Reson Imaging*. 2003;17(2):206-213.

[9] Westphal CJ, Schmitz A, Reeder SB, Thelen DG. Load-dependent variations in knee kinematics measured with dynamic MRI. *J Biomech*. 2013;46(12):2045-2052.

[10] Kaiser J, Bradford R, Johnson K, Wieben O, Thelen DG. Measurement of tibiofemoral kinematics using highly accelerated 3D radial sampling. *Magn Reson Med*. 2013;69(5):1310-1316.

[11] Kaiser J, Vignos MF, Liu F, Kijowski R, Thelen DG. American Society of Biomechanics Clinical Biomechanics Award 2015: MRI Assessments of Cartilage Mechanics, Morphology and Composition Following Reconstruction of the Anterior Cruciate Ligament. *Clin Biomech*. 2016;34:38-44.

[12] Glover GH, Pauly JM. Projection Reconstruction Techniques for Reduction of Motion Effects in MRI. *Magn Reson Med*. 1992;28(2):275-289.

[13] Buonincontri G, Methner C, Krieg T, Carpenter TA, Sawiak SJ. Trajectory correction for free-breathing radial cine MRI. *Magn Reson Imaging*. 2014;32(7):961-964.

[14] Feng L, Axel L, Chandarana H, Block KT, Sodickson DK, Otazo R. XD-GRASP: Golden-angle radial MRI with reconstruction of extra motion-state dimensions using compressed sensing. *Magn Reson Med*. 2016;75(2):775-788.

[15] Winkelmann S, Schaeffter T, Koehler T, Eggers H, Doessel O. An optimal radial profile order based on the golden ratio for time-resolved MRI. *IEEE Trans Med Imaging*. 2007;26(1):68-76.

[16] Wundrak S, Paul J, Ulrici J, Hell E, Rasche V. A small surrogate for the golden angle in time-resolved radial MRI based on generalized fibonacci sequences. *IEEE Trans Med Imaging*. 2015;34(6):1262-1269.

[17] Buehrer M, Pruessmann KP, Boesiger P, Kozerke S. Array compression for MRI with large coil arrays. *Magn Reson Med*. 2007;57(6):1131-1139.

[18] Moussavi A, Untenberger M, Uecker M, Frahm J. Correction of gradient-induced phase errors in radial MRI. *Magn Reson Med*. 2014;71(1):308-312.

[19] Uecker M, Lai P, Murphy MJ, Virtue P, Elad M, Pauly JM, Vasanawala SS, Lustig M. ESPIRiT - An eigenvalue approach to autocalibrating parallel MRI: Where SENSE meets GRAPPA. *Magn Reson Med*. 2014;71(3):990-1001.

[20] Yushkevich PA, Piven J, Hazlett HC, Smith RG, Ho S, Gee JC, Gerig G. User-guided 3D active contour segmentation of anatomical structures: Significantly improved efficiency and reliability. *Neuroimage*. 2006;31(3):1116-1128.

[21] Klein S, Staring M, Murphy K, Viergever MA, Pluim JPW. Elastix: A toolbox for intensity-based medical image registration. *IEEE Trans Med Imaging*. 2010;29(1):196-205.

[22] Motaal AG, Coolen BF, Abdurrachim D, Castro RM, Prompers JJ, Florack LMJ, Nicolay K, Strijkers GJ. Accelerated high-frame-rate mouse heart cine-MRI using compressed sensing reconstruction. *NMR Biomed*. 2013;26(4):451-457.

[23] Paul J, Divkovic E, Wundrak S, Bernhardt P, Rottbauer W, Neumann H, Rasche V. High-resolution respiratory self-gated golden angle cardiac MRI: Comparison of self-gating Methods in combination with

k-T SPARSE SENSE. *Magn Reson Med*. 2015;73(1):292-298.

[24] Deng Z, Pang J, Yang W, Yue Y, Sharif B, Tuli R, Li D, Fraass B, Fan Z. Four-dimensional MRI using three-dimensional radial sampling with respiratory self-gating to characterize temporal phase-resolved respiratory motion in the abdomen. *Magn Reson Med*. 2016;75(4):1574-1585.

[25] Cruz G, Atkinson D, Buerger C, Schaeffter T, Prieto C. Accelerated motion corrected three-dimensional abdominal MRI using total variation regularized SENSE reconstruction. *Magn Reson Med*. 2015;1498:1484-1498.

[26] Benkert T, Feng L, Sodickson DK, Chandarana H, Block KT. Free-Breathing Volumetric Fat/Water Separation by Combining Radial Sampling, Compressed Sensing, and Parallel Imaging. *Magn Reson Med*. 2016;576:565-576.

[27] Mazzoli V, Nederveen AJ, Oudeman J, Sprengers A, Nicolay K, Strijkers GJ, Verdonschot N. Water and fat separation in real-time MRI of joint movement with phase-sensitive bSSFP. *Magn Reson Med*. 2017;78(1):58-68.

[28] Guan S, Gray HA, Keynejad F, Pandy MG. Mobile biplane X-Ray imaging system for measuring 3D dynamic joint motion during overground gait. IEEE Trans Med Imaging. 2016;35(1):326-336.

[29] King AJ, Deng Q, Tyson R, Sharp JC, Matwiy J, Tomanek B, Dunn JF. In Vivo Open-Bore MRI Reveals Region- and Sub-Arc-Specific Lengthening of the Unloaded Human Posterior Cruciate Ligament. *PLoS One*. 2012;7(11):1-10.

[30] Carelsen B, Jonges R, Strackee SD, Maas M, Van Kemenade P, Grimbergen CA, Van Herk M, Streekstra GJ. Detection of in vivo dynamic 3-D motion patterns in the wrist joint. *IEEE Trans Biomed Eng*. 2009;56(4):1236-1244.

[31] Feng L, Benkert T, Block KT, Sodickson DK, Otazo R, Chandarana H. Compressed sensing for body MRI. *J Magn Reson Imaging*. 2017;45:966-987.

[32] Spincemaille P, Liu J, Nguyen T, Prince MR, Wang Y. Z intensity-weighted position self-respiratory gating method for free-breathing 3D cardiac CINE imaging. *Magn Reson Imaging*. 2011;29(6):861-868.

[33] Han F, Zhou Z, Cao M, Yang Y, Sheng K, Hu P. Respiratory motion-resolved, self-gated 4D-MRI using rotating cartesian k-space (ROCK). *Med Phys*. 2017;44(4):1359-1368.

[34] Morton NA, Maletsky LP, Pal S, Laz PJ. Effect of Variability in Anatomical Landmark Location on Knee Kinematic Description. *J Orthop Res*. 2007;9:1221-1230.

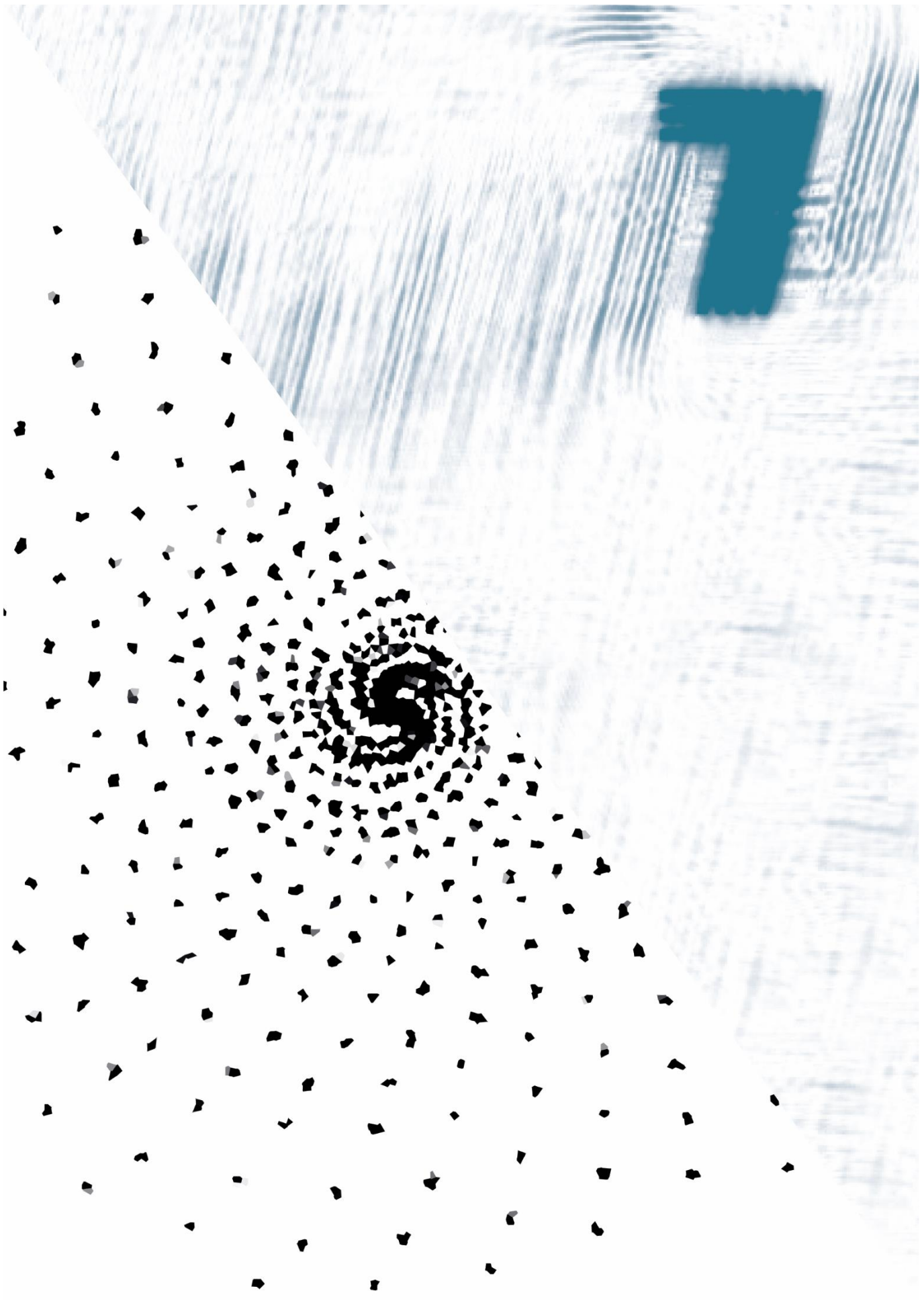

Chapter 7

General Discussion

Summary

Nederlandse Samenvatting

Research can take us on strange winding paths. Interesting (publishable) work is sometimes found while studying something else. Such was certainly the case for me. That is why this thesis covers so many different topics (anatomies, static, dynamic and quantitative imaging, and even pre-clinical work). However, the work shares a common theme in the application of *accelerated imaging* based on *sparsity*. From the broad range of applications in this thesis the question arises which technological advances are likely to change the way we will acquire clinical images in the future, and which won't.

Aims

Anatomical (static) MRI is the work-horse of imaging in most clinical settings. Parallel imaging (e.g. SENSE) has revolutionized scanning, and acceleration factors in the order of two to four times are routinely used in clinical practice these days. Compressed sensing is now well-established and understood and therefore it seems ready for clinical introduction [1]. Philips has introduced a product called *'Compressed SENSE'*, which successfully shortens scan times in anatomical imaging—up to 2 times compared to the standard parallel-MRI [2]. In terms of time gained, this compares rather poorly to the sexier dynamic and parametric acquisitions, for which acceleration factors in the double digits were reported [3].
So, anatomical MRI has less acceleration potential, and we are stuck with a minimum scan time? Maybe. But it might pay off to stop focusing solely on *acceleration* in accelerated imaging. In **Chapter 2**, we have investigated whether we could use the gained scan time for averaging, and, in a way, enable us make *better* images in low-SNR conditions rather than obtain them in less time. We found this to improve imaging in a certain low-SNR regime, and this could open up opportunities to obtain good quality images under low SNR conditions, deemed unfeasible before. In a similar way, some authors have proposed to use this novel insight to scan at greater resolution [4]. Lesson learned is that improving image quality with compressed sensing reconstruction techniques above standard parallel MRI is a goal worth pursuing.
Dynamic Contrast-Enhanced (DCE)-MRI is a widely used (in about 25% of examinations [5]) imaging technique. Most radiologists still prefer visual inspection of a limited set of images during contrast in- and efflux above a full quantitative contrast-dynamics analysis. A quantitative analysis of the full time-course of contrast in- and efflux, requiring a full dynamic movie, could potentially give more information on the tissue dynamics and thus give us more valuable diagnostic information to work with. In **Chapter 3** and **4**, we therefore developed a highly accelerated DCE protocol and measured various lesion-prone vascular regions (carotids, abdominal aorta, femoral arteries) in patients. New and essential to vascular imaging this protocol facilitated black-blood imaging with high spatial

resolution. A high spatial resolution, which is an absolute requirement for good delineation of vessel wall and plaque components, could only be obtained because of the *overcompleteness* of the anatomical information in the time domain. The temporal resolution in these scans was on the order of 10 seconds, whereas the total scan time—dictated by time it takes for contrast in- and efflux— was several minutes. In this example, we are thus not accelerating the examination time, but rather obtain more detailed spatio-temporal information in the same examination time.
A similar argument can be made for the work in **Chapter 6**. We were able to image the dynamics of tibiofemoral kinematics at unprecedented temporal resolution without the use of an external trigger. This could benefit the study of bone kinematics.
The question arises if we even want to call this collection of strategies *accelerated imaging*. That is not a bad thing. Speed is one factor but not a goal in itself. The true goal is to increase the diagnostic power of scans.
The promise of reduced waiting times and lower healthcare costs, usually laid at the feet of accelerated imaging, might therefore be more easily found in other aspects, e.g. more efficient patient preparation, and much wider clinical usage (educate technicians and start scanning patients in the evenings and the weekends!).

Technology

If we are interested in faster patient turnover times, image information of the entire exam should be combined. Multi-parametric approaches such as the low-rank-tensor framework [6], fingerprinting, MR-STAT [7], and joint sparsity over multiple contrasts [8], may allow for speeding up entire exams. These innovations are very exciting, as they are moving away from the simple prior knowledge of sparsity only – rather incorporating MR physics and data-driven compressibility into the reconstruction. The sparsity of images can be exploited to accelerate imaging, but might not be a great fit for all type of images—e.g. low SNR, or highly detailed images. However, multi-parametric approaches will only be helpful if these contrasts are clinically useful and provide complementary diagnostic information.

Specific tailoring

As the research in this thesis deals with a variety of contrasts, anatomies, and purposes, it is easy to see differences in what works for one approach and not for another. For example, in Chapter 2, for low SNR anatomical MRI, we used both total-variation and wavelet transform in our CS minimization. In the dynamic imaging chapters (3,4 & 6), only total-variation over time was used. In the preclinical work of Chapter 5, using ^{19}F data, which is very noisy, but also sparse by nature due to no background signal, total-variation could be used, but no transform works as well.

As with sparse transformation, many other 'buttons' can and should be tweaked to get optimal image quality. However, these are very specific to the intended use. For instance, we found our CS-VDA strategy of Chapter 2 to work very well—but only in a specific SNR and contrast regime.
The segmentation of very specific optimal settings for every use case needs to be addressed to achieve practical implementation of the collection of accelerated imaging techniques.

Implementation
Subtle differences in derivative measures might save lives. For example, knowledge on vessel wall permeability in atherosclerotic plaques may ultimately give insight into the vulnerability of plaques [9]. These permeability measures are derived from DCE-MRI. CS application has greatly improved image quality. However, ever-more complicated models are used. If the imaging was done right, the image reconstruction worked, the model was sufficiently explanatory of the biology, and all model input parameters have been measured or estimated correctly—only then the derived parameters are valuable. Error propagation is extremely tedious, and this is what will ultimately limit clinical application.
Image reconstruction times still represent a major hurdle. A big collection of optimization algorithms has been developed [10]. Many of which can now be run on state-of-the-art GPU clusters. However, the problems are generally ill-posed, with a huge possible solution space. As such, even the cleverest algorithms can take a few minutes to finish. For MR operators, which are used to receive reconstructed images in a few seconds, this is still too long.
Artificial Intelligence (AI) based learned reconstruction might be the solution—while training times are very long, a pre-trained model can be run in a fraction of a second. Many promising ideas have been proposed [11]–[13]. In contrast to sparsity-based accelerated imaging, AI methods do not generally have any prior, but learn image reconstruction purely based on training data. The recent *fast MRI Challenge* [14] gives an overview of the state of AI reconstruction. Many different approaches were tested and gave similar results, although comparisons with CS by neutral observers still seems to be lacking in literature. However, while optimization algorithms are generally proven to be robust—generally, the optimal solution will be found as long as you run it long enough—AI-based approaches are not [15]. Small disturbances in the data can have massive consequences on image quality. This should be a big priority for current research.

Community

We should recognize the importance of open-source software. The open-source Berkeley Advanced Reconstruction Toolbox [16] has seen a surge of users in the last few years. The ability for all researchers to look into and modify the source code is essential for fast, reproducible research. Similar approaches have been proposed for k-space data [17], and reconstruction frameworks [18]—however, the big vendors seem very slow and reluctant to join the open-source trend. This is very unfortunate: industry-wide open standards can speed up research and innovation for everyone. A big reason for the rapid innovation in the AI field is precisely the availability of the most state-of-the-art machine learning software to anyone.

Preventing code sharing by the vendors, combined with regular software changes, is very inefficient and makes researchers spend a big part of their time maintaining instead of innovating.

The MRI community is not very big, but it is quite well-connected. Novel papers and ideas quickly find their way around. However, cross-disciplinary knowledge transfer is more important than ever. Many ideas introduced in seminal papers were not new at all—merely cleverly applied and well marketed. I believe that very useful ideas will be found just by looking over the hedge. Of course, this will work the other way around as well, other (medical) imaging fields can benefit greatly from the research revolution in image reconstruction in the MRI field.

References

[1] S. S. Vasanawala, M. J. Murphy, M. T. Alley, P. L. K. Keutzer, and J. M. Pauly, "Practical parallel imaging compressed sensing MRI: Summary of two years of experience in accelerating body MRI of pediatric patients," in *2011 IEEE International Symposium on Biomedical Imaging: From Nano to Macro*, 2011, pp. 1039–1043.

[2] "MR Compressed SENSE | Philips Healthcare." [Online]. Available: https://www.philips.nl/healthcare/middelen/landing/the-next-mr-wave/compressed-sense. [Accessed: 13-Mar-2020].

[3] L. Feng, T. Benkert, K. T. Block, D. K. Sodickson, R. Otazo, and H. Chandarana, "Compressed sensing for body MRI," *J. Magn. Reson. Imaging*, vol. 45, no. 4, pp. 966–987, 2017.

[4] B. Roman, A. Hansen, and B. Adcock, "On asymptotic structure in compressed sensing," *arXiv Prepr. arXiv1406.4178*, no. c, pp. 1–10, 2014.

[5] J. Lohrke, T. Frenzel, J. Endrikat, F. Caseiro, T. M. Grist, M. Law, J. Min, L. Tim, K. L. Konstantin, N. Martin, H. H. Schild, J. C. Weinreb, K. Yoshikawa, and H. Pietsch, "25 Years of Contrast-Enhanced MRI : Developments , Current Challenges and Future Perspectives," *Adv. Ther.*, vol. 33, no. 1, pp. 1–28, 2016.

[6] J. He, Q. Liu, A. G. Christodoulou, C. Ma, F. Lam, and Z. P. Liang, "Accelerated High-Dimensional MR Imaging with Sparse Sampling Using Low-Rank Tensors," *IEEE Trans. Med. Imaging*, vol. 35, no. 9, pp. 2119–2129, 2016.

[7] O. Heide, A. Sbrizzi, P. R. Luijten, and C. A. T. Berg, "High-resolution in vivo MR-STAT using a matrix-free and parallelized reconstruction algorithm," *NMR Biomed.*, vol. 33, no. 4, Apr. 2020.

[8] J. Huang, C. Chen, and L. Axel, "Fast multi-contrast MRI reconstruction," *Magn. Reson. Imaging*, vol. 32, no. 10, pp. 1344–1352, Dec. 2014.

[9] B. F. Coolen, C. Calcagno, P. van Ooij, Z. A. Fayad, G. J. Strijkers, and A. J. Nederveen, "Vessel wall characterization using quantitative MRI: what's in a number?," *Magn. Reson. Mater. Physics, Biol. Med.*, pp. 1–22, 2017.

[10] J. A. Fessler, "Optimization methods for MR image reconstruction (long version)," *arXiv Prepr.*, vol. arXiv:1903, pp. 1–12, Mar. 2019.

[11] B. Zhu, J. Z. Liu, S. F. Cauley, B. R. Rosen, and M. S. Rosen, "Image reconstruction by domain-transform manifold learning," *Nature*, vol. 555, no. 7697, pp. 487–492, Mar. 2018.

[12] K. Hammernik, T. Klatzer, E. Kobler, M. P. Recht, D. K. Sodickson, T. Pock, and F. Knoll, "Learning a variational network for reconstruction of accelerated MRI data," *Magn. Reson. Med.*, vol. 79, no. 6, pp. 3055–3071, Jun. 2018.

[13] K. Lønning, P. Putzky, and M. Welling, "Recurrent Inference Machines for Accelerated MRI Reconstruction," *Int. Conf. Med. Imaging with Deep Learn.*, no. Midl 2018, pp. 1–11, 2018.

[14] F. Knoll, M. Rabbat, A. Defazio, J. Zbontar, M. J. Muckley, C. L. Zitnick, D. K. Sodickson, and M. P. Recht, "Advancing machine learning for MR image reconstruction with an open competition : Overview of the 2019 fastMRI challenge," pp. 1–18, 2019.

[15] V. Antun, F. Renna, C. Poon, B. Adcock, and A. C. Hansen, "On instabilities of deep learning in image reconstruction - Does AI come at a cost?," *Arxiv*, vol. 1902.05300, Feb. 2019.

[16] J. I. Tamir, F. Ong, J. Y. Cheng, M. Uecker, and M. Lustig, "Generalized magnetic resonance image reconstruction using the Berkeley Advanced Reconstruction Toolbox," *Proc. ISMRM 2016 Data Sampl. Image Reconstr. Work.*, vol. 2486, p. 9660006, 2016.

[17] S. J. Inati, J. D. Naegele, N. R. Zwart, V. Roopchansingh, M. J. Lizak, D. C. Hansen, C. Y. Liu, D. Atkinson, P. Kellman, S. Kozerke, H. Xue, A. E. Campbell-Washburn, T. S. Sørensen, and M. S. Hansen, "ISMRM Raw data format: A proposed standard for MRI raw datasets," *Magn. Reson. Med.*, vol. 77, no. 1, pp. 411–421, 2017.

[18] M. S. Hansen and T. S. Sørensen, "Gadgetron: An open source framework for medical image reconstruction," *Magn. Reson. Med.*, vol. 69, no. 6, pp. 1768–1776, 2013.

Summary

The research is this thesis aimed at developing methods to increase the scan efficiency of various types of MRI acquisitions. This is predominantly achieved by designing clever ways to combine data undersampling strategies with advanced reconstruction techniques. These methods are all based on the assumption of data sparsity in some transform domain, which can be highly dependent on the application itself. Increased scan efficiency can be found in various factors, such as decreasing scan times, improving spatio-temporal resolution within the same scan time or increasing the effective SNR of scans. While the methods developed in this thesis are mostly tailored for specific anatomical regions or clinical applications, the concepts may very well be translated to other applications as well.

In **Chapter 2**, I aimed to study and improve the acceleration technique 'compressed sensing' (CS) for noisy acquisitions. I introduced a novel sampling method called CS-VDA which is a combination of Cartesian undersampling and variable averaging in k-space. We hypothesized that this strategy could successfully improve image quality in the low-SNR regime. We have shown successful applications in computer simulations, in static phantoms and in *in-vivo* volunteer scans.

Chapters 3 and 4 report on a novel volumetric, accelerated dynamic contrast-enhanced MRI sequence (DCE-MRI) for vessel wall imaging. In **Chapter 3, t**he developed sequence was applied to a group of patients with femoral atherosclerotic plaques. I found a correlation between DCE-MRI and USPIO (ultrasmall superparamagnetic iron oxide particles) uptake in the patient group.
Signal from blood can negatively impact vessel wall delineation, therefore the developed sequence suppressed blood signal. This suppression makes pharmacokinetic analysis of the data more difficult. In **Chapter 4**, I investigated the use of arterial input-free analysis methods, and show that the use of such a method if a viable alternative for atherosclerotic plaques. I show successful application in two patient groups, and I make suggestions for improvement of the fitting of this analysis.

In **Chapter 5**, a radial stack-of-stars acquisition was applied for dynamic imaging of the patella in a moving knee. With this combination of innovative sampling, compressed sensing and self-gating, high-resolution dynamic knee images could be made which could provide useful in the study of bone kinematics.

In **Chapter 6**, I used the possibilities of iterative reconstruction and the MR physics to enable multi-color MRI for ^{19}F MRI. I describe a novel method to simultaneously measure two chemical compounds. With this method, successful multi-color images were made *in-vivo* in a pre-clinical animal model which had been injected with the ^{19}F compounds PFOB and PFCE.

Nederlandse samenvatting

Het onderzoek in dit proefschrift beschrijft de ontwikkeling van methoden om de scanefficiëntie van verscheidene soorten MRI-acquisities te verhogen. Dit wordt vooral gedaan door slimme manieren van databemonstering te combineren met geavanceerde reconstructietechnieken. Deze methoden zijn gebaseerd op de aanname dat de data schaars is na een wiskundige transformatie.
Een verhoogde efficiëntie kan verschillende dingen betekenen: snellere scans; een verhoogde tijds- of beeldresolutie of het verhogen van de effectieve signaal-ruisverhouding van de scans. Hoewel alle methoden in dit proefschrift zijn toegepast op bepaalde anatomische gebieden of klinische applicaties, kunnen de beschreven concepten makkelijk vertaald worden naar andere toepassingen.

In **Hoofdstuk 2** beschrijf ik een methode om de MRI-versnellingstechniek 'compressed sensing' te verbeteren voor scans die erg veel last hebben van ruis. Hiertoe heb ik een nieuwe bemonsteringsmethode ingevoerd, CS-VDA genaamd, wat een combinatie is van Cartesisch bemonsteren en een variabel aantal middelingen over de k-ruimte. Onze hypothese was dat deze strategie de beeldkwaliteit ten goede zou komen in een laag-SNR regime. We laten succesvolle toepassingen zien, zowel in computersimulaties, in stilstaand fantoombeelden als in *in-vivo* scans van vrijwilligers.

In **hoofdstuk 3 en 4** wordt gebruik gemaakt van een door ons ontwikkeld scanprotocol voor het in versneld in beeld brengen van dynamische volumetrische contrastscans voor vaatwand toepassingen. In **hoofdstuk 3** wordt deze sequentie toegepast in een een patiëntengroep met atherosclerose in de femorale vaten. Hier vonden we een positieve correlatie tussen de DCE-MRI en de opname van superparamagnetische ijzeroxide- nanodeeltjes.
Aangezien bloedsignaal het onderscheid tussen vaatwand en ander weefsel moeilijk kan maken, bevat onze nieuwe sequentie een bloedsignaalonderdrukking. Het nadeel van deze onderdrukking is dat het bloedsignaal niet meer meegenomen kan worden in de analyse van de contrastdynamiek. In **hoofdstuk 4** onderzoek ik of het mogelijk is om een analyse te doen zonder de bloeddynamiek signaal. Ik laat zien dat deze methoden succesvol toegepast kunnen worden in de beeldvorming van vaatwanden, in simulaties en in twee verschillende patiëntengroepen. Ik doe ook suggesties om de toepassing van deze methode te verbeteren.

In **hoofdstuk 5** wordt de snelle beeldvorming van de patella in een bewegende knie mogelijk gemaakt door innovatieve data-acquisitie: bestaande uit het bewegen door de k-ruimte in een ster-vorm. Door een combinatie van deze bemonstering,

compressed sensing, en *self-gating* (een innovatieve methode om de kniebeweging uit de data te halen), was het mogelijk om bewegende beelden te maken op een hoge resolutie. Dit kan een nuttige toevoeging zien in de studie naar botbewegingen.

In **hoofdstuk 6** heb ik de mogelijkheden van iteratieve reconstructie en de unieke natuurkunde van de MRI gebruikt om de *multi-color* beelden van ^{19}F-MRI mogelijk te maken. Dit wil zeggen, het gelijktijdig in beeld brengen en nadien uit elkaar halen van twee verschillende chemische verbindingen die fluor bevatten: PFOB en PFCE genaamd. Met deze nieuwe techniek konden wij de verbindingen in een muismodel injecteren, en naderhand in beeld brengen waar de verbindingen zich hadden opgehoopt. Deze beeldvorminginnovatie kan gebruikt gaan worden in de studie naar medicijneffecten in diermodellen.

PhD portfolio

Name PhD student:	Jasper Schoormans
PhD period:	March 2016 – February 2020
Promotors:	prof. dr. ir. G.J. Strijkers,
	prof. dr. ir. A.J. Nederveen
Co-promotor:	dr. ir. B.F. Coolen

1. PhD training	Year	Workload (Hours)
General Courses		
Scientific Writing	2017	1.5
Unix	2019	1.5
Didactical Skills	2019	1.5
Seminars and workshops		
Institute QuantiVision Winterschool on Machine Learning, Noordwijk, NL	2018	0.6
ESMRMB Non-Cartesian MRI: Implementation and application, Wurzburg, DE	2016	0.9
Conferences and symposiums attended		
Institute QuantiVision Conference, Amsterdam	2017, 2019	0.1
Annual Meeting of the ISMRM, Singapore	2016	0.3
Annual Meeting of the ISMRM, Honolulu, USA	2017	0.3
Annual Meeting of the ISMRM, Paris, France	2018	0.3
Annual Meeting of ISMRM Benelux chapter, Eindhoven, NL	2016	0.1
Annual Meeting of ISMRM Benelux chapter, Tilburg, NL	2017	0.1
Annual Meeting of ISMRM Benelux chapter, Antwerp, BE	2018	0.1
Annual Meeting of ESMRMB, Rotterdam, NL	2019	0.3
Imaging with Modulated/Incomplete Data, Graz, Austria	2016	0.3

Medical Imaging with Deep Learning, Amsterdam	2018	0.3

Podium Presentations

Imaging with Modulated/Incomplete Data, Graz, Austria	2016	0.2
Annual Meeting of the ISMRM, Singapore	2016	0.2
Annual Meeting of ISMRM Benelux chapter, Eindhoven, NL	2016	0.2
Annual Meeting of the ISMRM, Paris, France	2018	0.2
Annual Meeting of ESMRMB, Rotterdam, NL	2019	0.2

Poster Presentations

Annual Meeting of the ISMRM, Honolulu, USA	2017	0.2
Annual Meeting of ISMRM Benelux chapter, Tilburg, NL	2017	0.2
Annual Meeting of ISMRM Benelux chapter, Antwerp, BE	2018	0.2
Institute QuantiVision Conference, Amsterdam	2017, 2019	0.2

Other

Research visit to the Translational and Molecular Imaging Institute at Mount Sinai, New York, USA	Oct 2018- Feb 2019	

2. Teaching

Lecturing

Advanced MRI – MSc course	2018, 2019	1.0

Tutoring

Advanced MRI – MSc course	2017, 2018, 2019	1.0
Data Analysis in MATLAB	2016-2019	0.2
Institute QuantiVision Winter school on Machine Learning	2018	0.5

Supervising

MSc Graduation project supervision (4 students)	2016, 2017, 2018, 2019	10.0

3. Parameters of Esteem

Grants

Travel grant Amsterdam University	2018
ISMRM educational stipend	2016-2018

Awards and Prizes

Summa Cum Laude ISMRM Merit award	2018

Organizational Activities

10th Annual Meeting of ISMRM Benelux chapter, Antwerp, BE	2018

Acknowledgements

At the time of writing, in the tumultuous summer of 2020, it has been more than five years since I took my first steps in the MR research community. Every single day since then, I have been grateful for the opportunity to do research at this institute. On the one hand, this setting has been intellectually stimulating, with many fruitful discussions, opportunities and a team with widely varying interests. But the nice atmosphere must have been what made me determined to start a PhD here. Looking back, I can say that this was the right choice.

Allow me to express my sincere gratitude on these pages.

To my promotion team, thank you very much for all your confidence, freedom, and opportunity. Bram, we have had many wonderful discussions, which could go on and on, with ideas getting more and more wild. You have been a wonderful daily supervisor and I hope many others will have the chance to enjoy your guidance. Gustav, you had confidence in me, from tutoring and helping the courses to sending me to NYC. Aart, you have provided a wonderful research environment and made many collaborations possible. Thank you all very much.

Thank you to the committee members, for giving me the opportunity to discuss this work with you. I look forward to a lively discussion - either in-person or via video messaging.

I have had the opportunity to collaborate with so many talented people. Oliver, thank you for guiding me into the world of research during my first year at the AMC. Valentina, we managed to publish a wonderful paper, and you taught me many things when I was just starting out. Kerry, we started many projects in wild enthusiasm – based on some paper we read. This did not result in a publication, but it does not matter: the most important goal of science is to satisfy our curiosities. The compressed sensing team: Eva, we made a great patch together, but most importantly we laughed a lot! Lukas, without your continual development on the PROUD patch, I could never have done many things in this thesis. Kang, thank you for the great collaboration! Oliver Maier, many thanks for the nice work we did. Prof. Hansen, thank you for explaining the theoretical foundations of compressed sensing theory and suggesting helpful experiments.

Dear roommates Z0-178 (Koen, Carmen, Bobby, Luuk, Liza, Jithsa, Lena, Paul DH, Wouter, Bada, Jos), we have had so much fun and been through so many highs and lows. It is tempting to list so many memories here. I will only mention the annual ISMRM deadline weeks - the deadline is usually at my birthday. I fondly think back

to these days, so fantastically filled with science. We supported and encouraged each other. You could expect to be a 'volunteer' in the scanner daily, while filling up the rest of the waking hours with writing or making figures.
Dear colleagues (Joena, Melissa, Esther, Sandra, Raschel, Anouk, Claudia, Geor, Jules, Mariah, Marieke, Matthan, Michelle, Ot, Sophie, Toni, Pim, Paul G, Marian, Susi, Luka, + many others), thank you for being part of this wonderful community. The lunches, coffees, *borrels*, parties, conferences and conversations we shared were the highlight of many days. To all the PhDs: enjoy - you'll be done before you know it!

I have been lucky enough to do part of my research in New York, at the TMII Institute at Mount Sinai in the fall of 2018. New York must be one of the most beautiful cities in the world in October. This was a very educational and amazing experience. Many thanks to Claudia, Zahi and Willem, and my colleagues (Alex, Thomas) over there.
Thank you for all the MRI volunteers - you made an essential contribution.

I have had the honour of working with many students, both in a supervisory role for MSc theses as well as during the annual *Advanced MRI* course. Thank you all for your interest and hard work. I was very happy that three of the students, Bobby, Laura and Ernst, decided to pursue a PhD in MRI research after their Master's. Good luck!

Finally, I want to give an expression of gratitude to all of the researchers, from all over the world, that are always ready to help in any way. I have sent many e-mails to scientists I had never met, and every single one has been responded to in the kindest and most helpful way.

Lieve schoonfamilie, bedankt voor jullie steun!

Lieve familie, papa, mama, Anouk en Manon. Eindelijk klaar in het verre Amsterdam. Zonder jullie liefde en steun zou dit proefschrift hier niet liggen. Bedankt voor alles.

Lieve Abegail, we hebben al zoveel meegemaakt samen, niet in het minst het laatste jaar. Bedankt dat je er altijd voor me bent. Op naar het volgende avontuur, samen met onze kleine Zora!

List of Publications

Journal publications

Compressed sensing MRI with variable density averaging (CS-VDA) outperforms full sampling at low SNR
***J Schoormans**, GJ Strijkers, AC Hansen, AJ Nederveen, BF Coolen.*
Physics in Medicine & Biology 65 (4), 045004, 2020

An iterative sparse deconvolution method for simultaneous multicolor ^{19}F-MRI of multiple contrast agents
***J Schoormans**, C Calcagno, MRR Daal, RCI Wüst, C Faries, A Maier, A JP Teunissen, S Naidu, BL Sanchez-Gaytan, AJ Nederveen, ZA Fayad, WJM Mulder, BF Coolen, GJ Strijkers.*
Magnetic resonance in medicine 83 (1), 228-239, 2019

Plaque Permeability Assessed With DCE-MRI Associates With USPIO Uptake in Patients With Peripheral Artery Disease
KH Zheng, **J Schoormans***, LCA Stiekema, C Calcagno, I Cicha, C Alexiou, GJ Strijkers, AJ Nederveen, ESG Stroes, BF Coolen*
JACC: Cardiovascular Imaging 12 (10), 2081-2083, 2019
(* Both authors contributed equally)

Rapid T1 quantification from high resolution 3D data with model-based reconstruction
*O Maier, **J Schoormans**, M Schloegl, GJ Strijkers, A Lesch, T Benkert, T Block, BF Coolen, K Bredies, R Stollberger.*
Magnetic resonance in medicine 81 (3), 2072-2089, 2019

Accelerated 4D self-gated MRI of tibiofemoral kinematics
V Mazzoli, J **Schoormans***, M Froelin, AM Sprenger, BF Coolen, N Verdonschot, GJ Strijkers, AJ Nederveen.*
NMR in Biomedicine 30 (11), e3791, 2017
(* Both authors contributed equally)

A hybrid tomographic reconstruction algorithm for high speed X-ray tomography
X Yang, JR van Ommen, J Schoormans, RF Mudde.
Computer Physics Communications 196, 27-35, 2015

Refereed Proceedings

Schoormans J, Calcagno C, Nederveen AJ, Strijkers GJ, Coolen BF.
"Black-blood 3D DCE-MRI of the aortic wall with AIF-free pharmacokinetic modeling: feasibility in abdominal aortic aneurysm patients"

In proceedings of the 28th annual meeting of ISMRM, Sydney, 2020

Schoormans J, Calcagno C, Daal M, Faries C, Sanchez-Gaytan B, Nederveen AJ, Fayad ZA, Mulder WJM, Coolen BF, Strijkers GJ.
"A novel iterative sparse deconvolution method for multicolor ^{19}F-MRI"
In proceedings of the 26th annual meeting of ISMRM, Paris, 2018

Coolen BF, **Schoormans J**, Kooreman E, Zhang Q, Viessmann O, Strijkers GJ, Nederveen AJ, Gilbert G, Siero JCW.
"Double DANTE: an improved method for high-resolution intracranial vessel wall imaging"
In proceedings of the 26th annual meeting of ISMRM, Paris, 2018

De Heer ,P van Schelt A, **Schoormans J** , Strijker GJ , Coolen BF , Runge JH, Stoker J, Nederveen AJ.
"Respiratory binning showdown; self-gated, respiration belt or pencil beam?"
In proceedings of the 26th annual meeting of ISMRM, Paris, 2018

Maier O, Schloegl M, **Schoormans J**, Coolen BF, Block T, Strijkers GJ, Stollberger R.
"Golden-Angle radial 3D T1 quantification with minimal scan time utilizing constrained model-based reconstruction."
In proceedings of the 26th annual meeting of ISMRM, Paris, 2018

Schoormans J, Zheng K, Stroes ES, Strijkers GJ, Nederveen AJ, Coolen BF.
"3D black-blood DCE-MRI using radial stack-of-stars acquisition and CS reconstruction: application in carotid and femoral arteries".
In proceedings of the 25th annual meeting of ISMRM, Honolulu, 2017

Mazzoli V, **Schoormans J,** Froeling M, Sprengers A, Nicolay K, Coolen BF, Verdonschot N, Nederveen, AJ, Strijkers GJ.
"Dynamic Knee Imaging Using 4D Self-Gated MRI with Compressed Sensing Reconstruction"
In proceedings of the 25th annual meeting of ISMRM, Honolulu, 2017

De Heer P, Hemke R, Lavini C, **Schoormans J**, Coolen BF, Barendregt A, Strijkers GJ, Maas M, Stoker J, Nederveen AJ, Runge J.
"Feasibility of GRASP DCE-MRI in Children with Juvenile Idiopathic Arthritis (JIA)"
In proceedings of the 25th annual meeting of ISMRM, Honolulu, 2017

De Heer P, Gurney-Champion O, Runge J, Klaassen R, **Schoormans J,** Coolen BF, van Laarhoven H, Hanneke, Strijkers GJ, Stoker J, Nederveen AJ.
"Free Breathing T2 Mapping of the Liver Using a Compressed Sensing Reconstruction"*
In proceedings of the 25th annual meeting of ISMRM, Honolulu, 2017

Schoormans J, Gurney-Champion O, Klaassen R, Runge J, Gonçalves S, Coolen BF, Motaal A, van Laarhoven H, Stoker J, Nederveen AJ , Strijkers GJ,
"4D Radial Fat-Suppressed Alternating-TR BSSFP MRI with Compressed Sensing Reconstruction for Abdominal Imaging During Free Breathing."
In proceedings of the 24th annual meeting of ISMRM, Singapore, 2016